Integrated Rotor Air Cooling System Design in Axial Flux Permanent Magnet Machines for Aerospace Applications

By

Islam Zaher

A Thesis Submitted to the School of Graduate Studies in Partial Fulfillment of the Requirements for the Degree

Master of Applied Science in Mechanical Engineering

Supervisor: Prof. Ali Emadi

Abstract

In the wake of the rising global demand for more electric transportation, aerospace electrification is becoming a highly active research area as commercial fully electric aircrafts are becoming a reality. The transportation electrification industry is challenged to develop powerful, safe, and compact-sized machines that can replace fossil fuel powered engines in aircrafts. Axial Flux Permanent Magnets (AFPM) machines are currently being intensively developed as a great candidate for this purpose due to their inherently higher power density compared to other machine electric machines topologies. The efforts of further increasing AFPM machines power density add more thermal challenges as intensive cooling is required at a relatively small machine package to avoid machine failure. One of the most concerning failure modes in these machines is power output reduction due to overheating of the rotor-mounted permanent magnets or even complete failure due to irreversible demagnetization. This research discusses the design process of an integrated rotor air cooling system for a 100 kW AFPM machine designed for an electric aircraft propulsion system. The embedded cooling system allows the rotor to be self-cooled at a sufficient cooling rate while minimizing the impact on machine efficiency due to windage power losses. The presented design process includes several stages of cooling enhancement including the addition and fine-tuning of rotor fan blades and rotor vents design. These enhancements are done by studying the air flow over the rotor surfaces in conjunction with heat transfer through Conjugate Heat Transfer (CHT) Computational Fluid Dynamics (CFD) analyses. In an initial study, different rotors with different combinations of rotor cooling features are studied and their thermal performance is compared. The results show that using rotor embedded fan blades in throughflow ventilated rotor geometry offers the best performance balance, achieving sufficient rotor cooling rate within a reasonable increase of windage power loss. A parametric study is performed to improve the rotor blade geometry for a higher ratio of heat transfer to windage losses. Another study is performed where the rotor and the enclosure geometries are fine-tuned simultaneously to reduce the negative effect on rotor heat transfer imposed by the enclosure. The final geometry of the rotor enclosure assembly is generated based on the research results and the design is integrated into the final machine prototype to be tested.

Table of Content

Acknowledgments

Firstly, I would like to thank my supervisor Prof. Ali Emadi for making this research possible and granting me the opportunity to work under his mentorship in a world-leading research group, and for his support during the rough times of the pandemic.

I would also like to thank all my team members and leaders for their devoted work and their contribution to this project and for making it a reality. Special thanks go to Dr. Romina Rodriguez, the thermal design lead, for her constant guidance and unconditional support.

I would also like to express my gratitude to all the professors and teachers who helped me form the knowledge I needed for this research. Special thanks go to Prof. Marylin Lightstone and Paul Galpin, for their mentorship and support with their thorough knowledge of computational fluid dynamics.

Thanks to Eaton Corporation and Mitacs for funding this research project and special thanks to Eaton Aerospace design team for their support and their very helpful insights in aerospace applications design.

All my gratitude and love to my family, to them I owe all my successes in life, and I will always be grateful for their help and support throughout my academic journey. I cannot find enough words to express my grace to my parents for always being my biggest supporters. Thanks to my sisters Noha and Nada for all their love and encouragement. And thanks to my brother Mohammed for being my study partner and always being there for me with his support and motivation.

I would like to pay tribute and remember all the loved ones that I lost over the term of my study, my beloved uncle Mohsen, and my dear colleagues Iman Aghabali and Mehdi Eshaghian. May God bless their souls and grant their families peace.

Lastly, thanks to God for the blessings He bestowed upon me that allowed me to accomplish this task.

"And my success is not but through Allah. Upon Him I have relied, and to Him I return"

Quran 11:88

List of Figures

List of Tables

Chapter 1

Introduction

1 Introduction

1.1 Background and Motivation

Transportation electrification has recently become a necessity that is no longer overshadowed by the highly developed fossil fuel powered transportation systems. Nowadays governments are not just enforcing strict regulations on vehicle emissions but also aiming for the complete ban of fossil fuel powered vehicles by the end of the decade [1][2]. Such regulations push the manufacturers and the whole transportation industry towards electrification. The strong influence of transportation electrification on the automotive industry, and the electrification research in accordance, drives a rising movement to broaden the electrification initiative to include, not just ground transportation, but also air and marine transportation as more powerful and efficient electric drivetrains choices become available.

1.2 Aerospace Electrification

There is no doubt that aviation transportation is one of the biggest contributors to global greenhouse gas (GHG) emissions contributing by 2.4% of the global CO_2 emissions [3][4]. Aviation is the highest GHG emitting mode of transportation per passenger per traveled distance among other modes as shown in Fig. 1-1 [5]. Hence, there is a growing global interest in aerospace electrification.

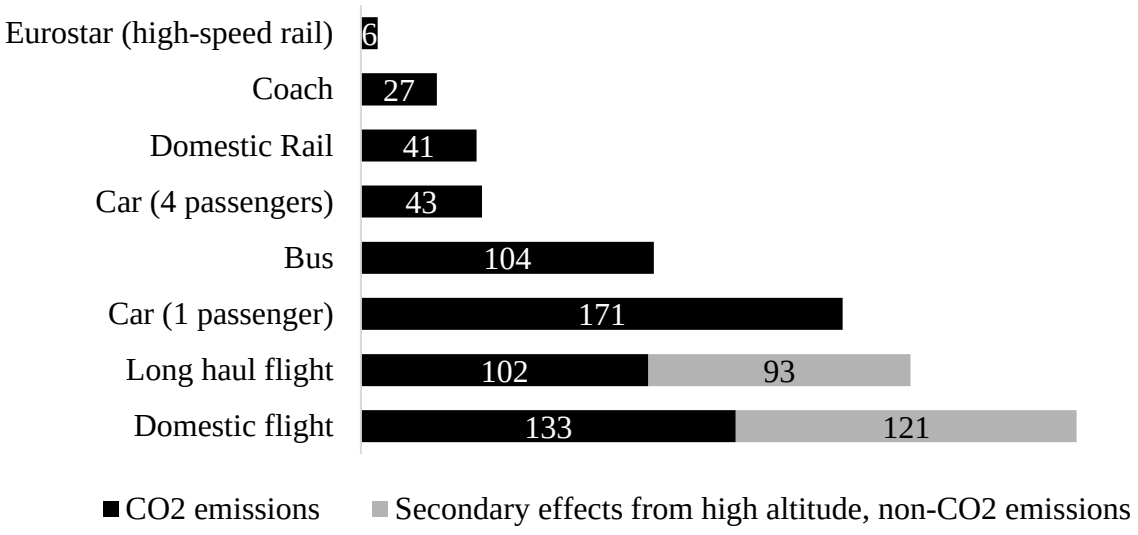

Fig. 1-1 Comparison of normalised emissions per passenger per km travelled of different modes of transportation [5]

Two main challenges are currently facing the electric aerospace industry. First, the relatively low power density offered by current electric energy storage technologies, compared to jet fuel as a mean of energy storage commonly used in nowadays aircrafts. Second, the immaturity of current state-of-art electric propulsion systems to match the current standards of air transportation [6]. While the all-electric long-haul commercial flights might still not be achievable with current technologies, intense research allowed making grounds in the area of electrified urban air mobility [7]. Electric vertical take-off and landing (eVTOL) aircrafts are great candidates for urban air mobility and intercity air traveling with many successful prototypes (shown in Fig. 1-2) being currently tested for commercialization by major aerospace industry-leading companies [8][9].

Fig. 1-2 Joby four-passenger eVTOL prototype during a 150 miles test flight [9]

1.3 Axial Flux Permanent Magnets Machines for Aerospace Applications.

Axial flux permanent magnet (AFPM) machines are great candidates for eVTOL powertrain given their high power density compared to other electric machine topologies [10]. The inherently longer torque arm of the axial flux machine topology results in a very high torque production in a relatively compact machine package size. However, the compact machine size imposes challenges on the thermal stability of the machine as more intensive cooling is needed within a limited space. Efforts are done to further increase AFPM machines power density electromagnetically through the control of the electric current without changing the machine

size or geometry. This results in very high eddy current losses in both the stator and the rotor that can trigger many of the failure points in the machine if not thermally managed.

High power density AFPM machines stators are usually cooled using dedicated liquid cooling loops since the highest losses are usually concentrated in the stator [11]. On the other hand, considerable heat losses are also generated in the rotor due to electrical as well as mechanical losses. Rotor losses can lead to output power reduction due to magnets overheating or even complete failure due to irreversible demagnetization if the magnets are not adequately cooled [12]. Machine losses can be broken down as shown in Fig. 1-3. Efforts to increase AFPM machine power density have resulted in exacerbating magnet overheating issues, especially for an air-cooled rotor. This is due to the higher eddy-current losses in the magnets associated with the higher flux generated by the stator at a limited rotor cooling capacity. Cooling the rotor predominantly by air limits the cooling capacity since the cooling rate is dictated by the rotor geometry and operating speed. Nevertheless, air cooling has the advantage of being a simple and less power-consuming rotor cooling method compared to other methods such as phase change and liquid cooling [13]. Moreover, the air cooling rate can be maximized at the same operating conditions by improving the rotor geometry to enhance the airflow over the rotor surfaces.

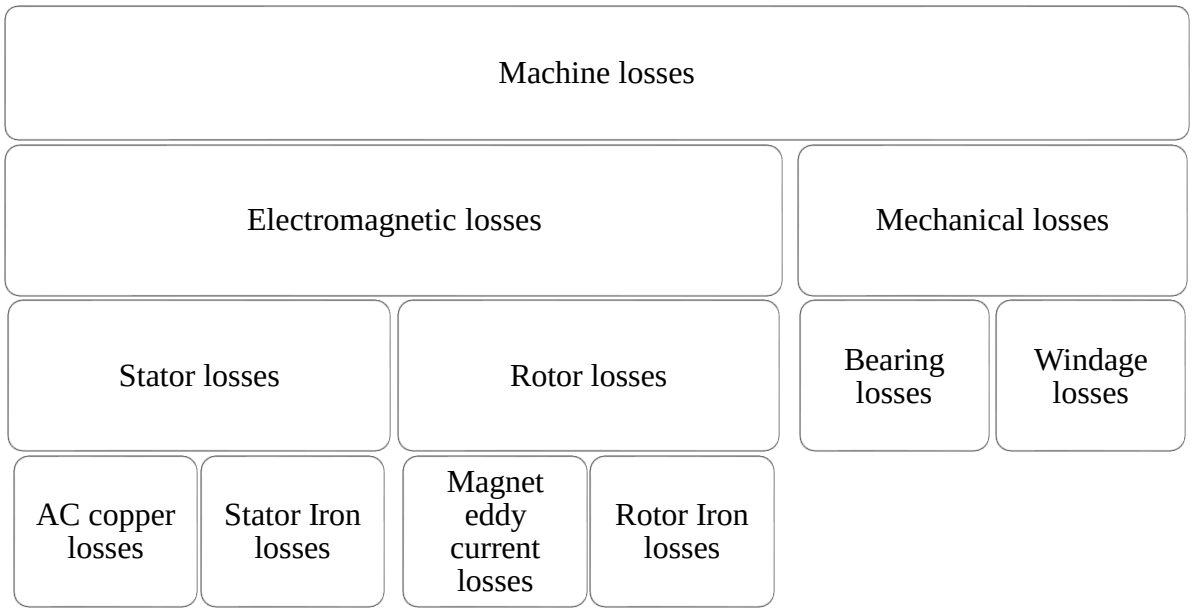

Fig. 1-3 Breakdown of AFPM machine losses

1.3.1 Machine topology

The designed machine has a Single Stator Double Rotor (SSDR) AFPM topology as shown in Fig. 1-4. The machine has a total of 16 poles. The stator and the two rotors are mounted on a shaft at the center with two bearing couplings, one on each rotor. The stator is liquid-cooled through a separate cooling loop fed through manifolds embedded in the motor housing (casing). The motor housing also includes the air ports (Single inlet and multiple outlets) for the proposed air cooling system. Two rotor covers are attached to the housing, one on each side of the machine. The two rotor covers contain embedded inlet manifolds for each rotor, while one of the covers also contains an enclosure for the resolver to be mounted. Accordingly, the rotor opposing this cover is designed to have the resolver target mounted on it.

The machine is required to be stackable as shown in Fig. 1-5 (b). This means that two machines can be stacked on top of each other coupled through a single shaft, hence, the access to the machine cooling systems can only through its side. Additionally, the converter is designed to be mounted to the side of the machine allowing it to be modular as shown in Fig. 1-5 (a). This adds more challenges to the air cooling system design as will be discussed later in Chapter 5.

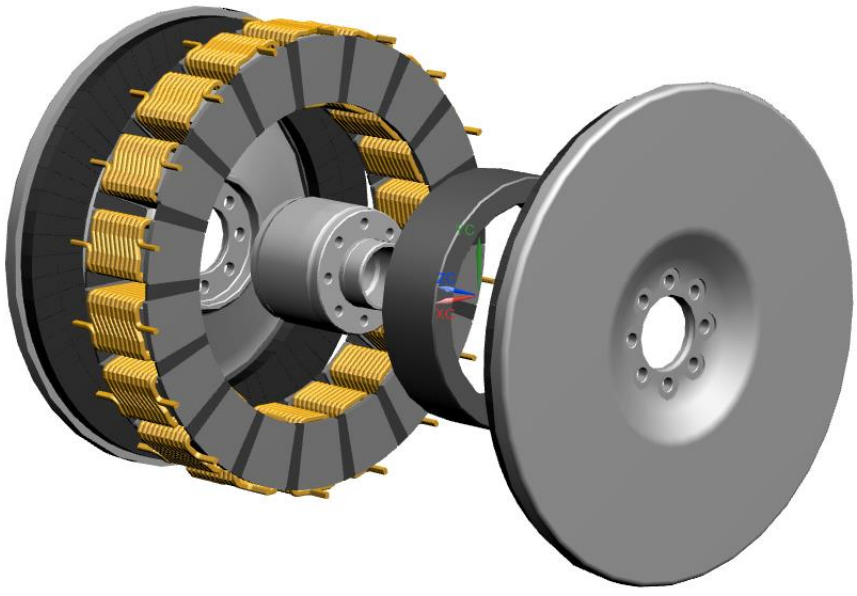

Fig. 1-4 Preliminary SSDR AFPM machine design.

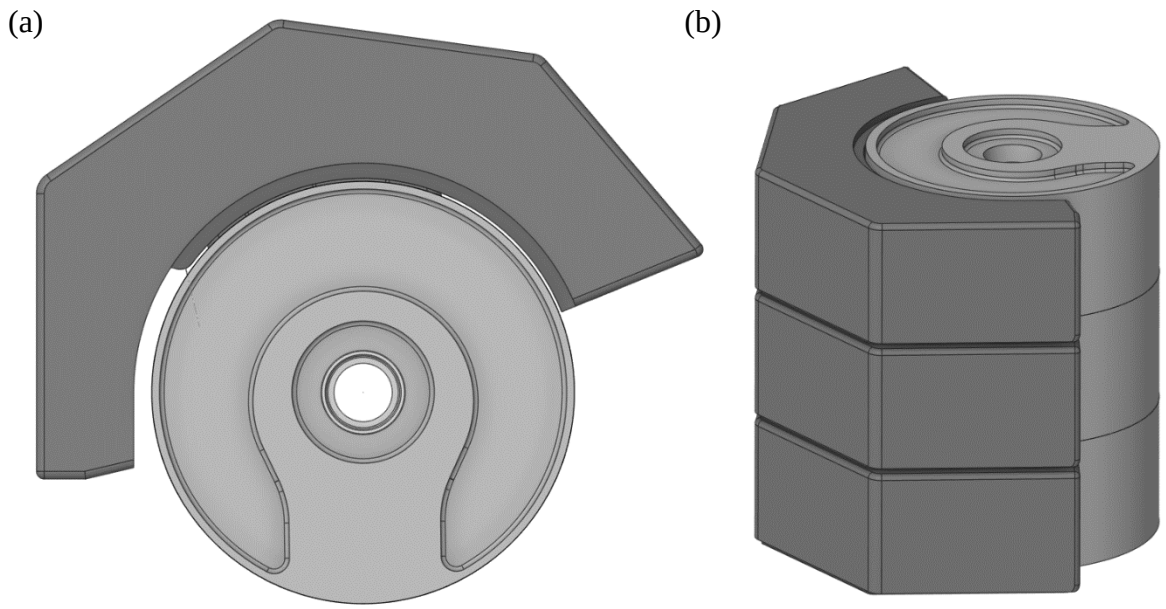

Fig. 1-5 (a) Representation of the full modular assembly of the machine and the inverter. (b) Stacked motors assembly.

1.3.2 Machine operating conditions and rotor losses analysis

The rotor structure consists of a Halbach magnets array forming a total of 16 poles with a back iron of a smaller thickness. The magnets are bonded to the back iron using magnet adhesive, and both are bonded to an aluminum rotor carrier using the same adhesive. The adhesive bond line is estimated to be of 0.05mm thickness. The rotor structure is mounted to the center shaft with bearing coupling between each rotor and the stator. The rotor and the stator assembly have a 1 mm air gap thickness. A schematic of the machine assembly is shown in Fig. 1-6 and rotor materials and their properties are listed in Table 1.

Property	Magnets	Back Iron	Rotor Carrier	Adhesive
Material	NdFeB	Cobalt steel	Aluminum	Epoxy based
Thermal conductivity (W/m.K)	7.6	36.1	237	1.87
Density (kg/m^3)	7580	8120	2702	1900
Specific heat capacity (J/kg.K)	460	440	903	~1100

Table 1 Rotor components materials and their properties.

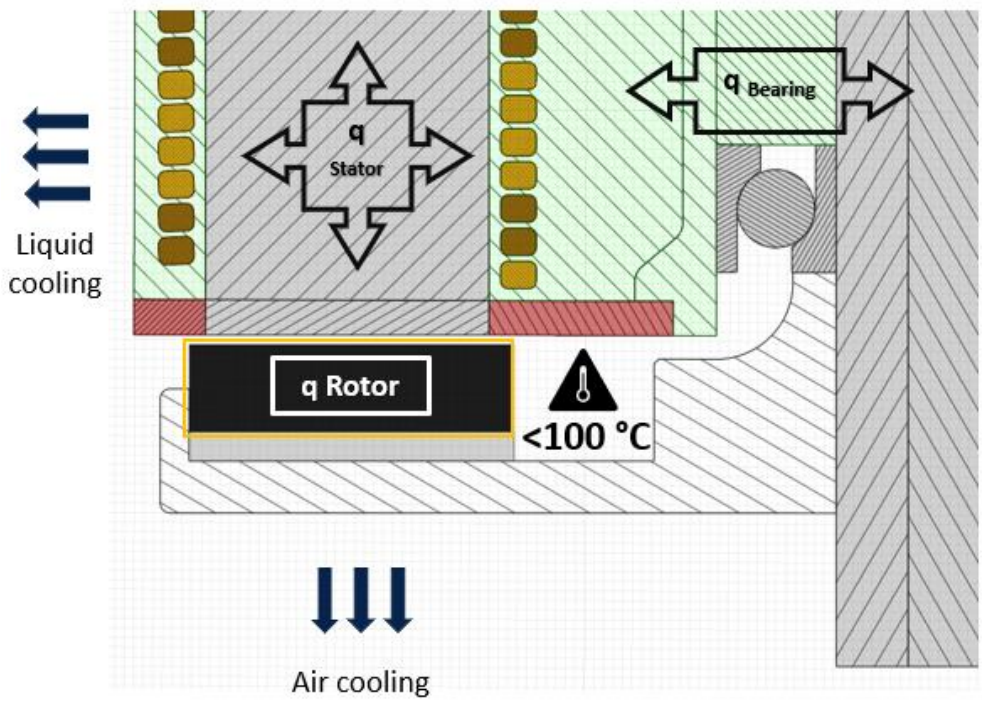

Fig. 1-6 Schematic of AFPM rotor-stator assembly and losses involved.

The machine is designed to have a continuous power output of 100 kW at a rotation speed of 6500 RPM. This operating point is chosen as the design point for the machine thermal design Rotor losses due to eddy currents are estimated based on the continuous design point assuming magnets temperature of 100 ℃. Moreover, a safety factor (SF) is added for the electromagnetic (EM) losses to account for uncertainties. A breakdown of the rotor losses is shown in Table 2

Continuous power output		100.3 kW
Rotational speed		6500 RPM
Rotor losses	Magnet eddy-current loss	593 W
	Rotor iron loss	28 W
	Rotor Bearing loss	537 W
	Total (including 10% EM SF)	1220
	Total per Rotor (including 10% EM SF)	610

Table 2 Rotor losses at continuous power output operation point

1.3.3 Rotor modes of failure and considerations

Rotor modes of failure can be classified into the following:

1. **Thermal-electrical failure** due to magnets overheating results in demagnetization and power loss. For Neodymium magnets, magnetic flux reduces linearly as the temperature increase as a result of reversible demagnetization. The drop becomes more significant past the 120 ºC reaching irreversible demagnetization limits at 150 ºC as shown in Fig. 1-7 [14]. Accordingly, the magnetic torque also decreases with the increase of the temperature proportionally. However, the nonlinear drop in torque starts at a lower temperature of 100 ºC as shown in Fig. 1-8. Therefore, maximum magnets temperature of 100ºC is set as a design limit in this research.

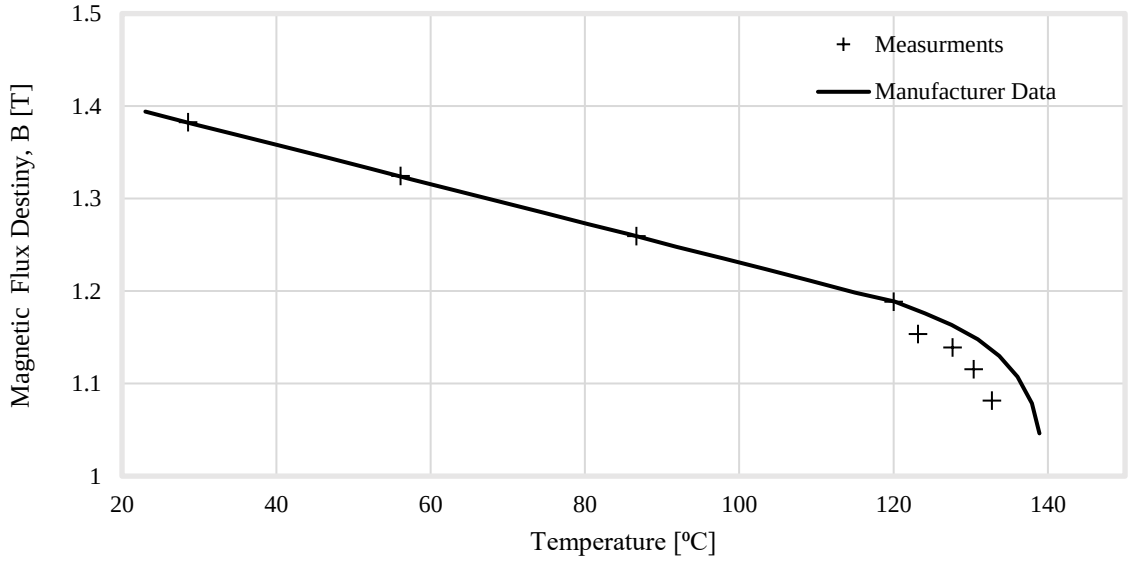

Fig. 1-7 Effect of magnets temperature on flux density [14]

2. **Thermal-structural failure** due to epoxy adhesive failure due to its temperature exceeding the glass transition limit. Past the glass transition temperature, the cured epoxy tensile strength drops drastically which might cause magnets debonding from the mounting surface and complete structural failure of the machine. The magnet adhesive is selected to have a high glass transition temperature of 200ºC according to the manufacturer data.

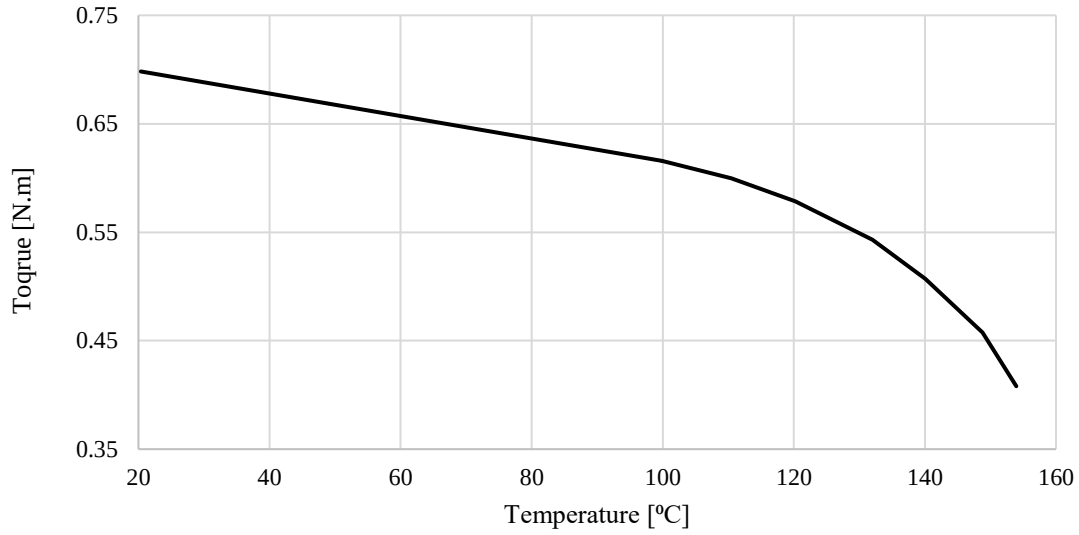

Fig. 1-8 Effect of magnets temperature on magnetic torque [14]

3. **Mechanical-structural failure** due to excessive stresses on the rotor carrier as a result of the machine high rotational speed causing rotor deformation. The aluminum relatively low tensile strength compared to other commonly used rotor materials (e.g., steel or titanium) is compensated by increasing the rotor thickness where stresses are found to be high. Despite such disadvantages of aluminum as a rotor carrier material, its superior thermal conductivity makes it a better option from a thermal standpoint.

The machine is designed to operate in harsh ambient conditions. Two main factors are considered to define these conditions, the ambient temperature (or inlet flow), and the operation altitude. High air temperature and low air density due to elevation can significantly deteriorate the machine cooling systems performance. Worst-case conditions for the rotor air cooling system design are defined at 55ºC ambient temperature or at sea level. Although the machine is designed to operate at altitudes as high as 15000 ft significantly reducing the total cooling air mass flow rate and cooling performance, it is found that the effect of higher temperature is more critical to the rotor than the effect of elevation. Moreover, the simultaneous occurrence of the two conditions is highly unlikely given the inherently low air temperature at high altitudes (at 15000ft the ambient air temperature is nearly -15 º).

1.4 Research Objectives

The aim of this research is to develop an integrated air cooling system for rotor cooling in an AFPM machine. The cooling system is intended for a newly developed 100 kW motor developed by Eaton corporation and McMaster University. The machine is targeted to be used for aerospace applications, eVTOL propulsion drivetrain specifically. The required continuous high power output for flight operation, as well as, the strict flight safety regulations mandates having a reliable and efficient rotor cooling system to rule out the rotor as one of the machine critical failure points. This is done through the following design stages:

1.4.1 Thermal analysis of AFPM machine rotor

The failure modes of the AFPM machines rotor, whether it is electromagnetic or structural, are often related to thermal failures. In order to design an effective rotor cooling system, a number of studies are done through this research to understand the thermal behavior in the rotor and assess its performance at every design stage prior to prototyping. This is done with the aid of computational fluid dynamics (CFD) simulations for fast and reliable results.

1.4.2 Improvement of rotor geometry for rotor air cooling enhancement

The inherently limited capacity of air cooling relative to the high heat losses generated in the rotor during continuous operations requires adaption of its geometry to enhance the cooling. Two design parameters are targeted through the enhancement of the rotor geometry: First, the rotor pumping capacity (mass flowrate), and second, the convective heat transfer on its surface. The two parameters control the cooling rate over the rotor surfaces, hence, the temperature distribution and the maximum temperature of local hotspots. One drawback of such enhancement is the increased windage losses due to increased drag and friction over the rotor surfaces. Different geometrical features are tested and improved in this research. The rotor geometries are judged based on their ability to achieve the best cooling performance at the lowest possible windage losses.

1.4.3 Design and thermal modeling of the rotor – enclosure assembly

The requirement of the machine to be enclosed imposes a challenge to the air cooling design of the rotor due to the increased pressure losses causing reduction of the total mass flow rate and unevenness of the flow over the rotor surfaces. Few iterations are done for improvement

and fine-tuning of the full rotor-enclosure assembly geometry within the allowable machine package size.

1.5 Thesis Outline

Chapter 1: Introduction.

A brief discussion of the ongoing efforts in the field of aerospace electrification, and it being the driving motivation behind this research. AFPM motor is discussed as a good candidate for electric aircrafts drivetrain. Moreover, the steps followed in this research for designing a reliable embedded air cooling system for an AFPM machine rotor are furnished.

Chapter 2: Rotor Air Cooling in Axial Flux Permanent Magnet Machine

A survey of the related research on the air flow in rotor-stator systems in general, and AFPM machines in particular. The survey aims for understanding the flow and cooling mechanisms in rotor-stator systems, also to set guidelines for the best initial rotor geometry in terms of cooling based on the findings of other researchers.

Chapter 3: Computational Fluid Dynamics

Discussing the rotor air cooling thermal analysis problem from Computational Fluid Dynamics (CFD) point of view. The setup of the different rotational models used for rotor simulations are discussed in detail. The benefits of Conjugate Heat Transfer (CHT) CFD simulations for rotor cooling simulations over analytical and conventional CFD analyses are also argued.

Chapter 4: Integrated Rotor Air Cooling Improvement and Design Iterations

In this chapter, the process of designing an efficient rotor cooling system is discussed, starting from the initial direction setting for the rotor cooling system to the final rotor-enclosure system prototype design.

Chapter 5: Conclusion and future work.

A summary of the work done in this research and statement of the important outcomes and future work and designs that can be researched for further improvements.

Chapter 2

Rotor Air Cooling in Axial Flux Permanent Magnet Machine

2 Rotor Air Cooling in Axial Flux Permanent Magnet Machine

This chapter discusses the physics and the understandings behind rotor cooling in AFPM machines. This is done by going through the literature and the studies done regarding this topic. The thesis studies the design process and improvement of a rotor air cooling system for an AFPM machine; accordingly, the flow over rotating bodies is of great interest, and it is studied first to fully understand the associated flow patterns over the different rotor surfaces. These flow patterns usually have a great effect on heat transfer. The next section discusses the heat transfer over the rotor body while focusing on the different analytical and numerical solutions for the heat transfer over the different surfaces of the rotor. For instance, the heat transfer at the air gap was studied by many researchers due to the complexity of the flow as it varies with the gap dimensions, rotor geometry, and operating conditions. The other surfaces of the rotor including its internal rotating cavity, rotor back, vents, and blades also have to be studied since the air flow exhibit different patterns over each surface, this affects the heat transfer intensity over each surface which involves different solutions and heat transfer correlations for these solutions. Finally, the last section is reviewing the different approaches studied in literature to improve the rotor air cooling in AFPM machines.

2.1 Flow Over Rotating Disks

The rotor of an AFPM is usually designed as a flat disk with the permanent magnets mounted on one side of it, therefore studying flow over rotating disks is of great importance to this research. The rotor disk rotational motion induces a centrifugal flow around it known as Bödewadt flow. Von Karman [15] investigated this type of flow by modeling the flow over a rotating disk of an infinite radius, reducing Navier-Stokes equations to four coupled nonlinear ordinary differential equations through different assumptions. The study concluded that the fluid around the disk that is initially at rest is subjected to viscous stress at the disk boundary as a result of the disk relative motion as it rotates at steady angular velocity. The viscous forces drag the fluid at the disk boundary in a circular motion. However, due to the absence of a pressure gradient in the radial inward direction, the centrifugal force on the fluid makes it move in a spiral motion towards the disk periphery rather than in a perfectly circular rotation. This results in a centrifugal fan-like action where

the fluid is drawn axially towards the disk and flows outwards at its outer diameter. The axial flow towards the disk surface ensures that the mass flow is conserved, and the vorticity is confined in the boundary layer over the disk surface.

Rotating flow over a stationary disk was solved by Bödewadt [16] and found to have an effect opposite to what happens in the case of the rotating disk. The fluid near the disk surface flows radially towards the disk center.

The rotating flow behaves differently when confined between a rotating and a stationary disk. Therefore, the case where the flow is confined between two disks with one of them being stationary and the other is rotating at a specific rotational speed had to be studied separately.

Batchelor [17] investigated this case by solving the differential equations for an asymmetric flow between two coaxial disks of an infinite radius. According to his solution, a non-viscous fluid core is formed between two separate boundary layers at each disk surface. The boundary layers at the stator and the rotor can be either laminar or turbulent depending on the rotor rotational speed and the resulting Reynolds number. The rotating core is balanced by a radial pressure gradient that opposes the centrifugal force. These two forces keep the rotating core at a nearly constant radial position at a given rotational speed. Stewarton [18] solution opposed Batchelor solution showing that there is no core rotation and that the tangential velocity can vary from zero at the stator boundary to a non-zero value near the rotor surface. The contradicting solutions of Batchelor and Stewartson were mentioned in many following studies that provided numerical and analytical solutions for Von Karman similarity equations that supported either of the two solutions [19] [20], and other review articles in literature related to flow over rotating disks where the different solutions were reviewed and discussed [21] [22] [23] [24].

Mellor et.al [25] provided a solution for the similarity equations for infinite disks and discussed the possibility of the two solutions at different Reynolds number values, with Batchelor flow was associated with low Reynolds flow. They also suggested the possible influence of the disk edge effect on the flow type in the case of a finite disk, where the outward flow near the rotating disk edge is re-ingested in the boundary layer over the stationary disk inducing core rotation. Brady and Durlofsky [26] studied the solution for

disks with finite radius and found that the Batchelor flow type is associated with enclosed rotor-stator assemblies, while Stewartson flow type can be found in open periphery throughflow systems. Batchelor flow type was also noticed in throughflow systems at low Reynolds number. Daily and Nece [27] studied the flow in an enclosed rotor-stator assembly and classified the flow in the clearance between the two disks (or air gap) into four different flows dependent on the rotational Reynolds number, and the ratio between the axial clearance, s, and disk radius, R, usually referred to as air gap ratio ($G=s/R$). Experiments were done using different air gap clearances at rotational Reynolds number ranging from 10^3 to 10^5. The authors proposed four possible flow regimes and related their existence to different combination of the gap axial clearance and the flow Reynolds number. The mentioned flow regimes can be classified into first, turbulent and laminar flows of merged or non-merged boundary layers. According to the figure below (Fig. 2-1), the following can be observed:

1) laminar flow with merged boundary layers exists at low Reynolds number and small gap clearances.
2) laminar flow with non-merged boundary layers exists at larger axial clearances. While for a given axial clearance the laminar boundary layers can become unmerged at a higher Reynolds number. For small gap clearances, the boundary layers will stay merged even at a high Reynolds number before they transition into turbulent boundary layers.
3) merged turbulent boundary layers exist at high Reynolds number and small gap clearances. At larger gap clearances, turbulent boundary layers may never become merged.
4) non merged turbulent boundary layers can exist at any gap clearance if Reynolds number is high enough.

It was also observed that a minimal radial outflow exists midplane across the gap and that the average tangential velocity in the gap decreases as the gap clearance is increased at a constant Reynolds number.

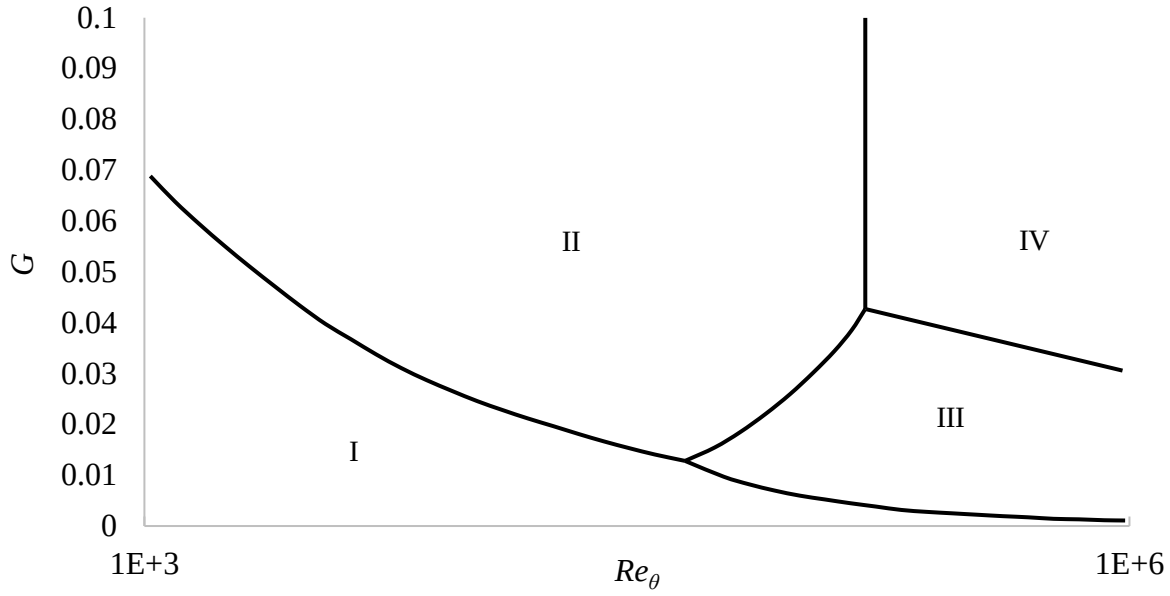

Fig. 2-1 Four air gap flow regimes as defined by Daily and Nece [27] based on *G* and Re_θ, from Owen and Rogers [28]

Poncet et. al [29] studied the turbulent flow in a rotor-stator system with and without a through flow. The flow was studied experimentally and numerically at three different values of Reynolds numbers and two different gap aspect ratios. The study concluded that the flow remains of Batchelor type for closed systems as well as when a weak through flow is allowed. The study also showed that increasing Reynolds number at a given through flow rate changes from Stewartson type to Batchelor type. The results showed that both flow types can co-exist at different disk radial locations and that the Stewartson flow tends to dominate the flow at the smaller radii.

The transition from Batchelor to Stewartson flow was found mostly dependent on the through-flow rate. Two correlations that relate the flow entrainment coefficient, *K* (the ratio between the tangential velocity of the flow at the rotating core and the disk surface), and the local flow rate coefficient, Cq_r, were derived from the collected experimental data shown in Fig. 2-2. Note that high *K* values denote the Batchelor flow type. the variable Cq_r can be expressed through the following equation, where Q_t is the volumetric flow rate:

$$Cq_r = \frac{Q_t \, {Re_{\theta,r}}^{1/5}}{2\pi r^3 \omega} \tag{1}$$

In a further study [30], Poncet et al. studied the transition of the flow from Batchelor to Stewartson type under the influence of superimposed through flow, it was found that the direction of the through-flow is determinant of the type of the flow. Superimposed centripetal flow kept the flow of Batchelor type while it had faster core rotation than in case of closed system Batchelor flow. Also, the transition from Batchelor to Stewartson was characterized using Rossby number, *Ro,* considering the radial position in the gap according to Fig. 2-3.

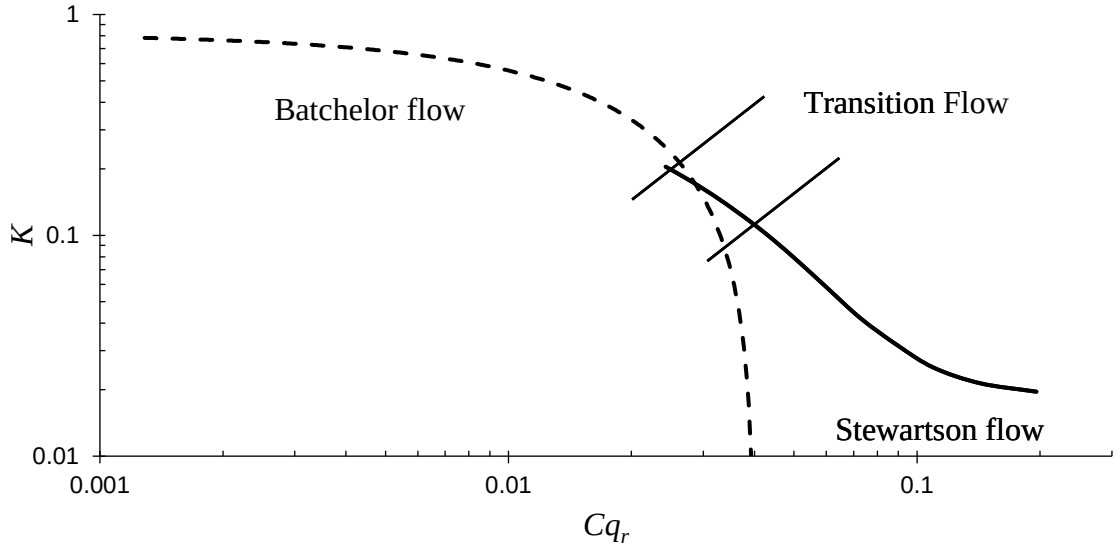

Fig. 2-2 Flow type dependency on local flow coefficient, Cq_r. [29]

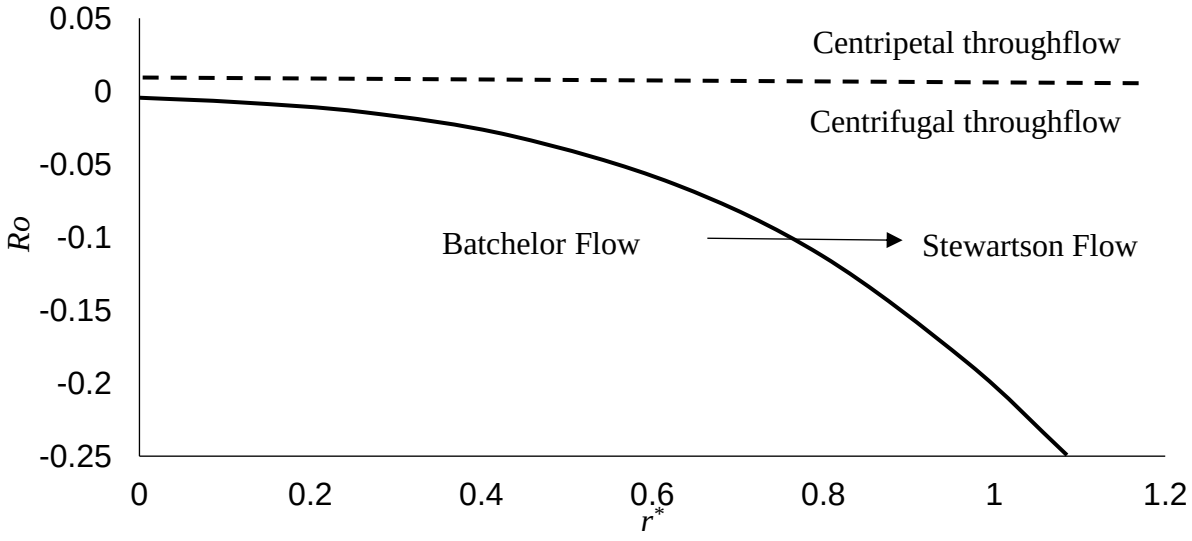

Fig. 2-3 Flow type characterization as a function of Rossby number, Ro. [30]

2.2 Heat Transfer in Rotating Disks

Cobb and Saunders [31] derived correlations for the mean Nusselt number on a free rotor based on experiments run on a heated rotating disk for both turbulent and laminar flows, with the transition recorded at $Re_\theta \approx$ 2.4e5. For laminar flow over laminar flow over a free rotor, the average mean Nusselt number can be calculated using this equation:

$$\overline{Nu} = 0.36\, Re_\theta{}^{0.5} \tag{2}$$

While for turbulent flow, the mean Nusselt number equation can be expressed as follows:

$$\overline{Nu} = 0.015\, Re_\theta{}^{0.8} \tag{3}$$

Dorfman [32] argued the existence of a relation between the surface temperature distribution over a free rotating disk and the convective heat transfer. Accordingly, for a temperature profile of:

$$T(r) = T_\infty + cr^n \tag{4}$$

The heat transfer for a laminar flow can be expressed through the local Nusselt number Nu_r equation given below for $Re \leq 1.82 \times 10^5$:

$$Nu_r = 0.308\, f(Pr)\sqrt{n+2}\, (Re_{\theta,r})^{0.5} \tag{5}$$

While for turbulent flow (Pr = 0.72) for $Re \leq 2.82 \times 10^5$:

$$Nu_r = 0.0197\, (n+2.6)^{0.2} Pr^{0.6} \left(Re_{\theta,r}\right)^{0.8} \tag{6}$$

The correlations provided by Cobb and Saunders, and Dorfman are only applicable for a heated free disk only, however, these correlations are not enough for representing the heat transfer in an AFPM machine rotor given the small clearances around it. Owen and Rogers [28] defined a limit for gap ratio over which the stator influence on the air gap flow can be neglected and the rotor can be assumed as a free disk.

This limit is a function of the rotational Reynolds number and can be calculated through the following equation:

$$G_{lim} = 1.05\, Re^{-0.2} \tag{7}$$

This ratio is found to be higher than most of the clearances ratios around the rotor in our machine, therefore, free disk heat transfer equations cannot be utilized and heat transfer in rotor-stator systems has to be studied.

For fully enclosed shrouded rotor-stator systems, Owen and Rogers [28] analytically derived four mean Nusselt Number correlations corresponding to each of the four flow regimes discussed by Daily and Nece [27], and they are listed in order from regime I to IV as follows:

$$\overline{Nu} = G^{-1} \tag{8}$$

$$\overline{Nu} = \frac{1.85}{\pi} G^{1/10} {Re_\theta}^{1/2} \tag{9}$$

$$\overline{Nu} = \frac{0.04}{\pi} G^{-1/6} {Re_\theta}^{3/4} \tag{10}$$

$$\overline{Nu} = \frac{0.051}{\pi} G^{1/10} {Re_\theta}^{4/5} \tag{11}$$

Where the mean Nusselt number was related to the correlations presented in [27] for the dimensionless moment coefficient on one side of the rotor, C_m, through the equation below:

$$\overline{Nu} = \frac{Re\ C_m}{\pi} \tag{12}$$

The correlations for C_m were driven for a range of Reynolds number between 10^3 to 10^7 and gap ratios G = 0.217, 0.115, 0.0637, 0.0255 and 0.0127. These ranges are applicable for the $\overline{Nu}$ values based on it for a rotor surface of a temperature profile ($T(r) = T_\infty + cr^2$) facing a stator of constant temperature equals T_∞.

Soo [33] analytically studied the heat transfer for a laminar flow in a shrouded rotor-stator system with an imposed inflow/outflow at the center at different pumping rates. The study concluded that a net outward flow in the air gap is more beneficial for the rotor heat transfer compared to inward flow.

Kapinos [34] performed an experimental study for an unshrouded rotor-stator system with a throughflow superimposed at the center. The studied flow corresponded to turbulent regime IV from Daily and Nece's study. The correlations below of the mean Nusselt number over the rotor surface at the air gap for turbulent air flow (Pr=0.72) at different air gap ratios (G=0.016-0.065) was driven based on the experiment results:

$$\overline{Nu} = 0.0346\, {X_a}^{0.3} G^{0.06} {K_v}^{-0.1} {Re_\theta}^{0.8} \tag{13}$$

where, K_v is a parameter calculated as a function of the imposed volumetric flow rate, and X_a is the ratio between the inner and outer radii of the studied air gap.

Owen [35] further studied the rotor heat transfer with superimposed flow at the center of the stator in an unshrouded system. A correlation for the local Nusselt number was derived analytically and the mean Nusselt values agreed with Kapinos experimental results at a high Reynolds number. The study concluded that the superimposed flow has increased the system heat transfer when compared to a free disk. While this increase is dependent on the imposed mass flow rate, rotational speed, and air gap ratio. The study also suggests that the convective heat transfer is found more dependent on the mass flow rate and less dependent on Reynolds number values at low Reynolds number for G<0.06. this was found agreeing with the experimental results from [35] and [36]. In another study [37], the dependency of heat transfer on mass flow rate was related to the radial to rotational Reynolds number ratio, Re_r. A flow of Re_r higher than 0.875 has the rotor heat transfer mostly dependent on the mass flow rate. Where Re_r can be expressed by the equation below:

$$Re_r = \frac{C_w}{2\pi G Re} \tag{14}$$

And, C_w is the non-dimensional mass flow rate expressed as:

$$C_w = \frac{\dot{m}}{\mu R} \tag{15}$$

Boutarfa and Harmand [38] studied heat transfer in an isothermal, unshrouded rotor-stator system experimentally. The studied setup had an opening in at the stator center allowing for throughflow naturally pumped through the rotor movement without superimposing additional air flow. The study is carried for at a range of rotational Reynolds number 5.87e4< Re_θ<1.4e6,

at G = 0.01, 0.02, 0.06 and 0.17. The study reported the correlations shown below for local and mean Nusselt number for different combinations of Re_θ and G.

For laminar flow and G=0.01:

$$\overline{Nu} = 7.46\ Re_\theta{}^{0.32} \tag{16}$$

when $0.02 \leq G \leq 0.06$:

$$\overline{Nu} = 0.5(1 + 5.47 \times 10^{-4}\ \mathrm{e}^{112\mathrm{G}})Re_\theta{}^{0.5} \tag{17}$$

when $G \geq 0.06$:

$$\overline{Nu} = 0.55(1 + 0.462 \times 10^{-4}\ \mathrm{e}^{-13\mathrm{G}/3})Re_\theta{}^{0.5} \tag{18}$$

in case of free disk:

$$\overline{Nu} = 0.55\ Re_\theta{}^{0.5} \tag{19}$$

For turbulent flow and G=0.01:

$$\overline{Nu} = 0.044\ Re_\theta{}^{0.75} \tag{20}$$

when $0.02 \leq G \leq 0.06$:

$$\overline{Nu} = 0.033(12.57\ \mathrm{e}^{-33.18\mathrm{G}})Re_\theta{}^{3/5+25\mathrm{G}^{12/7}} \tag{21}$$

when $G \geq 0.06$:

$$\overline{Nu} = 0.0208(1 + 0.298\ \mathrm{e}^{-9.27\mathrm{G}})Re_\theta{}^{0.8} \tag{22}$$

in case of free disk:

$$\overline{Nu} = 0.0208\ Re_\theta{}^{0.8} \tag{23}$$

The results showed the throughflow allowed through the stator opening increased the Nusselt number values on the rotor surface regardless of the Re_θ and G values when compared to closed systems. The study also showed that for G = 0.01 the Nusselt number over the rotor is nearly constant across the air gap, agreeing with Owen and Rogers [28], with a higher mean value compared to larger gap ratios at the same Re_θ. The author related the reduced mean Nusselt number in higher gap ratios to the fact that they result in lower air flow rate and Batchelor flow structure across the air gap. They explained that for G = 0.01, the flow in the air gap is dominated by the viscous forces resulting in a Couette flow type filling the entire gap, similar to regime I and III discussed by Daily and Nece [27]. This results in a higher rate of heat transfer at the inner radii where the boundary layer thickness is relatively small. As the flow progress to the gap periphery, the boundary layer thickness increase, and viscous forces become more significant which deteriorates the heat transfer. Moreover, the air temperature increase as it flows radially reaching temperatures close to that of the rotor surface, which further deteriorates the heat transfer. Accordingly, the local heat transfer coefficient decreases proportionally with the radius. The figure below (Fig. 2-4) shows the effect of different gap ratios on the measured local heat transfer across the air gap at Re_θ = 2.34e5. It is worth noting that the authors defined the laminar-turbulent transition region based on the Rotational Reynolds number, Re_θ, between 1.76e5 and 3.52e5, these values agree with the results from [39].

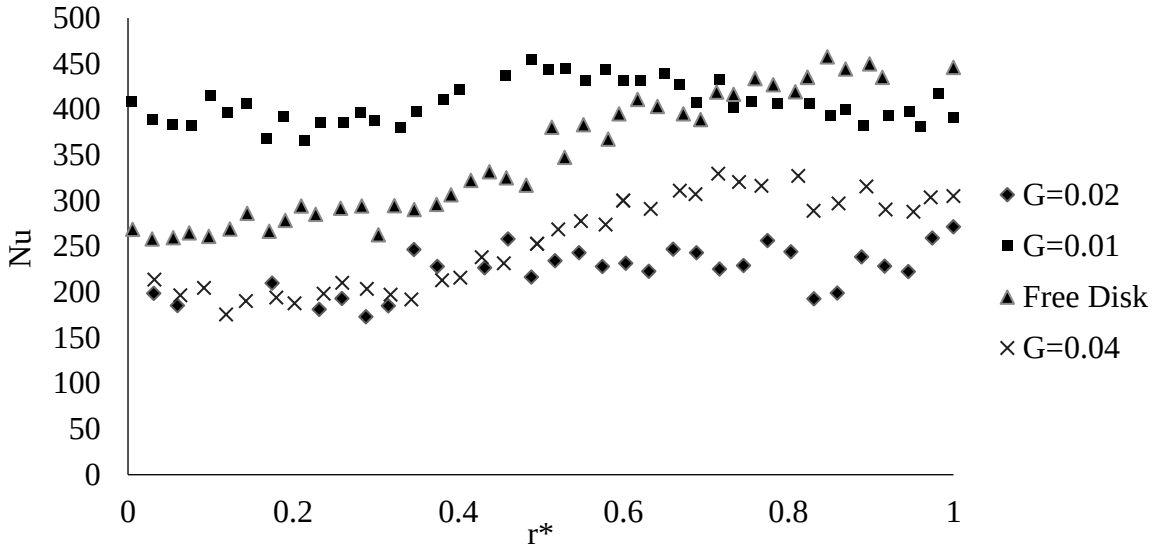

Fig. 2-4 Local Nusselt number on the rotor for different G values at Re_θ = 2.34e5 [38].

The figure below (Fig. 2-5) shows the mean Nusselt number at different Reynolds number values and gap ratios, it is noticed that the heat transfer increases significantly as soon as the flow reaches the transition region, also a trend can be seen where the heat transfer significantly drops for gap ratios, *G*, between 0.01 and 0.06 regardless of the Reynolds number value.

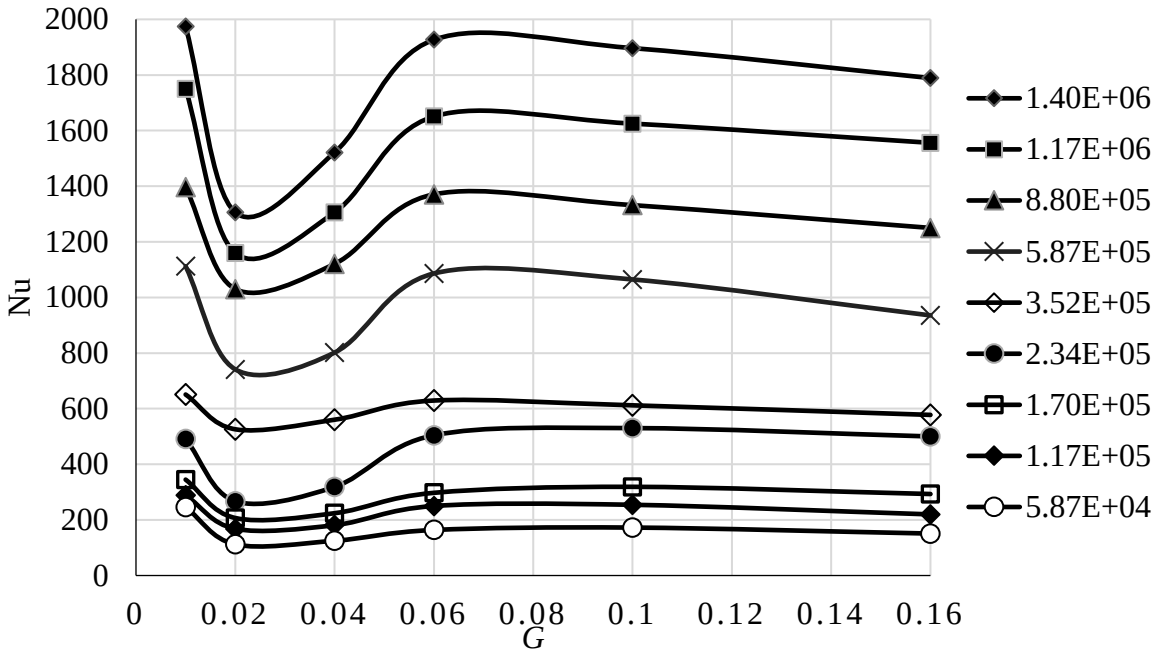

Fig. 2-5 Mean Nusselt number as a function of $Re_{\theta,}$ and G [38].

This research will be focusing on studying the thermal behavior of turbulent flows in small air gap ratios (G<0.01) given the operating conditions and the electrical design of AFPM machines which favors having a narrower air gap to maximize electromagnetic torque as a result of higher inductance [40] [10]. Also, the enhanced heat transfer associated with G<0.01 as presented in [38].

Rasekh et al. [41] provided a comprehensive numerical study for the heat transfer in AFPM machines. The study was carried out for an unshrouded rotor-stator assembly with an axial opening in the rotor for throughflow ventilation. Moreover, the rotor had surface-mounted magnets poles with annular air channels in between each pair acting as a centrifugal fan and enhancing the system air flow, hence the heat transfer. Multiple parameters were varied in the study and correlations for mean Nusselt number were derived accordingly. The correlations

constants are optimized so that their results are independent of the system dimensions and ambient temperature. The results showed that the magnets (rotor surface) heat transfer is directly proportional with the air gap ratio, opposing the results from [28] and [38]. Perhaps the difference in results is due to, first, the major difference between the studied rotor geometries, second, the fact that the existence of annular air channels affects the flow field at the air gap as they become the main air flow passage in the system according to the results presented by Howey et al. [42] and Airoldi et. al [43].

2.3 Rotor Thermal Modeling in AFPM Machines

Despite the large body of literature concerning the heat transfer over rotating surfaces in rotor-stator systems, few studies are found regarding rotor cooling in AFPM machines in particular, compared to the subject of stator cooling which is found to be very well researched. Alternatively, the average convective heat transfer coefficient is used in lumped parameter thermal models for studying the machine thermal performance. Fawzal [44] reviewed previous studies that used lumped parameter methods in studying AFPM machines and concluded that, while they offer a fast way to estimate the machine overall thermal performance, solely relying on this method can be of considerable drawbacks. The shortcomings of the lumped thermal parameters are usually brought back to their inability to account for the actual machine geometry, reducing it to few nodal points which neglects the spatial variation in temperature due to variation in surface properties. Additionally, the systematic inaccuracies due to the utilization of correlated values of contact resistances and convective heat transfer coefficients that are usually based on unalike geometries and operating conditions from previous studies. Although few studies reported high accuracy of lumped parameter thermal models when compared to experimental results [45] [46] [47] [48], the solution accuracy can be strongly affected in machines of highly complex surface features when it comes to airflow modeling as suggested in [49].

2.3.1 Numerical thermal modeling

Numerical simulations overcome the discussed shortcomings of lumped parameters thermal models as the exact geometry of the machine can be modeled and discretized into a finite number of elements at which energy equation can be solved. This results in increased solution

accuracy, besides the ability to capture the spatial variation of different thermal properties at the surface as well as the core of the machine components. This allows machine designers to address potential failure points due to local thermal hot spots as discussed in [50].

Many studies on numerical thermal modeling of AFPM machines can be found in literature. The simpler type of numerical thermal simulations involving using Finite Element Analysis (FEA) offers superior accuracy over the lumped parameter thermal models in terms of spatial variation of thermal properties in the machine core. Nevertheless, some of the studies still used the averaged flow properties for surface boundary conditions which compromises the solution accuracy. In the study done by Wang et al. [50], although targeting detailed thermal analysis of the rotor using FEA model, averaged heat transfer coefficients based on mean Nusselt number correlation from [51] and [52]. The FEA model allowed for a more accurate distribution of losses in the magnets accounting only for the effect of electromagnetic losses density on the spatial temperature distribution. However, the effect of spatial variation of thermal properties on the rotor surface was not captured.

A more complex and computationally demanding numerical analysis involves computationally fluid dynamics (CFD). This type of numerical analysis captures the spatial variation of surface properties through modeling of the fluid flow over the machine surfaces and the influence of different features and operating conditions on it. This level of accuracy, however, comes at a high computational cost due to the higher count and complexity of the equations solved per each element in the finite element grid as will be discussed in the next chapter.

Most of the CFD studies done on AFPM machines that are discussed in literature are focused on thermal modeling of the stator. Airoldi et al. [53] [43] and Howey [54][55] studied the effects of surface-mounted protruding magnets in through-flow ventilated machines with the vents located on the stator side. They only presented correlations that predict the heat transfer coefficient at the stator at different air gap ratios. However, both studies did not consider the effects on rotor heat transfer. While Howey et al. relied on correlations from [38] to predict the heat transfer on the rotor side. Fewer studies are found discussing the rotor side. The most recognized studies done regarding the rotor cooling are those done by Rasekh et al. [41] [56][57], and Fawzal et al. [58] [59][60]. Prior to these studies, Hey et al. [61] discussed using

a hybrid method utilizing both lumped parameter analysis and FEA to predict the transient thermal behavior in an AFPM machine. CFD simulations are also used to determine the average heat transfer coefficient for the modeled enclosed machine geometry as correlations from literature were found to be not directly applicable to the presented geometry in their work. The heat transfer coefficients obtained from the CFD simulations are then used as boundary conditions in the lumped parameter thermal network. The results of the hybrid thermal model agreed well with the experimental data when validated and the maximum error recorded was 3.4% at the end windings. On a further study [62], the model accuracy was further improved by applying Monte Carlo optimization method, achieving 53% less temperature deviation. Despite the high accuracy of the model, its efficiency compared to exclusive CFD solutions can be argued in case of more complex geometry.

2.4 Approaches for Rotor Air Cooling Enhancement

Cooling the rotor predominantly by air limits the cooling capacity since the cooling rate is dictated by the rotor geometry and operating speed. Nevertheless, air cooling has the advantage of being a simple and less power-consuming rotor cooling method compared to other methods such as phase change and liquid cooling [13]. The air cooling rate can be maximized at the same operating conditions by improving the rotor geometry to enhance the airflow over the rotor surfaces.

Many researchers have studied the airflow in AFPM machine rotating assembly and its effects on heat transfer and cooling in general. The following sections discuss the main utilized approaches for rotor cooling improvement found in literature.

2.4.1 Ventilated rotor

Rasekh et. al [56] studied the air flow in a discoidal rotor-stator system at a range of rotational Reynolds number $2.5e10^4 \leq Re_\theta \leq 2.5e10^5$, and air gap ratios G=0.0067, 0.0133, and 0.02667. The study found that the presence of vents/holes in the rotor body allows for a net radial outflow at the air gap. Hence, increasing the air gap heat transfer effect. However, the study did not quantify or measure the claimed enhancement compared to a non-vented rotor. Airoldi et. al [43] also argued the benefit of having air admitted through the rotating rotor boss (hub) at the center on the stator heat transfer. However, the enhancement was also not

quantified. Chong et al. [63] discussed the effect of rotor axial, as well as, radial holes in an air cooled AFPM machine. The study showed a significant increase in the throughflow mass flow rate by introducing the holes, which enhanced the stator cooling in result. Similar to Airoldi et al. study, the effect of the holes rotor cooling was not assessed in this study.

2.4.2 Surface-mounted protruding magnets

The effect of surface-mounted protruding magnets on cooling heat transfer in AFPM machines was investigated by Airoldi et al. [43]. The thickness of the surface-mounted magnets and the rotational speed were varied in a validated CFD model. The study found that increasing the height of the channels in between the magnets increased the pumping capacity of the rotor and the resulting windage losses consequently (shown in Fig. 2-6). This effect resulted in enhanced the heat transfer on the stator side. Howey et al. [54] conducted a similar experimental study with two rotor configurations, one with surface protrusions and another with a flat rotor surface (without protrusions). The study concluded that the average heat transfer on the stator side was increased by 20%-30% at similar operating conditions.

Rasekh et al. [41] studied rotor protrusions in AFPM numerically. Unlike the geometries presented in Airoldi et al. and Howey et al. work, the machine was throughflow ventilated through annular openings (channels) in the rotor. The geometry of the magnets, gap ratio, and rotational speed were varied in the study. The effect of each parameter on the heat transfer in the stator and the rotor was studied. The results showed that the overall machine heat transfer can improve substantially, especially on the magnets, by having both the rotor protrusions and the rotor openings simultaneously featured in the design. It can be argued that rotor protrusions are only effective in throughflow ventilated machines, hence, the author emphasized on the equal importance of both features in the design for enhanced cooling.

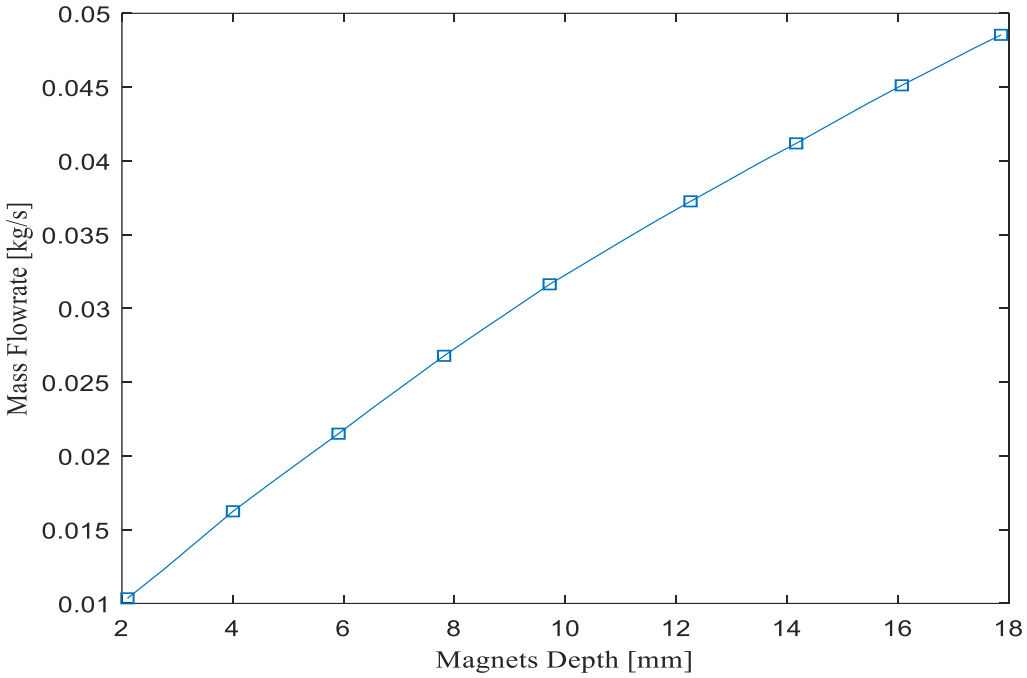

Fig. 2-6 Effect of the protruding magnets depthon total through flow mass flow rate [43]

2.4.3 Rotor embedded radial fan

In the efforts to maximize the rotor cooling AFPM, Vansompel [64] suggested the addition of fan blades to the back side of the rotor to enhance the rotor heat transfer and structural rigidity. Fawzal et al. [58][59]studied the implementation of this concept. Three fan geometries (backward curved, radial, and tear drop pillar blade) from other applications were investigated. Each geometry was modeled separately as an embedded fan section in an AFPM rotor. The performance of each fan design was judged based on the cooling capacity, pumping capacity, pressure development, and windage losses. The study was done numerically using a validated CFD model of the machine. Although the study showed an enhanced cooling performance of bladed rotor design in general, this enhancement was not quantified. The results, however, showed that the backward inclined had the best thermal performance among other geometries since it provides high cooling capacity at low additional windage losses. The radial blade, on the other hand, offered slightly better cooling capacity, but at high cost of added windage losses. The authors introduced an index , Rotor Cooling Performance Index (RCPI), for comparison of different designs based on their convective cooling capacity and

windage losses. The index can be expressed using the equation below. Despite being helpful for ranking of designs based two of the most important rotor design parameters, the index is calculated at equal temperatures of the rotor across all designs, hence, inconsistent thermal load. Accordingly, the index comparison might not be directly applicable when comparing designs at constant thermal load.

On a further study, Fawzal et al. [60] studied the inlet and outlet arrangement for the rotor air cooling system and its effect on the machine thermal performance. Three arrangements where the locations and shape of inlet and outlet ports were varied. The first arrangement had a radial inlet and radial outlet, the second design had a tangential inlet and tangential outlet, finally the third design had an axial inlet and tangential outlet. The three designs were modeled and simulated using CFD, where equal mass flow rates are prescribed at the inlet in all simulations. The axial inlet-tangential outlet design was found to result in the lowest pressure losses and significantly higher average heat transfer coefficient over the rotor at comparable windage losses values compared to the other designs.

Chapter 3

Computational Fluid Dynamics Modeling

3 Computational Fluid Dynamics Modeling

The complexity of solution of the flow and heat transfer over rotating bodies usually mandates equally complex approaches. The studies in literature shown in the previous chapter adopted analytical, computational, and experimental approaches or even hybrid methods to reach a simplified solution for the presented cases at an acceptable level of accuracy. Most of the presented solutions are mainly concerned with the surface properties of the studied geometries under certain conditions; Alternatively, internal thermal behavior of the rotating body is usually assessed using Lumped Parameter (LP) thermal networks for a fast, yet less accurate solution. Although this approach might be sufficient in certain cases, it might not capture the full effect of local variations of the surface parameters on the internal thermals.

In AFPM machines, permanent magnets demagnetization and debonding due to adhesive failure due to magnets overheating are highly two concerning risks when it comes to the rotor design; Accordingly, assessment of the internal temperature distribution can be of great benefit for the machine thermal management and determination of machine continuous operation load. As discussed earlier, relying just on lumped parameter thermal networks and analytical calculations might not yield an accurate estimation of the machine thermal behavior in some cases due to the following reasons:

1. The permanent magnets on the machine rotor of an AFPM machine rotor are prone to developing local hot spots due to different factors that will be discussed in the next chapter. Local hot spots in the magnets might not be captured using a lumped thermal network that leads to inaccurate estimation of the magnets operating temperature.
2. The correlations from literature often used to determine the boundary conditions for a thermal network are highly dependent on other factors that vary from one machine design to another such as (magnets arrangement, rotor geometry, air path routing, overall measurements of the machine...etc.).Therefore, a detailed Computational Fluid Dynamics (CFD) simulation of the flow for the designed machine considering its geometry and operating conditions is necessary to accurately assess its thermal behavior.
3. Losses generated in the rotor are often represented by approximated constant temperature or evenly distributed heat flux boundary conditions at the rotor surfaces in order to solve for the averaged heat transfer coefficient values at these surfaces that are then plugged into the LP thermal network. This reduces the accuracy of the solution of the rotor thermals.

Conjugate Heat Transfer (CHT) CFD rotational model is used for this research to avoid the inaccuracies and limitations imposed by using alternative approaches as discussed earlier. CHT models can simultaneously simulate the fluid flow as well as the heat transfer in the immersed solid domains. This approach eliminates the need for using LP thermal networks, averaged surface properties, approximate boundary conditions. In combination with the ability of the turbulence models to solve for mass flow and other surface flow properties in rotating assemblies at a high level of accuracy [44], using CHT models to simulate thermal losses in AFPM machines rotors can yield a highly accurate estimation of the machine thermals that can greatly help in the design process of thermal management solutions for the machine.

3.1 Geometrical Setup

The setup of the geometry for the machine assembly shown in Ch. 2 requires having a geometrical setup that allows for CHT rotational modeling of the rotor. The CHT model setup demands full representation of the parts of the solid domain that affects the rotor assembly heat transfer through either heating or cooling; Additionally, the fluid domain surrounding the rotor to which the heat is transferred through the interfaces of the two domains.

As previously discussed in Ch.2, the major sources of thermal losses in the rotor ordered from highest to lowest are:

1. Permanent magnets, due to eddy current losses.
2. Rotor Bearings, due to friction.
3. Stator, due to heat losses in the stator core. Heat is transferred from the stat

While minor heat losses can also occur in:

4. Back iron, due to eddy-current losses.
5. Rotor Carrier, in case of using a material of higher relative permeability where eddy currents can be generated.

These four parts of the rotor assembly hence must be included in the simulated solid domain so that the thermal losses in each are applied as a loss density (W/m^3) directly to the corresponding solid body in the simulation.

3.1.1 Geometry Simplifications

The exact geometry of the simulated machine may include parts or features that serve a purpose in the mechanical or the electrical design, but they may be irrelevant or have a negligible effect on the thermal design; Including such elements may unnecessarily increase the size and complexity of the modeled geometry. In efforts to maintain good quality, robustness, accuracy, and computational cost of the CFD simulation, few simplifications have to be made in the simulated solid and fluid domains geometries without compromising the model accuracy.

As a general approach for computational domain size reduction, the smallest representative angular periodic sector of the machine is utilized for base rotor geometry studies rather than simulating the full 360° assembly of the machine which is highly computationally expensive compared to the former approach. Nevertheless, modeling of the full assembly is used for studying the non-axisymmetric cover geometries that might affect the rotor performance as will be discussed later.

3.1.1.1 Solid domain simplifications

a. Rotor bearings

The rotor bearing is reduced into a simple surface at the rotor carrier inner diameter resembling the interface between the bearing hub and the rotor carrier. This approximation is justified based on the following reasons:

1. The rotor bearings are located in a semi-enclosed region where it is not directly cooled by the main stream of the air over the rotor, however, the heat losses generated in the bearing are cooled indirectly through both the stator and the rotor. Therefore, only the resultant heat flux at the bearing interface with the rotor carrier can be considered.
2. The bearing thermals are not an area of interest in this research. Hence, only its effect on the rotor thermal performance is assessed.
3. Heat is transferred from the bearings to the rotor carrier by conduction at a relatively small interface area between the carrier and the bearing hub compared to the rotor surface area.

   This means that variations of the heat flux at the hub-carrier interface are expected to be minimal and the losses can be assumed as a uniform heat flux over that interface area.

The approximation of the bearing interface allows results in a simpler and smaller size of both solid and fluid domains.

b. Magnets and back iron

The rotor solid domain is further simplified by reducing the Halbach magnet array into a single solid body. This simplification is based on the assumption that the heat transfer within the magnets poles is nearly two-dimensional, with negligible heat conduction in the circumferential direction. This is due to the following reasons:

1. The potting material of a very low thermal conductivity (< 2 W/m.K) between the magnet poles nearly prevents the heat transfer between the magnets poles.
2. The small width of the Halbach magnets segments combined with the relatively low thermal conductivity of Neodymium magnets results in negligible circumferential variation in the temperature within a single segment.
3. At a continuous operation of the machine, all the magnet segments will eventually reach nearly equal steady state temperature distribution given the high rotational speed of the machine with respect to the large thermal time constant of the magnets due to its low conductivity. This means no heat transfer between two magnets parallel segments in the circumferential direction is expected.

The same simplification approach is applied to the back iron segments considering the comparable thermal conductivity of the back iron steel to that of Neodymium magnets.

c. Rotor carrier

The simplifications in the rotor carrier geometries discussed in this research are limited to the elimination of some of the features that are mostly related to the structural design that are rather irrelevant to the thermal design. Some of these features are:

1. Rotor bolts counterbores

Although protruding bolts heads near the rotor impeller eye can be of great concern to the rotor thermal performance as discussed in [65], the bolt heads in the rotor carrier designs presented in this thesis are designed to sit flush in counterbores in the rotor carrier body. This design alleviates the potential blockage of the flow area at the impeller eye by the protruding bolts heads. Accordingly, the rotor carriers are simplified into a solid body where the small recesses between the bolts heads and their counterbores are neglected.

2. Resolver target.

The resolver target is eliminated from the simulations in this research for simplification of both the rotor carrier and cover geometry. This is given that the resolver placement is set to have minimal interference with the main stream of the cooling air over the rotor.

3. Rotor enclosure.

The rotor enclosure is modeled as a simple wall for the simulations done for the initial phase of the rotor design to set up its base design and dimensions. Finally, the enclosure design and the rotor design are fine-tuned simultaneously for a more refined thermal performance as will be discussed later in the results section. It is also worth mentioning that in all the simulations the enclosure wall is modeled as an adiabatic wall. These boundary conditions allow for modeling the air flow only on the rotor side of the enclosure wall, resulting in a smaller size of the required fluid domain. Although the enclosure heat transfer can have a significant influence on the rotor thermal performance [44], the relatively small temperature difference between the ambient temperature outside and the bulk temperature of the air inside the enclose combined with the low thermal conductivity of the plastic machine cover result in negligible heat flux through the enclosure walls which justifies such assumption.

4. Stator core

The stator core is simplified as a stationary wall in the simulations due to the complexity of its geometry. The designed machine has a liquid cooled stator; hence it does not rely on the air on the rotor side for cooling the stator. The contribution of the air in stator cooling is considered negligible in comparison to the liquid cooling system, therefore, approximate representation of the stator air side is deemed sufficient for the rotor simulation. Moreover, this approach was justified in previous studies discussed in literature. [57]

3.1.1.2 Fluid domain simplifications

The fluid domain simplifications are rather straightforward compared to the solid domain. The simplifications process target is to minimize the fluid domain size as much as possible without affecting the simulation accuracy or robustness.

Axisymmetric periodic computational domains were discussed in previous studies [41][42]. However, most of these studies were targeted towards studying the heat transfer the air gap with; Accordingly, the studied computational domains sizes were limited to magnets side of the rotor only. The computational domain geometry presented in the study done by Rasekh et

al. [41] was modeled to solve for heat transfer coefficients for an uncovered rotor assembly. Although the solid domain was not included in their study, the presented geometry is found to have the closest representation required for the CHT modeling of the rotor given the comparable assembly of the rotor. The fluid domain in the referenced study was modeled as an axisymmetric pie-shaped periodic sector with atmospheric opening boundary conditions at a distance equal to six times the rotor radius away from the nearest walls.

A similar approach with the computational domain is initially used, while modifications are done later to improve the model convergence and reduce the fluid domain size as shown in Fig. 3-1. Also, the solid domain is included to allow for CHT modeling of the rotor. The fluid domain size is reduced by eliminating the part of the domain that does not influence the flow due to the existence of the cover. The excluded part of the domain is replaced by opening boundary conditions near the flow exit at the periphery to allow for air entrainment, whereas on the inlet side it is replaced by slip walls at the extended inlet to keep the inlet far enough from the real inlet at the cover. Additionally, the extents of the fluid domain are brought closer to the rotor through multiple iterations to finally set the inlet at a distance of 1R from the rotor, while the outlet is set at a distance of 3R from the external cover wall. Where R is the radius of the simulated rotor.

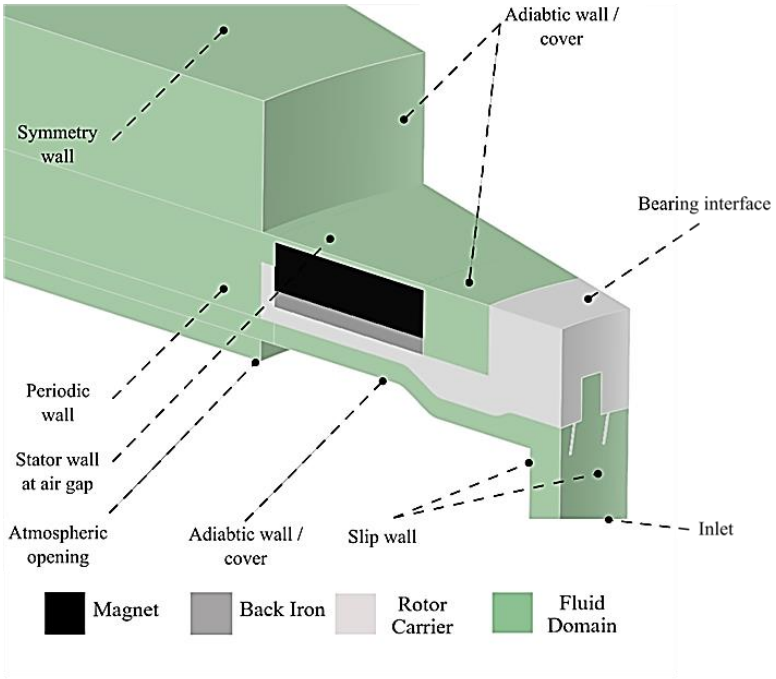

Fig. 3-1 General representation of the computational domain used for sectional periodic simulations and the specified boundaries.

3.1.2 Rotational Modeling Considerations

The rotational CFD modeling for the rotor requires multiple considerations when it comes to setting up the computational domain geometry. Rotational modeling can also involve more than one frame of reference; Accordingly, this influences the geometrical setup of the computational domain so that it allows assigning different parts of the domain to its relevant frame of reference whether it is rotating or stationary. The following are the two approaches used for rotational modeling in this research and the associated geometrical considerations:

1. Single Rotating Reference Frame (SRF)

SRF approach for rotational modeling has a single rotating domain. The entire CFD domain in this model rotates about a single axis defined in the stationary frame. Therefore, the defined axis of rotation must be the same axis of symmetry for an axisymmetric rotor geometry.

The SRF models allow for the use of different domains boundaries including inlet and outlets surfaces, periodic boundaries, and walls. However, some considerations must be maintained. First, periodic boundaries of the flow must reflect the periodicity of the modeled geometry. Second, the angles between the periodic boundaries must be evenly divisible into 360°. Lastly, the stationary walls, inlets, and outlets boundaries must be axisymmetric surfaces of revolution about the same axis as the rotating reference frame axis.

2. Multiple Frames of Reference (MFR)

The MFR models fluid domain with one domain rotating relative to another stationary domain with each domain having a separate frame of reference. This approach inherently requires the computational fluid domain to be split into two separate parts. The interface where the two domains connect can affect the solution and convergence behavior. Accordingly, some considerations must be maintained to ensure the correct setup of the fluid domains interface. First, the interface between the two domains should be a surface of revolution. Secondly, all the boundaries that are contained in the rotating domain must follow the same boundaries consideration of SRF models. Lastly, non-conformal meshes at the interface has special considerations, especially when used with periodic boundaries. This is mitigated by using a conformal interface for better solution accuracy.[66]

The different approaches of rotational modeling for steady state and transient solutions will be discussed in detail later in this chapter.

3.2 Governing Equations

A CFD simulation is defined through the geometry of the simulated body, the domain of the fluid affected by the body, the conditions of the fluid at its defined boundaries, and a set of governing equations that are used to model the physics involved within the defined computational domain. The computational domain is then discretized to infinitesimally small elements or control volumes that allow solving the governing equations numerically through a number of iterations.

The number and the form of the governing equations needed to solve for the flow in a CFD simulation vary from one case to another depending on the selected physics to be analyzed, the level of accuracy required for the analysis, and the available computational resources. Accordingly, the number of governing equations that are solved can be reduced to reflect only the physics desired to be captured. Moreover, the selected equations can be further simplified based on reasonable assumptions about the flow behavior. This will eventually result in reduced simulation time, less computational resources, and increased model robustness.

ANSYS CFX solver is used for the AFPM rotor simulations in this work. The governing equations solved by the solver are best represented by the unsteady conservation forms of Navier-Stokes equations. The equations are modified and simplified given the operating conditions and the geometry of the domain through the solver Graphical User Interface GUI. The summary of the equations and the simplifications made are presented below.

3.2.1 Navier-Stokes equations

3.2.1.1 Continuity equation

The continuity equation is the base equation for the representation of fluid motion ensuring mass conservation. The continuity equation on a given control volume can be written as follows:

$$\frac{\partial \rho}{\partial t} + \nabla \cdot (\rho U) = 0 \tag{24}$$

Where U is the fluid velocity at any given point in the computational domain. In case of a steady state, the transient term in the equation becomes $\partial\rho/\partial t = 0$. Also, considering that the flow is incompressible the equation is further reduced into:

$$\nabla \cdot U = 0 \tag{25}$$

The representation of the continuity equation in the cartesian coordinate system hence becomes:

$$\frac{\partial \rho}{\partial t} + \frac{\partial (\rho u)}{\partial x} + \frac{\partial (\rho v)}{\partial y} + \frac{\partial (\rho w)}{\partial z} = 0 \tag{26}$$

Similarly, for a steady state incompressible flow:

$$\frac{\partial u}{\partial x} + \frac{\partial v}{\partial y} + \frac{\partial w}{\partial z} = 0 \tag{27}$$

3.2.1.2 Momentum equation

The momentum equations described in Navier-Stokes governing equations conserve the momentum in a given control volume through balancing the pressure and shear forces acting on it with the net momentum due to fluid acceleration. The conservation of momentum hence can be written as follows:

$$\frac{\partial (\rho U)}{\partial t} + \nabla \cdot (\rho U \times U) = -\nabla p + \nabla \cdot \tau + S_M \tag{28}$$

For a cartesian coordinate system for a three-dimensional flow, the momentum equations become:

a. x-momentum:

$$\frac{\partial (\rho u)}{\partial t} + \frac{\partial (\rho u u)}{\partial x} + \frac{\partial (\rho v u)}{\partial y} + \frac{\partial (\rho u w)}{\partial z} = -\frac{\partial p}{\partial x} + \frac{\tau_{xx}}{\partial x} + \frac{\tau_{xy}}{\partial y} + \frac{\tau_{xz}}{\partial z} + S_{Mx} \tag{29}$$

b. y-momentum

$$\frac{\partial (\rho v)}{\partial t} + \frac{\partial (\rho u v)}{\partial x} + \frac{\partial (\rho v v)}{\partial y} + \frac{\partial (\rho v w)}{\partial z} = -\frac{\partial p}{\partial y} + \frac{\tau_{yx}}{\partial x} + \frac{\tau_{yy}}{\partial y} + \frac{\tau_{yz}}{\partial z} + S_{My} \tag{30}$$

c. z-momentum

$$\frac{\partial (\rho w)}{\partial t} + \frac{\partial (\rho u w)}{\partial x} + \frac{\partial (\rho v w)}{\partial y} + \frac{\partial (\rho w w)}{\partial z} = -\frac{\partial p}{\partial z} + \frac{\tau_{zx}}{\partial x} + \frac{\tau_{zy}}{\partial y} + \frac{\tau_{zz}}{\partial z} + S_{Mz} \tag{31}$$

Accumulation of momentum | Nonlinear Advection | Pressure gradient due to acceleration and shear | Friction / Viscous forces | External momentum sources

Similarly, for a steady state incompressible flow:

a. x-momentum:

$$\rho\left(\frac{\partial(uu)}{\partial x}+\frac{\partial(vu)}{\partial y}+\frac{\partial(uw)}{\partial z}\right)=-\frac{\partial p}{\partial x}+\frac{\tau_{xx}}{\partial x}+\frac{\tau_{xy}}{\partial y}+\frac{\tau_{xz}}{\partial z}+S_{Mx} \quad (32)$$

b. y-momentum

$$\rho\left(\frac{\partial(uv)}{\partial x}+\frac{\partial(vv)}{\partial y}+\frac{\partial(vw)}{\partial z}\right)=-\frac{\partial p}{\partial y}+\frac{\tau_{yx}}{\partial x}+\frac{\tau_{yy}}{\partial y}+\frac{\tau_{yz}}{\partial z}+S_{My} \quad (33)$$

c. z-momentum

$$\rho\left(\frac{\partial(uw)}{\partial x}+\frac{\partial(vw)}{\partial y}+\frac{\partial(ww)}{\partial z}\right)=-\frac{\partial p}{\partial z}+\frac{\tau_{zx}}{\partial x}+\frac{\tau_{zy}}{\partial y}+\frac{\tau_{zz}}{\partial z}+S_{Mz} \quad (34)$$

3.2.1.2.1 Rotational forces in momentum equation

The effect of the flow rotation in the rotating frame in rotational models is accounted for in the source term in the momentum equation. The rotational forces in a rotating flow are equal to the total of the Coriolis force and centrifugal forces as per the following equations:

$$S_M = S_{Coriolis} + S_{centrifugal} \quad (35)$$

where:

$$S_{Coriolis} = -2\rho U \times \omega \quad (36)$$

$$S_{Centrifugal} = -\rho\omega \times (\omega \times r) \quad (37)$$

Where ω is the angular velocity of the rotating frame, U is the relative rotating frame velocity to the rotating frame of reference and r is the location vector.

3.2.1.3 Total energy equation

$$\frac{\partial(\rho E)}{\partial t}+\nabla\cdot(\rho\, U\, H)=\ \nabla\cdot(\lambda\,\nabla\, T)+\nabla\cdot(U.\tau)+U\cdot S_M+S_E \quad (38)$$

Where E is the total energy, related the total enthalpy (H) and pressure by:

$$E = e+\frac{1}{2}U^2 = H-\frac{p}{\rho} \quad (39)$$

While

$$H = h + \frac{1}{2}U^2 \tag{40}$$

Where h is the static enthalpy. The term $\nabla \cdot (U.\tau)$ represent the viscous work, and the term $U \cdot S_M$ represent the work done by external momentum sources.

By subtracting the mechanical energy ($U \cdot Mom\ eq.$) from the total energy equation, this yields the thermal energy equation:

$$\frac{\partial(\rho h)}{\partial t} - \frac{\partial p}{\partial t} + \nabla \cdot (\rho\, U\, h) = \nabla \cdot (\lambda\, \nabla\, T) + U \cdot \nabla p + \tau : \nabla \mathrm{U} + S_E \tag{41}$$

For a flow of low Mach number with a negligible effect of pressure on thermal energy:

$$\underbrace{\frac{\partial(\rho h)}{\partial t}}_{\text{Accumulation of thermal energy}} + \underbrace{\nabla \cdot (\rho\, U\, h)}_{\text{Advection of thermal energy}} = \underbrace{\nabla \cdot (\lambda\, \nabla\, T)}_{\text{Thermal diffusion}} + \underbrace{\tau : \nabla \mathrm{U}}_{\text{Thermal energy generation due to shear stresses}} + \underbrace{S_E}_{\text{Thermal energy from external sources}} \tag{42}$$

By assuming constant gas properties, the thermal energy equation is:

$$\rho C \left(\frac{\partial T}{\partial t} + \nabla \cdot (U\, T) \right) = \nabla \cdot (\lambda\, \nabla\, T) + \tau : \nabla \mathrm{U} + S_E \tag{43}$$

The same equations are used for the rotating frame in a rotational model, however, Rothalpy, I, is used in the advection and the transient terms of the equation instead of Enthalpy, H, where:

$$I = h + \frac{1}{2}U^2 - \frac{1}{2}\omega^2 R^2 \tag{44}$$

3.2.1.4 Conjugate heat transfer (CHT) energy equation

The thermal energy equation can be set for a solid domain similar in order to solve for the heat transport within these domains due to conduction and the existence of volumetric heat sources. The form of thermal energy that is applied to the solid domain can be written as follows:

$$\frac{\partial(\rho h)}{\partial t} = \nabla \cdot (\, C \, \nabla \, T) + S_E \tag{45}$$

3.2.2 Equations of State

The equations of state are used in the model to relate the pressure p, volume V, and temperature T in a continuum through thermodynamic relations to predict its thermodynamic state and properties. A general form of the equations of state can be written as follows:

$$\rho = \rho\,(p, T)\;;\; C_p = C_p\,(p, T) \tag{46}$$

$$dh = \frac{\partial h}{\partial T}\bigg|_p dT + \frac{\partial h}{\partial T}\bigg|_p dp = C_p\, dT + \frac{\partial h}{\partial T}\bigg|_p dp \tag{47}$$

For most of the simulations in this work, air is assumed as a non-compressible fluid of constant properties at ambient conditions. The results are found to be nearly independent of the variations in air properties at the simulated operating conditions. This assumption was justified by other researchers in previous studies [57].

Accordingly, the equation of state is reduced to the following form:

$$\rho = \rho|_{\substack{T_{ambient} \\ p_{ambient}}} \;;\; C_P = C_P|_{\substack{T_{ambient} \\ p_{ambient}}} \tag{48}$$

3.3 Turbulence Modelling

Turbulence is a phenomenon often related to air flow as soon as the flow hit an obstruction, or the velocity exceeds a certain limit (Re>2300) where inertia forces dominate the flow and the damping effect of viscous forces between its layers fails to even out shear-generated instabilities in the velocity field resulting in the formation of eddies of different scales that causes further random fluctuations of the flow velocity and pressure. Due to the low viscosity of air, turbulent flows at relatively low speeds. In this work, the high rotational speed of the machine induces high air flow speeds over the rotor which makes the flow dominantly turbulent over its surfaces. Modeling of the turbulent air flow is therefore of great importance for this research given its high influence on rotor cooling as will be discussed in the next chapter.

Turbulence can be directly modeled through Navier-Stokes equations applied on extremely fine mesh elements in a Direct Numerical Simulation (DNS). However, this approach is

substantially expensive when it comes to the simulation computational cost, even for simple geometries with relatively low-speed turbulent flows as it resolves eddies of all scales. Alternatively, Reynolds Averaged Navier Stokes RANS statistical modeling approach is used. RANS equations ignore the small-scale eddies through time averaging of the Navies-Stokes equations, where a variable in the equations is divided into a mean value and a fluctuating, time-varying component. This can be represented through the velocity component u_i as follows:

$$U_i = \bar{U}_\iota + \grave{u}_\iota \tag{49}$$

Where the averaged component $\bar{U}_\iota$ is calculated as follows:

$$\bar{U}_\iota = \frac{1}{\Delta t}\int_t^{\Delta t} U_i \, dt \tag{50}$$

Where Δt is the time scale that is small enough to resolve the changes in the mean value, but still larger than the time scale needed to resolve the eddies-generated fluctuations.
By substituting in continuity equation while assuming incompressible flow:

$$\nabla \cdot (\bar{U} + \grave{u}_\iota) = 0 \tag{51}$$

Hence, the turbulence kinetic energy can be represented as follows:

$$K = \frac{1}{2}\left(\overline{(\grave{u}_1)^2} + \overline{(\grave{u}_2)^2} + \overline{(\grave{u}_3)^2}\right) \tag{52}$$

Where only the velocity fluctuations are accounted for as they are originally generated through turbulence. Additionally, a Reynolds averaged momentum equation can be rewritten as follows:

$$\frac{\partial(\rho U_i)}{\partial t} + \frac{\partial(\rho U_i U_j)}{\partial x_j} = -\frac{\partial p}{\partial x_i} + \frac{\partial}{\partial x_j}(\tau_{ij-}\rho\overline{u_\iota u_j}) + S_M \tag{53}$$

While the Reynolds averaged energy equation is rewritten as follows:

$$\frac{\partial \rho H}{\partial t} - \frac{\partial p}{\partial t} + \frac{\partial}{\partial x_j}(\rho U_i H) = -\frac{\partial}{\partial x_i}\left(\lambda\frac{\partial T}{\partial x_j} - \rho\overline{u_j h}\right) + \frac{\partial}{\partial x_j}\left[U_i\left(\tau_{ij-}\rho\overline{u_\iota u_j}\right)\right] + S_E \tag{54}$$

By comparing at the two Reynolds averaged equations above, they show that the RANS approach did not change the original form of Navier-Stokes equations. However, turbulent (or Reynolds) stress term ($\rho\overline{u_i u_j}$) is added to include the change momentum flux due to turbulent fluctuations. Similarly, turbulent heat flux term ($\rho\overline{u_j h}$) is added to the diffusion term in the energy equation to reflect the change in the diffusion rate as a result of the introduction of additional convective transport due to turbulence fluctuations. Although these terms do not represent an actual stress or flux, it mathematically represents the approximate effect of turbulence on the flow behavior in the governing equations for modeling purposes.

The RANS approach is used by different turbulence models. These turbulence models introduce different formulas and approaches for the computation of unknown turbulence stresses and turbulence fluxes, and they can be classified into:

1. Eddy viscosity models
2. Reynolds stress models

Eddy viscosity models assume continuous generation and dissipation of small eddies which influence the turbulence stresses and flux. A proportional relationship between the turbulence stresses and the mean velocity gradient is assumed and new equations are introduced to solve for the unknown stresses and fluxes in RANS equations. On the other hand, Reynolds stress models solve additional transport equations for all the components of the Reynolds stress tensor making it more suitable for complex flows. However, studies showed it has comparable accuracy to other two-equation eddy viscosity models [67].

Two the widely used two-equations Eddy viscosity models are the k-epsilon (k-ε) and k-omega (k-ω). The two models introduce a set of equations that are complex enough to accurately model turbulent flow, compared to the one and zero-equation eddy viscosity models. The k-ω is widely argued to have superior accuracy for modeling adverse pressure driven low-Reynolds near wall flow. On the other hand, k-ε model is known for its robustness and high accuracy modeling of the free stream turbulence, however, it requires excessive near wall resolution of y^+<0.2 for low-Reynolds flows compared to k-ω model, where y^+<2 is found to be sufficient for most of the cases.

SST k-ω is a two-equation turbulence model presented by Menter [68] based on Baseline (BSL) k-ω model. however, it excels by properly modeling the turbulence shear stress

transport, hence avoiding the overprediction of the eddy viscosity prediction thanks to adding a limiter to the eddy-viscosity formula.

The advantage of the SST model stem from its ability to simultaneously use the k-ε and k- ω turbulence models within one domain making advantage of the superiority of each model at different flow regions over the other.

The SST k-ω turbulence model is used for all the simulations in this work. The turbulence model selection is based on previous studies. It was found that the results were nearly independent of the turbulence model (as shown in Fig. 3-2), especially at high speeds where the flow is fully turbulent in previous studies [59]. Additionally, Shear Stress Transport (SST) k-ω turbulence model provided a good agreement with the experimental results and lower computational time and cost. [42]

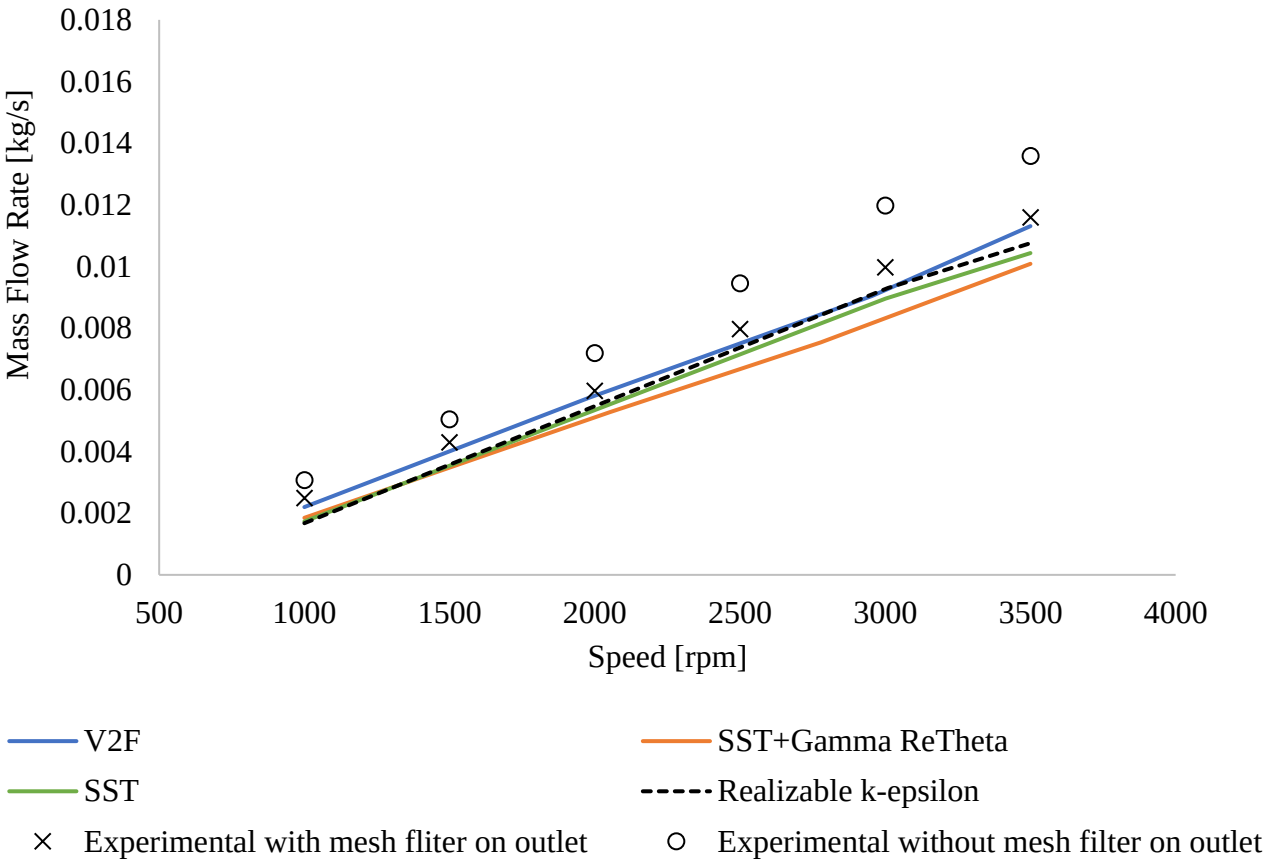

Fig. 3-2 Comparison of the different turbulence models and experimental data estimated rotor mass flow rate as presented by Fawzal et. al [59].

3.4 Rotational Modeling

Rotational modeling in CFD allows solving for the flow field over rotating assemblies. Unlike, conventional CFD models where the fluid is given a velocity component at a boundary to influence the fluid motion. One of the great advantages of the rotational models is their ability to solve for often unknown mass flow rate pumped through the system rotation, accordingly, a predefined velocity field or mass flow rate at the boundaries is not needed to drive the flow, unlike the non-rotational models.

Introducing a rotational component in the rotating frame adds the source of momentum to the momentum equation as mentioned earlier in section 3.2.1. Additionally, the velocity in the rotating frame of reference is calculated according to the equation below:

$$U_{rel} = U_{stn} - \omega \times R \tag{55}$$

where U_{stn} is the velocity of the flow in the stationary frame of reference, and R is the radius vector.

The new definition of the velocity in the rotating frame is introduced in the governing equations, and new forms of the equations are defined accordingly. One significant change is in the energy equations where rothalpy, I, replaces the total enthalpy term in the advection and transient terms. Rothalpy can be defined as follows:

$$I = h_{stat} + \frac{1}{2}\left(U_{rel} \cdot U_{rel} - (\omega \times R \cdot \omega \times R)\right) \tag{56}$$

One of the limitations in two-equation eddy viscosity models is their insensitivity to system rotational effects on turbulence. However, Spalart and Shur [69] introduced an empirical function to generate a multiplier, f_r, for the turbulence energy production term, P_k, expressed as follows:

$$P_k = \mu_t \, S^2 \tag{57}$$

where S is the strain rate magnitude expressed through this term:

$$S = \sqrt{2 \, S_{ij} \, S_{ij}} \tag{58}$$

and S_{ij} is the strain rate tensor

$$S_{ij} = \frac{1}{2}\left(\frac{\partial U_i}{\partial x_j} + \frac{\partial U_j}{\partial x_i}\right) \tag{59}$$

The production multiplier, f_r, is expressed in ANSYS CFX through this equation:

$$f_{rotation} = \frac{4\,r^*}{1+r^*}[1 - tan^{-1}(2\tilde{r})] - 1 \tag{60}$$

where r^*, and $\tilde{r}$ are calculated through the strain rate tensor, S_{ij}, and the vorticity tensor, Ω_{ij}, that accounts for the flow rotation in the stress tensor in the momentum equation.

These modifications to the eddy viscosity turbulence model -often referred to as curvature correction- is automatically applied to the SST model in ANSYS CFX allowing it to model rotational flows in rotating systems at sufficient accuracy levels as shown in the results from Fawzal et. al [58] study in the figure above. In this work, default settings for the scaling coefficients for the curvature correction are used.

The two rotational modeling approaches used in this research will be discussed in the next section.

3.4.1 Single Rotating Reference Frame (SRF) modeling

This approach models the fluid domain as a single zone. Rotational modeling equations presented in the previous section are solved for all the elements in the fluid domain. Rotating walls can be modeled with the fluid zone and their effects on the flow field are accurately captured. Stationary walls, however, are limited to the boundaries that are modeled as surfaces of revolution. Hence, the simulations where such an approach is applicable are limited to the simulation of rotor assemblies with simple or no shrouds/volutes.

Despite the SRF approach limitations, it can be of great advantage for fast and robust steady state solutions of rotational flows. SRF models are used in this work for the initial assessment of different rotor configurations and fan blade geometries. Although these initial simulations do not reflect the effect of the full machine assembly on the cooling air flow, they helped set the base geometry of the rotor structure. Such a process can be time-consuming using other computationally expensive approaches.

The SRF models in this work used a revised version of the fluid domain geometry presented in [41]. Instead of having the fluid domain split at the air gap to have a stationary and a rotating domain with two frames of reference, the air is modeled as a single domain with the stator/cover walls given a counterrotating velocity component to mimic their stationary nature in the rotating frame of reference.

3.4.2 Multiple Frames of Reference (MFR) modeling

The MFR approach models the fluid domain as split cell zones, each cell zone is then related to a frame of reference so that a relative motion between the two frames is allowed. For rotor-stator applications, one frame is set to rotate relative to the other. This allows having the cell zones near the stator components related to the stationary frame of reference, On the other hand, the cell zones surrounding the rotor are assigned to the rotating frame of reference.

The advantage of this approach is that it allows for modeling the more complex structures of the full machine assembly rather than just modeling the rotor. This comes at a cost of increased size and complexities in the computational domain geometry.

Two sub-models were used in this work for modeling the thermal performance of the rotor assembly, the two models are:

3.4.2.1 Frozen Rotor (FR) models

Frozen rotor models capture an instantaneous solution of the fluid flow; The instant captured is defined by the position of the moving mesh relative to the stationary mesh.

The solution captured by this model is considered a steady state solution whenever the transient effects due to flow unsteadiness are nonexistent or can be neglected.

FR models are found to accurately capture the flow properties at the steady state, however, they failed to capture the necessary surface-level transient effects required to accurately model the heat transfer in CHT model. since the rotor position is frozen by definition in this model., hence, the rotational effect of the solids with respect to the fluid is not considered. The circumferentially uneven instantaneous local heat transfer on the rotor surface then results in circumferentially uneven temperature distribution and local hot spots are formed as shown Fig. 3-3. This solution is judged unrealistic given the significantly larger solid timescale of the rotor compared to the fluid flow timescale as shown in Table 3. Where, L, is the characteristic length, and α, is the thermal diffusivity.

Domain	Fluid domain	Solid domain
Timescale Equation	$\frac{1}{\omega}$	$\frac{L^2}{\alpha}$
Min. Timescale	$1.469e-3\ [s]$	$7.572\ [s]$

General simulation timestep	Time per one degree of rotation $= \frac{60\ [s]}{6500\ [rpm] \times 360[deg]} = 2.564e-5\ [s]$

Table 3 Calculation of the different simulation timescales.

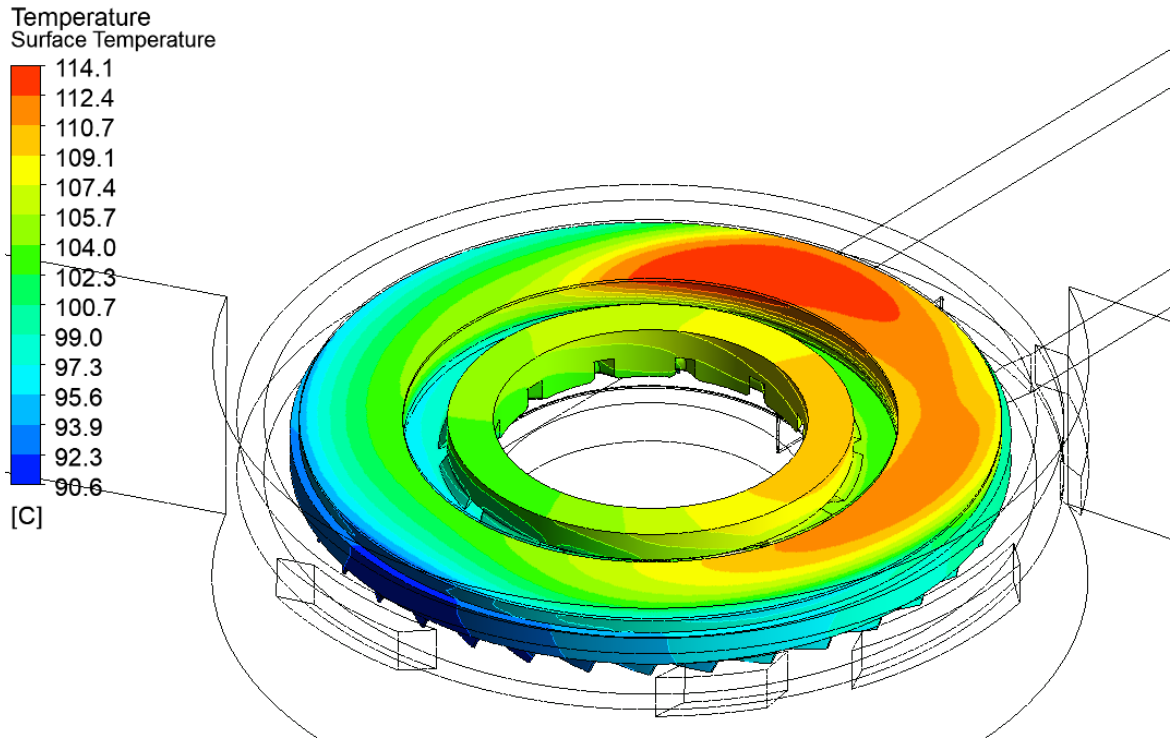

Fig. 3-3 uneven spatial temperature distribution in the solid domain in CHT simulation as a result of computational domains timescales inconsistency.

3.4.2.2 Transient Rotor Stator (TRS) models

Transient rotor-stator models use a different modeling approach than the FR models, where the two domains are allowed to rotate relative to each other and the solution is captured at every time step. This approach is used to capture the unsteadiness in the flow over the rotor and its effect on the heat transfer. Furthermore, the TRS model allows to solve at different timescales, this allows tackling the error due to the different timescales of the fluid and solid domains seen earlier with the FR model. It is worth mentioning that the steady state solution acquired using both TRS and FR models is found to be nearly equal which indicates minimal unsteadiness in the flow field.

The approach followed to control the solution timescale issue is composed of three steps:

1. Running a simulation using TRS using a small timestep - 1 degree of rotation – relevant to the fluid domain timescale to obtain fluid flow solution convergence. It is worth mentioning that using this timestep to obtain a converged solution for the solid domain would require an unreasonable number of iterations. The experimental results discussed by Hey et. al [62] for a transient study of the rotor thermal behavior showed that the time constant for the rotor to reach thermal equilibrium was approximately 90 seconds. This means that more than 3.5 million iterations are needed to reach thermal equilibrium, assuming using the same rotor geometry and materials. Hence, a timescale manipulation is used as will be discussed in the next step.
2. A second simulation is run using a much bigger timestep, relevant to the solid timescale while using the previous simulation results as initial conditions. The updated timestep is chosen so that the rotor rotates 8 full revolutions plus 5 degrees of rotation each time step. This approach mimics a 5-degree rotation of the rotor every timestep, which allows faster convergence of the solution in the solid domain while retaining reasonable stability of the fluid flow solution ensuring that it does not diverge. A converged solution of the temperature distribution in the solid domain is reached within a reasonable number of timesteps (<2000 iterations). Nevertheless, the excessively large timestep compromised the fluid flow solution accuracy, and oscillations in the flow properties and solution residuals are noticed.
3. Finally, a third simulation is run using the second simulation results as initial conditions, while using the initial small timestep once again. This reverses the unsteadiness in the fluid flow domain solution caused by using an excessively large timestep in the second step without changing the solid domain solution. The results from this simulation are then considered a fully converged solution.

It is worth noting that this approach is not followed for the steady state SRF simulations, since an axisymmetric rotor casing geometry with circumferentially uniform inlet and outlet is assumed. The axisymmetric geometry does not result in a considerable circumferential variation in the fluid flow and the associated surface thermal properties, hence circumferentially uniform heat transfer and temperature distribution are inherently maintained.

3.5 Boundary Conditions

The boundary conditions for the different walls and interfaces are set in the software as shown in Fig. 3-1 and Table 4, where p_{total} is the total pressure, p_{static} is the static pressure and T is the static temperature. A constant stator temperature of 150 °C is prescribed for the isothermal boundary condition at the air gap as a conservative approach to account for the unknown heat flux from the stator. This boundary condition is commonly used in different studies and found to be a good approximation since the stator heat transfer is not the main concern of this study [6] [7] [10]. Adiabatic conditions are specified for surfaces where insignificant heat flux is expected, such as the rotor innermost surface and surfaces of the stator carrier away from the stator cores and coils where most of the electromagnetic losses are concentrated. A conservative heat flux value of bearing mechanical losses is applied at an approximated rotor-bearing interface surface at the rotor inner diameter. An insulative adhesive layer of 0.1 W/m-K thermal conductivity is considered as thermal contact resistance between the solid components.

A stagnation boundary condition is specified at the inlet, whereas an atmospheric opening is specified for the outlet to minimize the influence of outlet boundary conditions on the results. Moreover, the inlet and outlet fluid regions were extended to a suitable extent through multiple iterations for the same purpose. These boundary conditions allow the model to solve for unknown mass flow rate due to the rotor rotation. Symmetry conditions are considered to account for the double-rotor, single stator motor topology.

Boundary	Condition
Inlet	p_{total} = 0 Pa, T = 298 K
Outlet	Atmospheric opening at p_{static} = 0 Pa
Stator / Cover Walls	Adiabatic no-slip smooth wall
Stator Wall Facing Air Gap	Isothermal no-slip smooth wall T = 423 K
Rotor Fluid Solid Interface	Conservative heat flux, no-slip smooth wall
Solids Interface	0.05 mm adhesive layer

Table 4 Boundary Conditions

3.6 Mesh

Hexagonal or hybrid conformal meshes are generated using ANSYS meshing software for the modeled geometries accounting for periodicity to reduce mesh size whenever applicable. The mesh is refined in the near wall fluid regions to keep y^+ near unity for accurate boundary layer resolution.

3.6.1 Mesh sensitivity analysis

A mesh sensitivity analysis study is performed to ensure high solution accuracy and minimal discretization error. The study is performed on one a simple 6° periodic sector model using the SRF approach. Four meshes are tested with different mesh counts as shown in Table 5. Four solution monitors are used to measure the accuracy of the solution and determine the mesh independent solution, with the main focus being on the variation in magnets temperature as

the main design parameter in this work.

Mesh	Elements Count, n	1/n	Mass flow [kg/s]	$\overline{Nu}_{Rotor}$	$\overline{Nu}_{Stator}$	T_{Magnet} [K]	Error %
Mesh 1	86277	1.2E-05	0.01024	316.0	134.8	397.0	0.5
Mesh 2	308598	3.2E-06	0.01047	336.5	136.8	397.9	0.27
Mesh 3	1707750	5.9E-07	0.01071	352.0	126.2	399.1	0.025
Mesh 4	1855680	5.4E-07	0.01071	352.2	124.3	399.1	0.025
Mesh Independent	-	0	0.01078	356.0	127.4	399.0	0

Table 5 Mesh sensitivity analysis

The study shows that despite the noticeable variation in other solution parameters, the final effect on the magnets temperature is found to be marginal. The error from the mesh independent solution is found to be only 0.5% with the coarsest mesh and 0.025% with the two finest meshes. This concludes the insensitivity of the solid thermal characteristics to mesh size in CHT rotor simulations. In mesh sensitivity studies done by Malloy[70], Fawzal [44], and Howey[49], they showed similar results where mesh refinement had a minimal effect on the temperatures and thermal properties in rotor simulations. One potential reason for such small errors is that a relatively fine mesh near the rotor walls is maintained across all studied meshes. This ensures having a solution of relatively high accuracy for the surface properties regardless of the overall mesh size.

Fawzal [44] divided the computational domain into different parts where each part had a different mesh setup. The mesh density and near wall grid thickness were varied iteratively to achieve low $y^+$and independence of thermal and flow characteristics. Given the similarity between the geometry of the computational domain in the referenced study and this work; the same approach is followed, and the same target mesh criteria are used. The mesh elements size target is kept within 0.75-1 mm within the rotor enclosure. Additional mesh refinement near the rotor walls and blades is maintained by setting the first mesh layer thickness between 0.5 - 0.05 mm throughout the rotor to account for the local high Reynolds number over different surfaces. Greater attention to the mesh refinement at the air gap is required given the sensitivity of the heat transfer to the flow regimes in this region as shown in Fig. 3-5. Hence, a hexahedral grid with 32-40 elements across its thickness is used to ensure mesh independence at this region according to earlier studies[49] [71]. Fig. 3-4 shows an example of the meshes used in this research and the resulting non-dimensional wall distance, y^+, shown in Fig. 3-6.

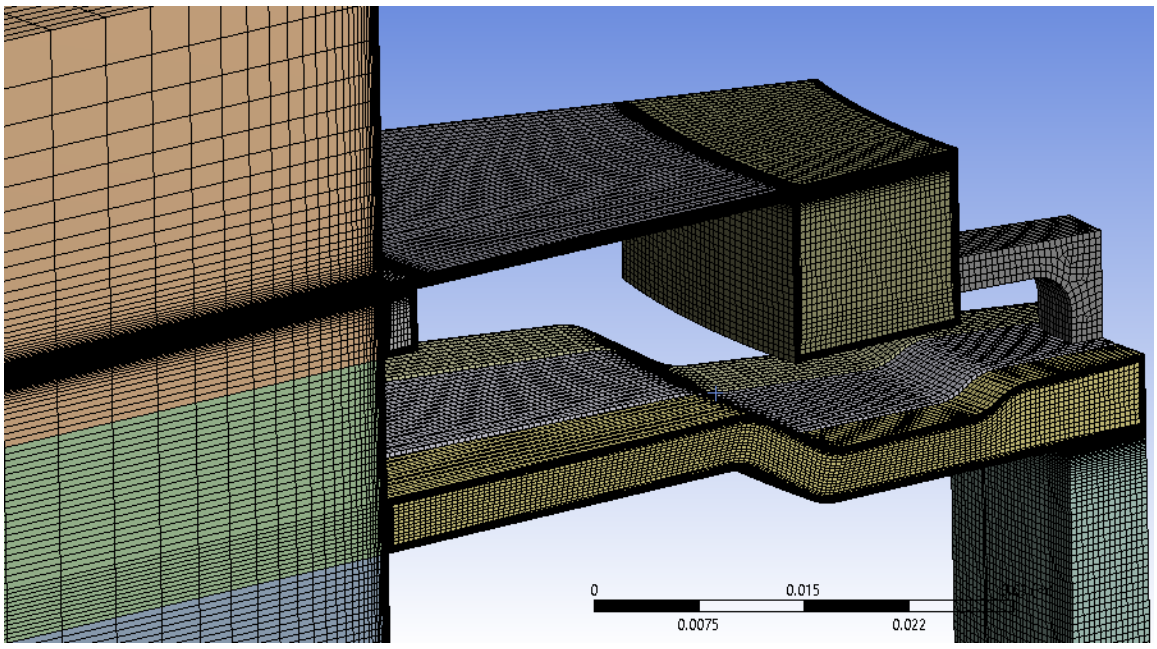

Fig. 3-4 Hexahedral mesh used for straight blade sectional simulation

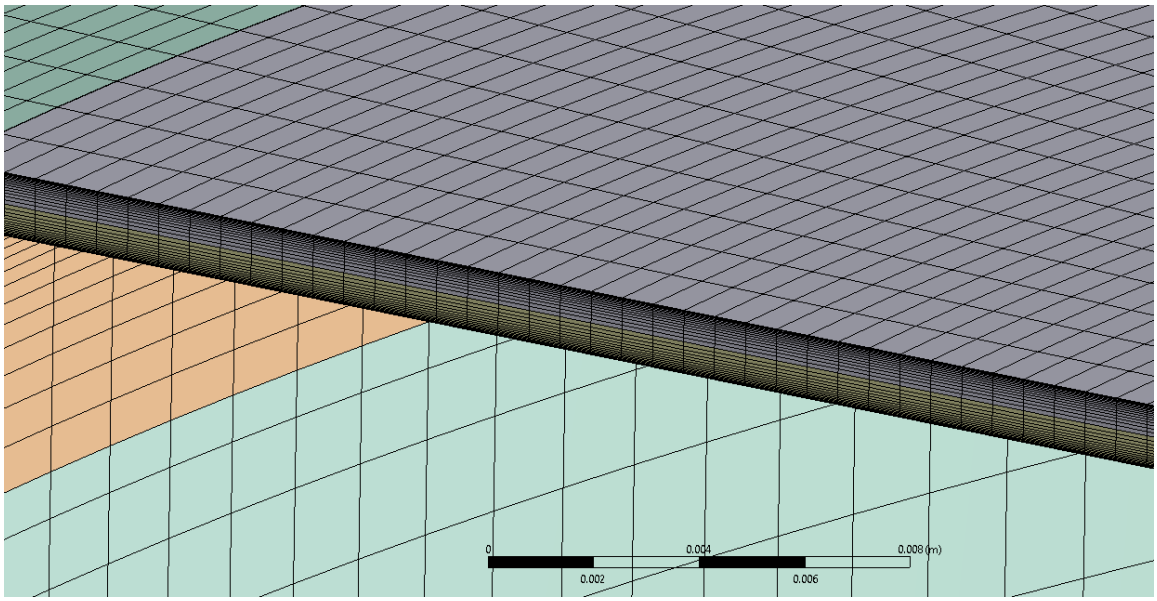

Fig. 3-5 Close up at the hexahedral mesh layers at the air gap

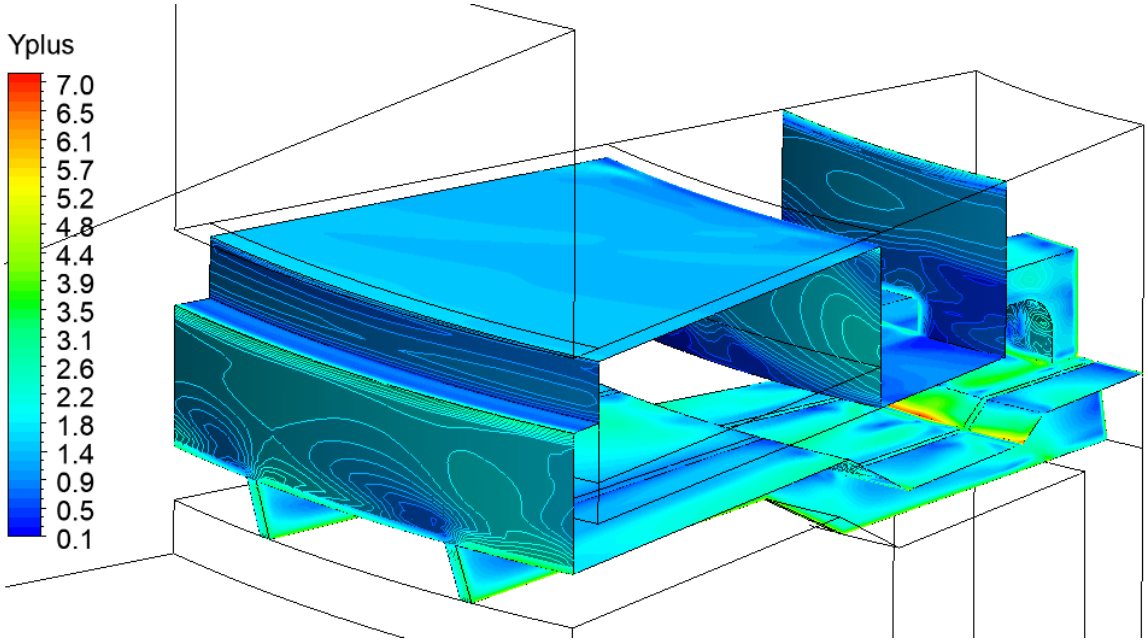

Fig. 3-6 Non dimensional wall distance y^+ at the rotor surfaces.

3.7 Convergence Criteria

Solution convergence is judged through monitoring different variables in the solid and fluid domains, such as magnets maximum temperature, total heat flow, and inlet mass flow rate. Besides, an RMS residuals value of 10^{-5} is set as a convergence criterion, and a Coefficient of Variation (COV) value of 0.01 was set as a target for the heat flux. The COV is the normalized standard deviation of the moving average $\overline{\emptyset}$. In other words, the COV measures the deviation of the total heat transfer from the mean. When COV is equal to 0.01, it means that the total heat transfer is converged within 1% variation about its mean. The moving average interval is set to 25 iterations. Normally the thermal variables converge at a lower number of iterations before reaching the other convergence criteria, which indicates the sufficiency of these criteria to reach a converged solution.

$$\overline{\emptyset} = \frac{1}{N}\sum_{j=1}^{N} \emptyset(j) \tag{61}$$

$$\sigma = \sqrt{\frac{1}{N}\sum_{j=1}^{N} \left(\emptyset(j) - \overline{\emptyset}\right)^2} \tag{62}$$

$$COV = \frac{\sigma}{\overline{\emptyset}} \tag{63}$$

3.8 Verification

The discussed CFD model setup is verified against the results discussed in [41]. Similar geometrical setup is used; however, the dimension of the designed machine is used.

The correlations provided in the study is used to calculate the heat transfer over the magnets air gap surface as a highly critical heat transfer region. The Nusselt number value calculated from the simulation is compared to the correlated values within a 1.1% margin of error. The figures below (Fig. 3-7, and Fig. 3-8) show the flow patterns in the verification simulation. The shown patterns are found to be similar to the patterns shown in Rasekh's study.

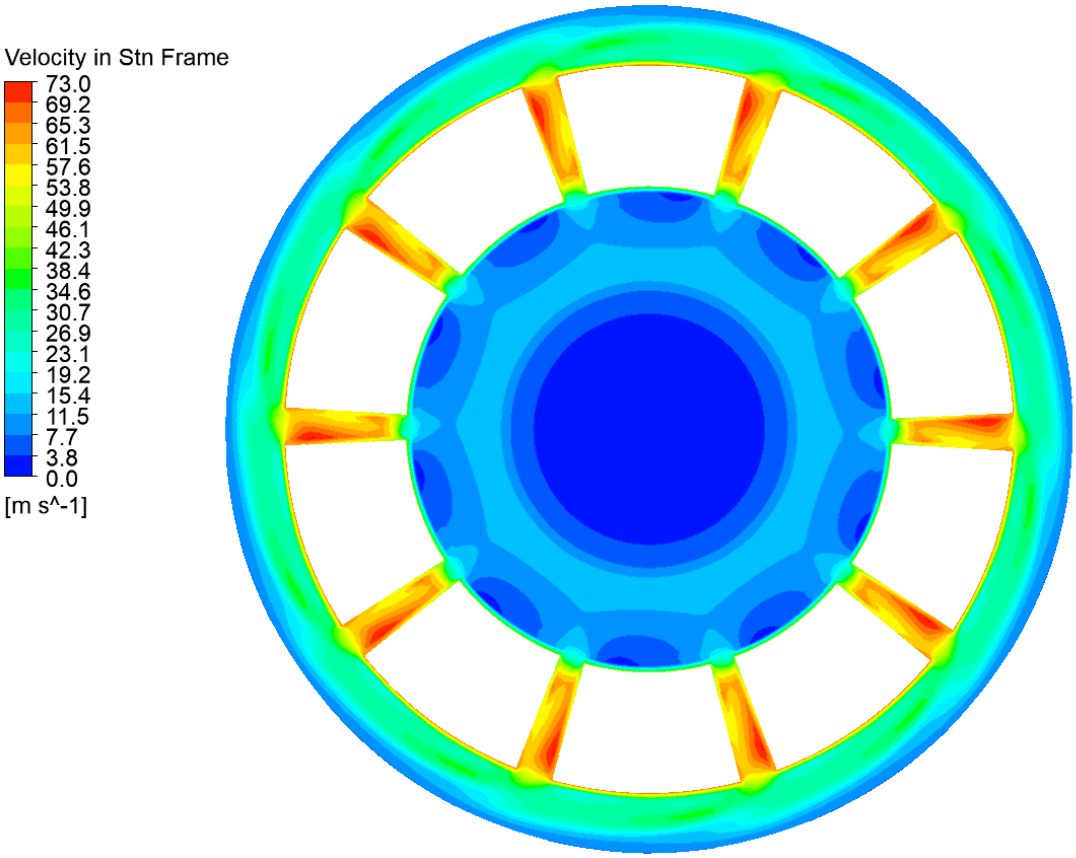

Fig. 3-7 Velocity contours captured at an axial plane located at the middle of the magnets thickness showing similar flow patterns at the equivalent location shown in [41].

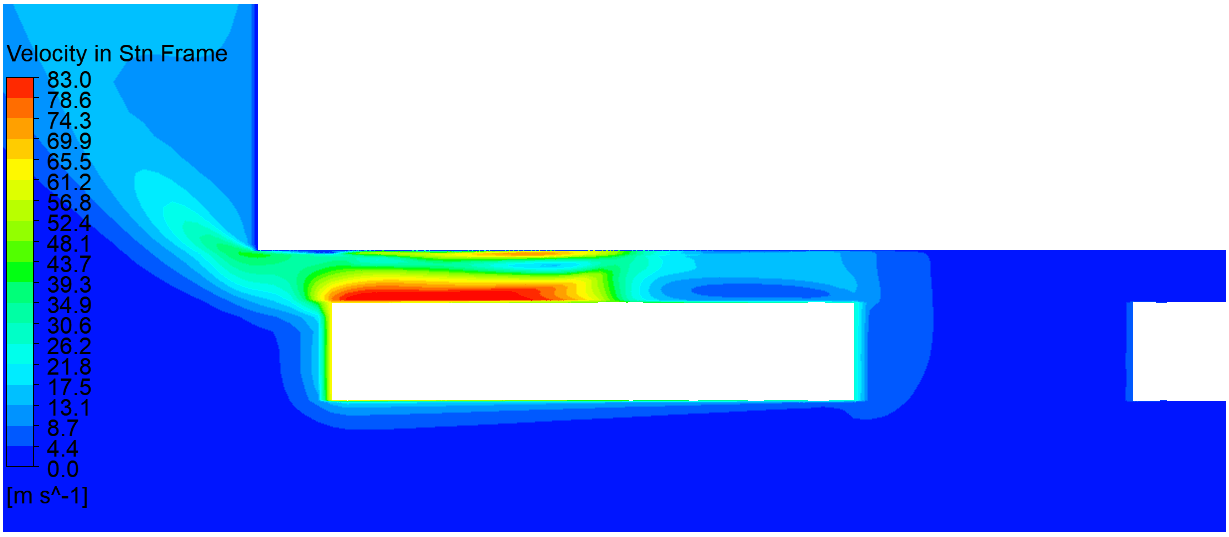

Fig. 3-8 Velocity contours around the rotor at a radial plane located in the middle of the magnets air-channels showing similar flow patterns at the equivalent location shown in [41].

Chapter 4

Integrated Rotor Air Cooling Improvement and Design Iterations

4 Integrated Rotor Air Cooling Improvement and Design Iterations

The simplest rotor design for an AFPM machine has blunt rotor carrier geometry 0with flat surfaces and surface-mounted magnets. The rotor losses as previously discussed makes the magnets at the risk of potential overheating and demagnetization. An air cooled rotor with flat surfaces at low rotational speed would have an inherently limited cooling capacity and may not provide a sufficient cooling rate to keep the magnets below their thermal threshold. The designed machine generates heat in the rotor that can reach as high as 740 W, thus a rotor air cooling rate of the same value should be maintained while keeping the magnets temperature below 100 C as previously specified in the machine operation requirements.

Multiple designs of the rotor and the rotor housing are tested numerically through different design iterations. These designs aim to improve the rotor thermal performance by introducing and improving the design of multiple geometrical features on the machine rotor and its housing that can enhance the rotor heat transfer. However, such geometrical features might also increase the machine windage losses, therefore multiple design iterations have to be carried out in order to ensure the best possible thermal performance of these designs at a low cost of associated windage losses

4.1 Design Direction Setting

Initial design iterations are made in order to set the initial base rotor geometry design. The design features are applied progressively to a basic design that considers the structural requirements of the rotor assembly shown in Fig. 4-1.

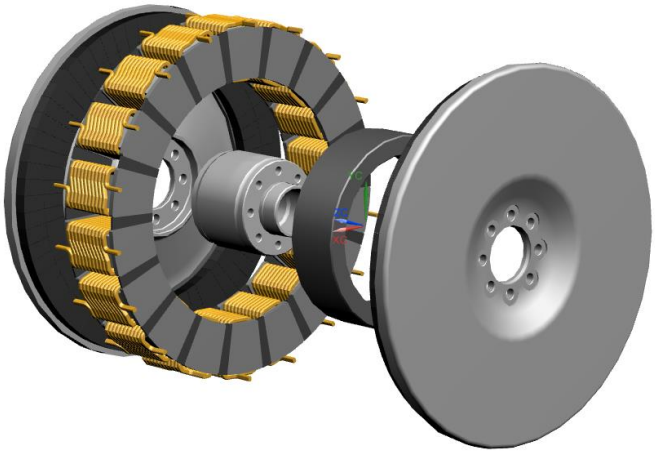

Fig. 4-1 Base machine assembly with preliminary basic rotor design.

The rotor housing design, although critical to the rotor thermal performance, is initially set as a simple wall with a simple inlet and outlet to ease the simulation process during the first phase of the rotor design. Six rotor designs are selected for this study and classified as shown below:

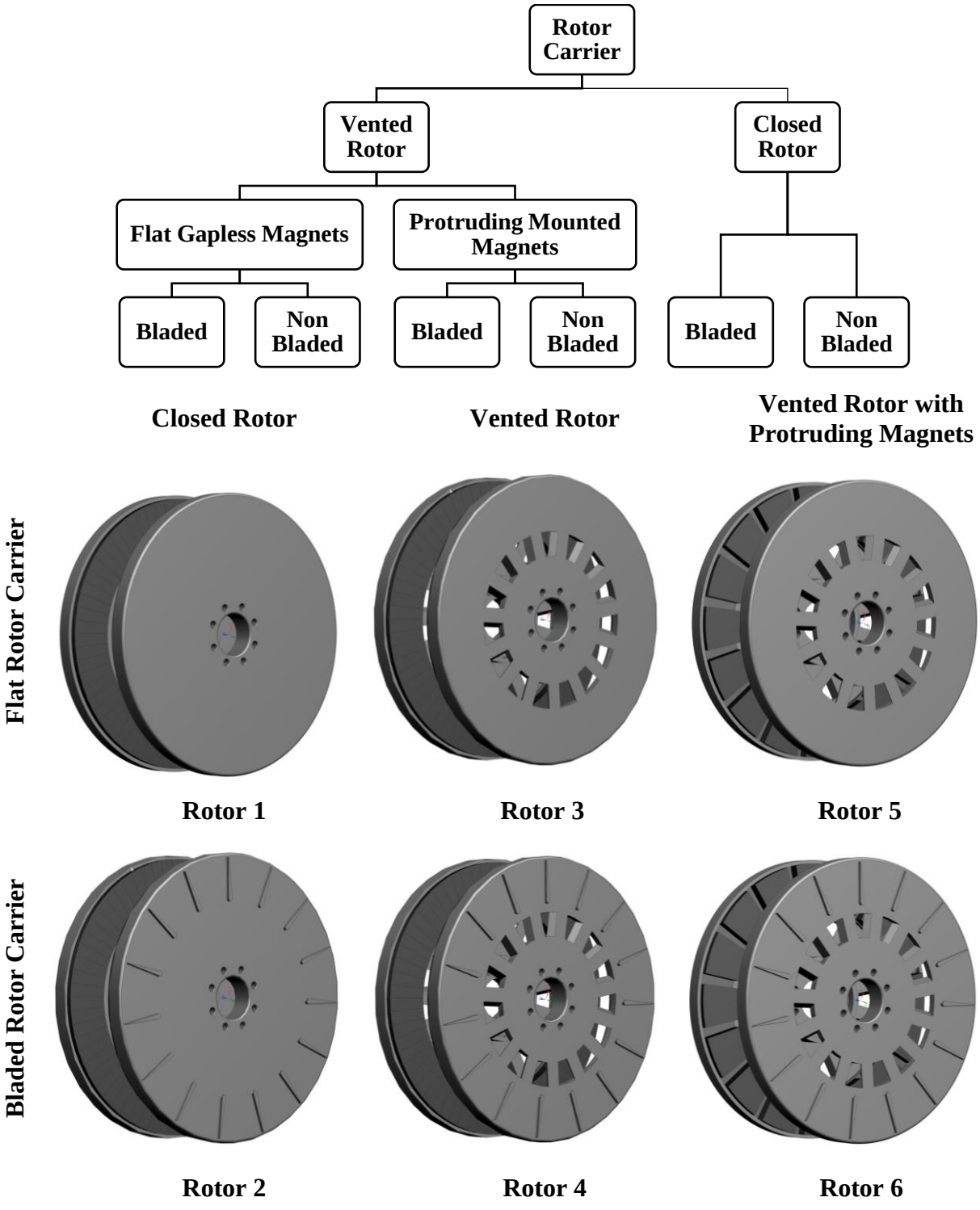

All six rotor assemblies are simulated with a simple wall enclosing the rotor carrier. The wall represents the motor housing with an axial air inlet at the center of the rotor and an open periphery as an outlet. This inlet arrangement is selected based on the study done by Fawzal et al [60]. However, a completely open periphery is used as an outlet instead of the volute casing with a single outlet used in the study. The volute casing outlet might be a must for a commercial machine design due to outlet size limitations imposed by the motor assembly. However, this design iteration is meant to investigate the simplest rotor/housing assembly. Moreover, this simplification facilitates the study of the different designs using a sectional rotational CFD model. The studied fluid and solid domains are modeled in ANSYS SpaceClaim following the geometrical guidelines for sectional models discussed in Chapter 3. The results from different CFD simulations show incremental improvement in the rotor cooling performance through adding the previously discussed geometrical features, as shown in Fig. 4-2. The average heat transfer coefficient values discussed are calculated based on the inlet temperature.

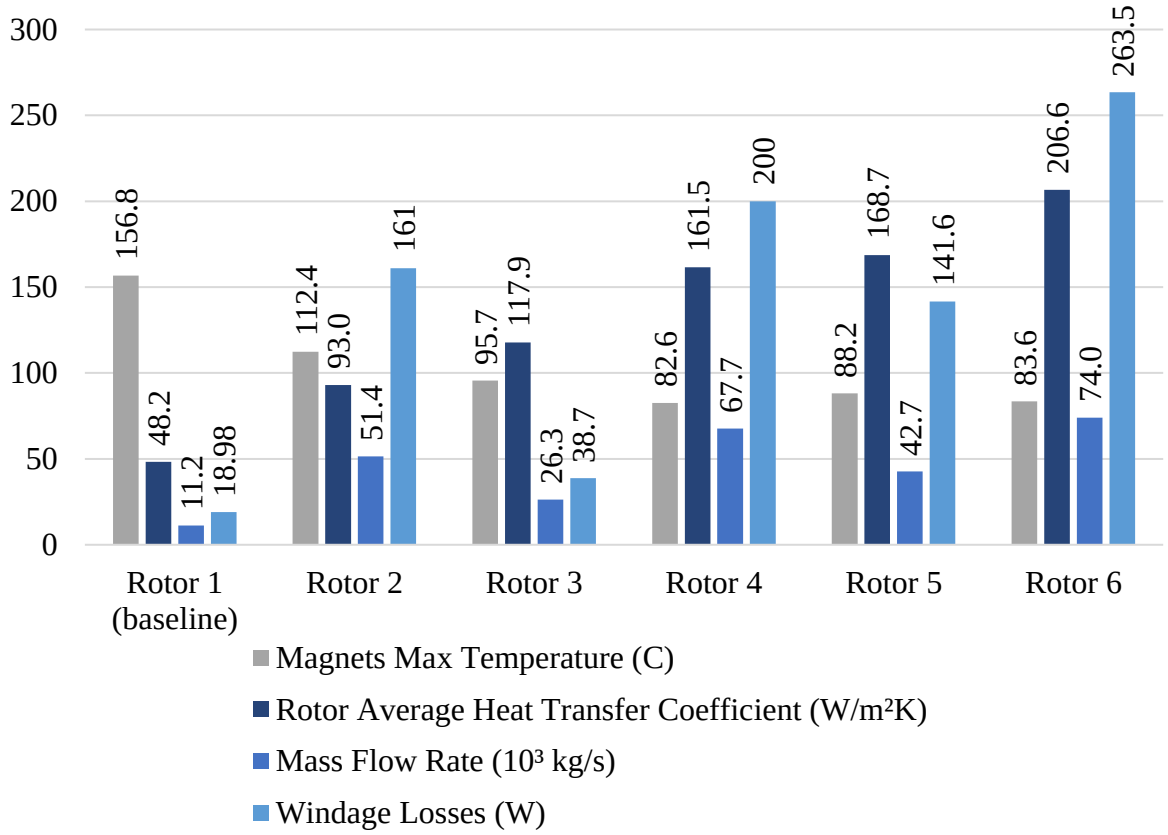

Fig. 4-2 Performance monitor variables of the different rotor designs.

The enhancement in rotor cooling is best demonstrated in reducing the maximum magnets temperature at the same operating conditions. The temperature reduction is directly related to either an increase in the mass flow rate, the rotor average heat transfer coefficient or both. The rotor geometry dictates the amount of momentum transferred from the rotor to air which defines the pumping power of the rotor hence the mass flow rate. The flow turbulence is mostly dictated by rotor surface geometry features. It defines the surface conductance and, hence, the heat transfer coefficient. There is also a direct relationship between mass flow rate and windage losses representing the pumping power. This was observed in the rotors, which either have an embedded fan or surface-mounted magnets that have a centrifugal fan-like effect centrifugal fan.

4.1.1 Closed Rotors (Rotor 1 and 2)

Rotor 1 shows the highest magnet temperature associated with the lowest mass flow rate and lowest rotor average heat transfer coefficient. Batchelor flow pattern at the air gap is observed which explains the deteriorated heat transfer [38]. Hot air is recirculated at the air gap due to the existence of the rotating core between the rotor and stator boundary layers. The flow streamlines over Rotor 1 presented in Fig. 4-3 show Batchelor flow type, also Eckman layer flow at the enclosed cavity between the rotor and the stator agreeing with [30]. These two flow regimes deteriorate the cooling heat transfer or even heat the rotor inner surfaces where the entrapped recirculating air temperature exceeds the solid body temperature of the magnets. The low mass flow rate is due to the limited pumping effect of the flat rotor surface compared to the other designs with blades and through-flow ventilation. This design represents the baseline performance allowing for assessment of enhancements in the other geometries.

Rotor 2 with the embedded fan blades decreased the magnets maximum temperature by 44 degrees due to the increased mass flow rate and turbulence over the rotor carrier surface, as shown in Fig. 4-4. This improvement, however, comes at the cost of a 140 W increase in the windage losses equivalent to the added pumping power of the fan.

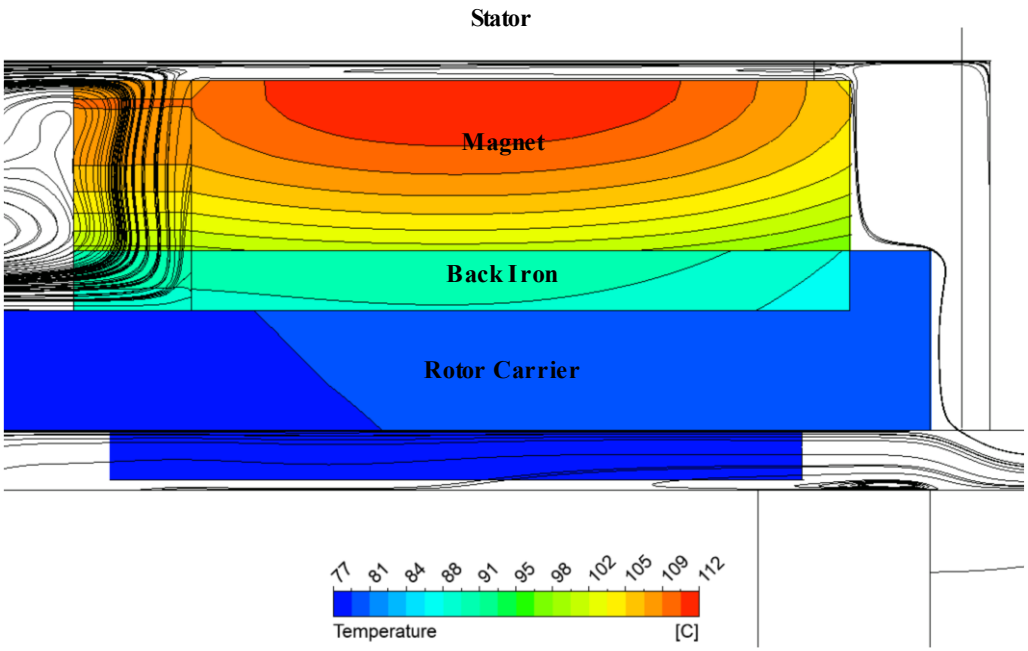

Fig. 4-3 Flow streamlines over the magnets at the rotor periphery showing Batchelor flow with core rotation at the air gap and Eckman layers at the rotor cavity in Rotor 2.

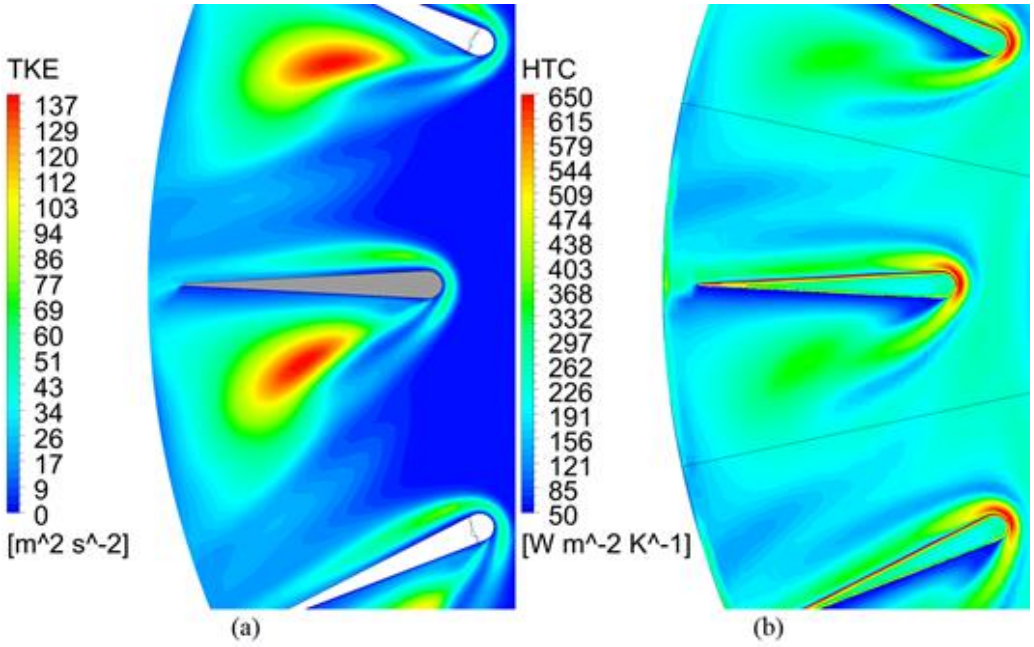

Fig. 4-4 Correspondence of high turbulence kinetic energy of air at 0.5 mm from the rotor surface (a) in Rotor 2 with high local heat transfer coefficient over the rotor surface (b).

Both Rotor 1 and 2 have similar flow patterns over the rotor's inner surfaces. Accordingly, most of the heat is removed indirectly through the rotor carrier surfaces similar to the baseline geometry. The temperature contours in Fig. 4-3 show a nearly one-dimensional heat flow in the axial direction with the hottest spot on the magnet surface at the air gap. This can be observed through the nearly flat temperature contours as a result of minimal heat transfer on the magnets surfaces, while a noticeable temperature gradient is seen in the axial direction with lower temperatures shifted towards the rotor carrier showing the direction of the nearly one-dimensional heat flow. The half parabolic temperature contour in the back iron supports the same rationale since a secondary heat flux in the radial direction is introduced by the rotor carrier lip where it contacts the back iron at the outer diameter. The contour curve is nearly flat at the back iron inner diameter indicating a diminished heat transfer on the inner surface. The reason behind the diminished cooling rate on the external surfaces of either the magnets or the back iron is due to flow recirculation at the air gap and the enclosed.

4.1.2 Vented Rotors (Rotor 3 and 4)

Rotor 3, although flat, showed major improvement in the cooling performance achieving lower magnets temperature and higher average rotor heat transfer coefficient at a lower mass flow rate when compared to its non-vented counterpart Rotor 1. Unlike the non-vented rotors, the temperature contours in vented rotors tend to be more elliptical contours with their center shifted towards the outer diameter which indicates the heat is being transferred through all surfaces. The existence of vents in the rotor allowed a net outward flow at the air gap periphery eliminating the recirculating core as the flow changes to Stewartson flow type as shown in Fig. 4-5. The net outward flow results in having the higher temperatures contours shifted towards the peripheral walls due to the higher heat transfer rate at the inner walls since they are exposed to colder air from the vents. The Stewartson flow type allows the magnets and back iron to be cooled at all the surfaces, unlike the closed rotors where the losses were mostly cooled through conducting heat to the rotor carrier. Also, lower magnets temperatures are achieved at 75 % less windage losses.

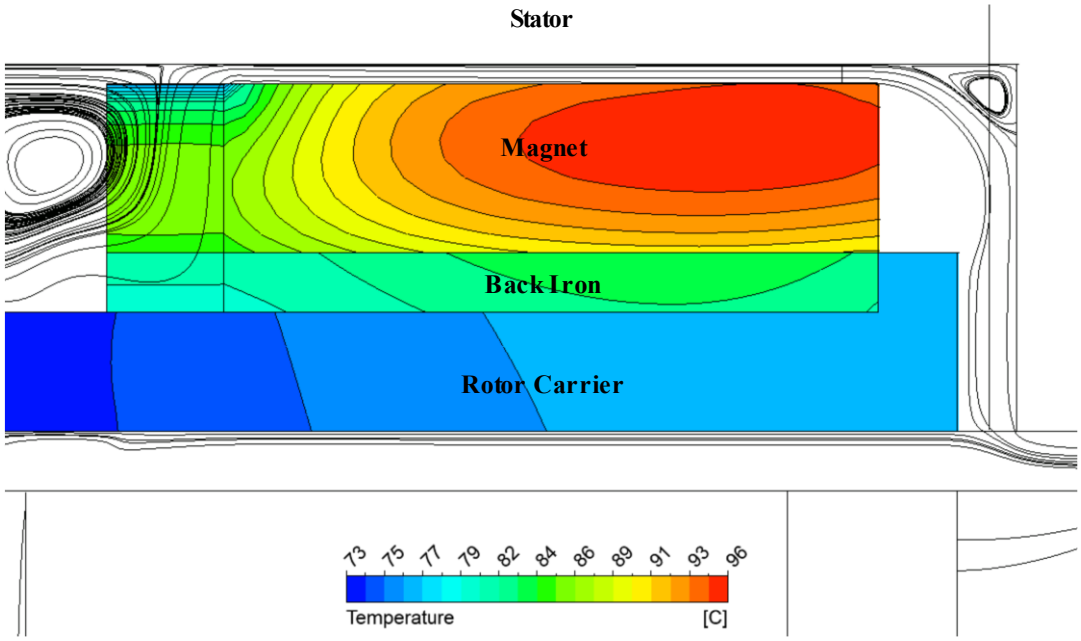

Fig. 4-5 Flow streamlines over the magnets at the rotor periphery showing Stewartson flow with net outward flow in Rotor 3.

The combination of rotor blades with the vents in Rotor 4 shows further reduction in the magnet and overall rotor temperatures. This reduction is a result of the increased mass flow rate as well as increased heat transfer due to the higher turbulence at the bladed side of the rotor, similar to Rotor 2 . However, the windage losses increase by 160 W compared to the bladeless Rotor 3.

4.1.3 Rotors with protruding magnets

Introducing air channels between magnets poles in Rotor 5 improves the cooling performance compared to Rotor 3 which has the same rotor geometry minus the air channels. The magnets maximum temperature drops 7 degrees, while the average temperature drops 15 degrees. However, the windage losses increase by 103 W due to the added fan effect from the protruding magnets. This effect results in a 62 % increase in the air mass flow rate and a 43 % increase in the average heat transfer coefficient. The increased magnets surface area and air mass flow rate as well as the added flow turbulence contributed to the overall enhancement in the cooling performance.

Rotors 5 and 6 show unsymmetrical temperature distribution in the magnets with an observable hot spot on the pressure side. This is related to the non-uniform airflow inside the air channels, which causes a difference in turbulence kinetic energy levels over the channel sides, as shown in Fig. 4-7.

This affects the local heat transfer on the magnets pressure and suction sides, as shown in Fig. 4-7. On the suction side, the graph shows a local peak halfway through the air channel corresponding to an increased local turbulence kinetic energy of the flow near the wall at that location. Contrarily, on the pressure side, the local heat transfer is high along with the first 20 % of the channel length, followed by a dip that corresponds to the location of the hot spot observed on that magnet face. The heat transfer increases again at the channel end as the air flows over the sharp edge of the magnet.

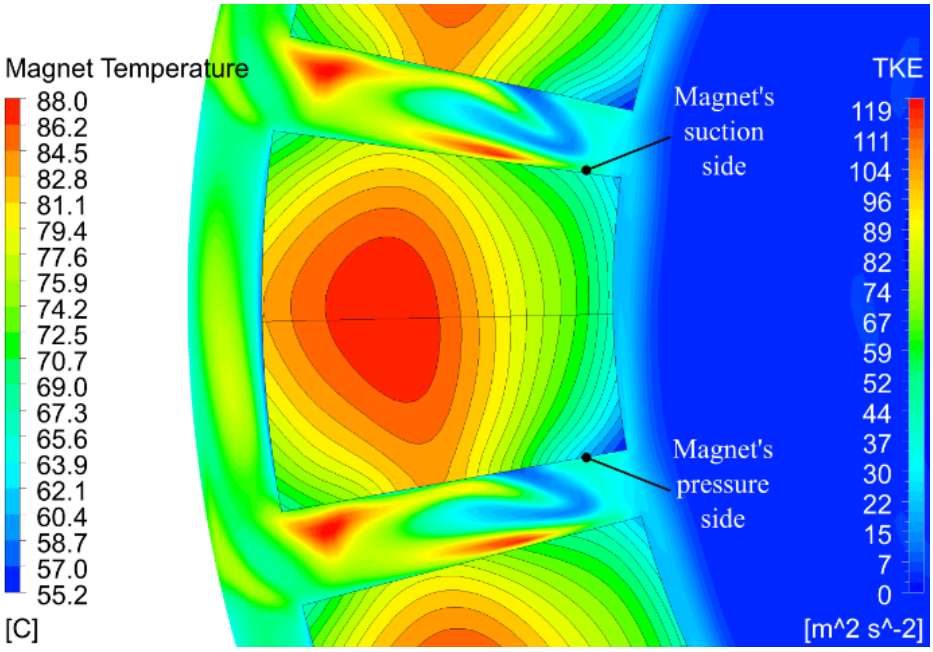

Fig. 4-6 Turbulence kinetic energy in the air channels and the corresponding temperature contours inside the magnets poles in Rotor 5.

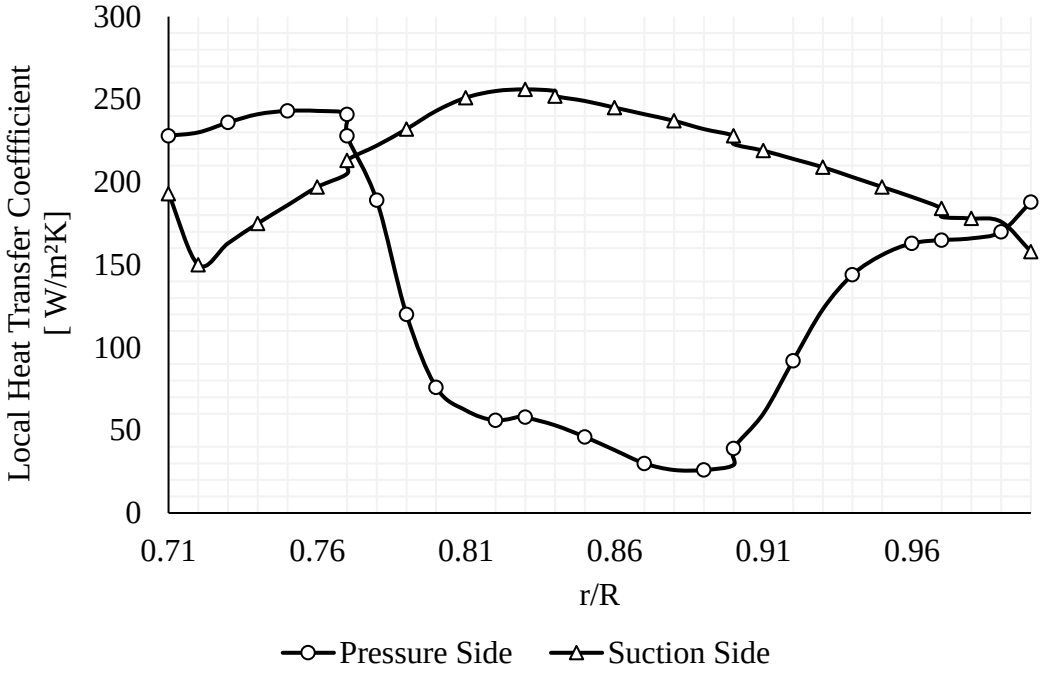

Fig. 4-7 Local heat transfer on the magnets suction and pressure sides.

Rotor 6 has the best thermal performance among all other rotors having the highest average rotor heat transfer coefficient. However, it has 1 degree higher maximum magnets temperature than Rotor 4 and 32 % higher windage losses. The temperature contours in Fig. 4-8 show better temperature distribution in Rotor 6 compared to Rotor 4 implying a lower average temperature of the former due to the increased heat transfer on the air channel sides of the magnet. This can be related to the fact that the fluid flow exhibit core rotation at the air gap in Rotor 6 as most of the rotor outflow exit through the air-channel rather than the air gap which result in increased film temperature at the magnets surface at the air gap [42] [43], hence the deteriorated heat transfer. The conclusion is that the protrusion of the magnets allows for increased mass flow rate around the rotor as well higher average Nusselt number over the rotor surfaces. The increased overall heat transfer only reduced the average temperature of the magnets by 5 degrees, while, the maximum temperature slightly increased due to the deteriorated heat transfer at the air gap. The improvement in thermal performance came at a cost of increased windage losses, such an increase represents an unjustifiable addition to the machine losses given that the enhancement in cooling performance is not enough to further lower maximum magnets temperature which is the main design goal.

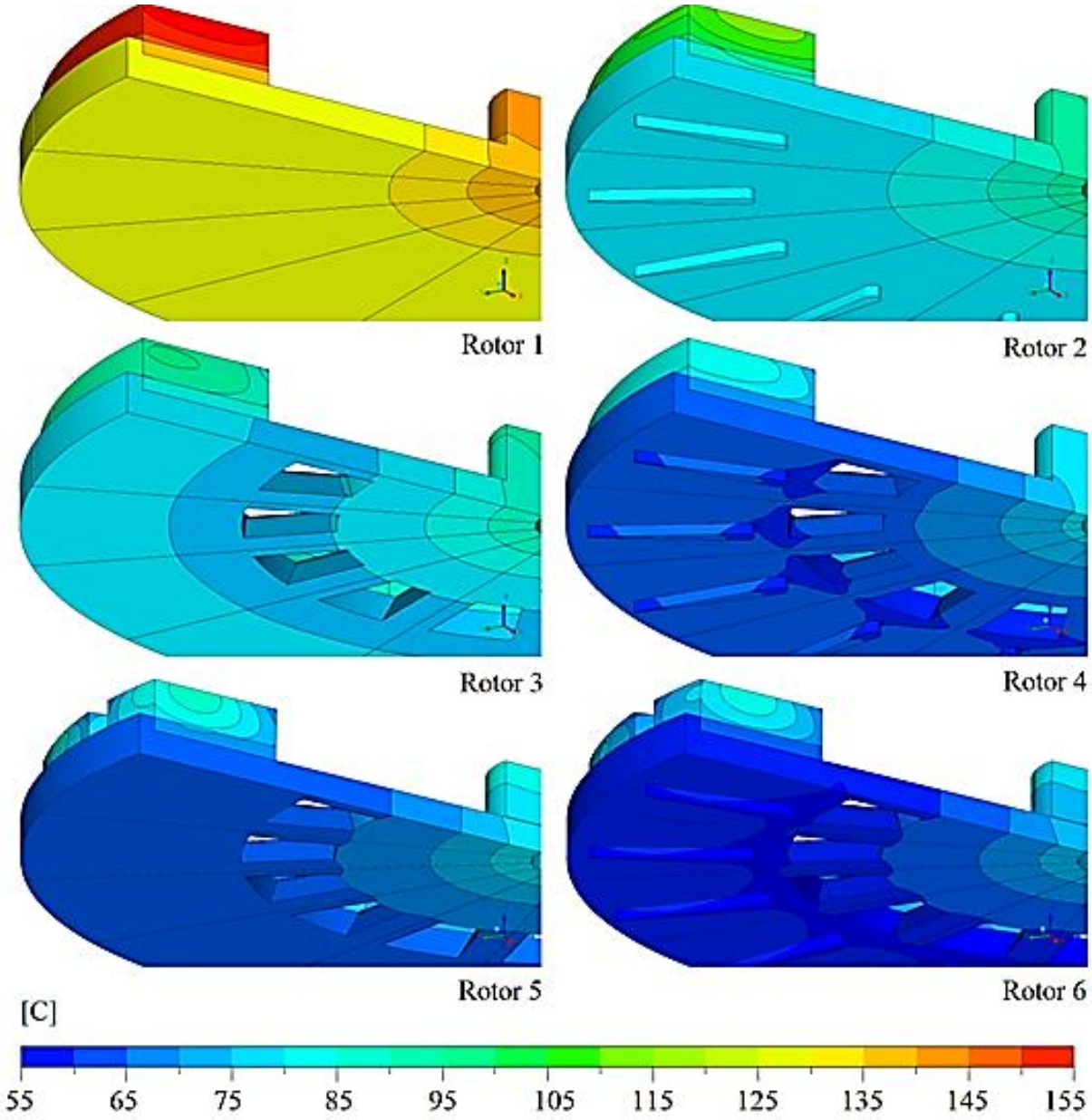

Fig. 4-8 Temperature distribution in the six different presented rotor geometries.

4.2 Cooling Performance Factor, η

For a better comparison of the cooling performance of the presented rotor geometries with respect to the associated windage losses, a cooling performance factor η, expressed in (1), is introduced. T_{limit} resembles the temperature limit of the magnets (150 °C), and Tm is the maximum temperature of the magnets at steady state. This factor measures the power consumed by the rotor in the form of windage losses per each degree drop in the magnets

maximum temperature below its critical limit. A low η indicates a good rotor design, given it is capable of steadily operating at safe magnets operating temperature limit. NdFeB magnets usually operate below or at 100°C in automotive/aerospace applications.

$$\eta = \frac{Windage\ Losses}{T_{limit} - T_m} \tag{64}$$

Five of the presented rotors were compared based on η. The baseline rotor is excluded from the comparison since its maximum temperature is higher than the critical limit. The second rotor is added for comparative purposes, although it does not qualify for safe operation since the magnets temperature exceeds the 100°C threshold.

As shown in Fig. 4-9, Rotor 2 consumes the highest power per degree reduction in magnets temperature. The closed rotor configurations rely only on indirectly cooling the magnets through the rotor carrier. This is an inefficient method due to two main reasons. Firstly, the heat flux path from the magnets to the rotor carrier has a high resistivity. This is imposed by the existence of two insulation layers between the three solid components and the lower conductivity of the cobalt steel back iron compared to the aluminum rotor carrier. Secondly, the development of Batchelor and Eckman layer flow on the inner walls of the rotors causes hot air to recirculate and deteriorate the convection heat transfer on the rotor surfaces.

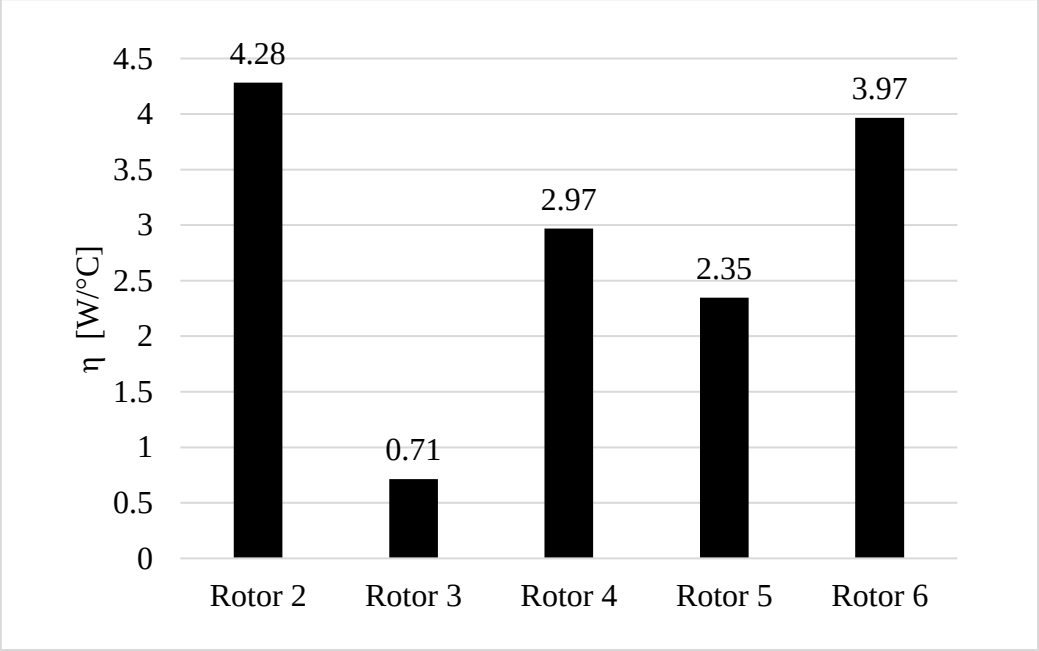

Fig. 4-9 Performance factor for the presented rotor geometries.

This concludes that the closed rotor geometries are the least performing geometries and any efforts to improve their thermal performance through the addition of geometrical features would be inefficient either thermal wise or power wise. It is worth mentioning that the performance of Rotor 2 alike geometries could be improved by modifying the rotor blades as discussed in [72] and [73].

The cooling performance of the other vented geometries varied widely, with the flat vented Rotor 3 having a substantially better performance than other rotors with their added features. However, the maximum temperature is found to be only 5 degrees below the operating temperature limit. Usually, for commercial machines, a safety margin of 10-20 degrees is recommended. Fawzal et al. set 80°C as the maximum rotor temperature limit for their study as specified by the machine manufacturer [72]. The main design advantage of vented rotors is removing the heat directly from the heat-generating source by forcing air directly over the magnets. The rotor's internal flow path can be improved through rotor geometry optimization with a minimal increase in windage losses.

Rotor 5 shows a slightly better performance compared to Rotor 4, but it also has a slightly higher maximum temperature. The better performance seen in Rotor 5 over Rotor 4 emphasizes that the enhancement of rotor internal flow for better direct cooling is usually more efficient than improving the indirect cooling through the rotor carrier.

The addition of fan blades in Rotor 6 geometry is found unreasonable given the minimal gain it offers in terms of thermal performance over the more efficient Rotor 4 and 5. This is reflected on the cooling performance factor which approaches the value of the Rotor 2 that has the worst performance among other presented rotors.

The study showed that vented rotors have superior cooling performance at slightly higher windage losses when compared to their non-vented counterparts. The improvement was found mostly related to the air gap flow type since vented rotors were able to eliminate flow recirculation regions which deteriorate heat transfer at the rotor inner walls. Also, the introduction of magnets protrusions resulted in a 43% improvement in heat transfer compared to gapless magnets as a result of increased mass flow rate. However, the magnets maximum temperature dropped only 7 degrees due to its strong dependency on air gap flow which was found to exhibit core rotation in the case of protruding magnets. The addition of straight fan blades to the rotor enhanced the overall rotor cooling however it increased the windage losses

by at least 86% when compared to their non-bladed equivalent geometries. Such an increase reduced the rotor cooling performance factor by 25% for nearly the same thermal performance. Fan blades increase the air mass flow rate and turbulence over the rotor surfaces which improves the cooling rate when direct cooling is insufficient. Nevertheless, the rather modest thermal conductivities of the rotor components often used (neodymium magnets, epoxy-based adhesives, steel back iron) limit the overall cooling capacity of the rotor blades given the indirect heat path between the cooled rotor surface and the magnets. Such limitations affect the cooling efficiency of rotor blades; Accordingly, it was found to consume higher power (windage losses) per degree °C reduction in magnets temperature when compared to the other mentioned cooling features.

Despite the downsides of the rotor blades, the study showed that they can achieve a superior cooling rate when coupled with rotor vents, resulting in low magnets operating temperature within a reasonable windage losses rate.

It is worth mentioning that the study is performed at a different operation point (5200 RPM) from the other simulations shown later in this chapter. However, the study results are indeed applicable for the continuous power operation condition used for later studies.

Based on the study results, the initial design is set to have a ventilated rotor with embedded radial fan blades and further design changes are made for the mechanical integration of the rotor with the other parts of the motor. Further studies are done for the improvement of the fan blades for better cooling efficiency.

4.3 Rotor Fan Blades Design

The results from the simulations discussed in the last section as well as experimental results from previous studies showed that the rotor of an AFPM machine has a great resemblance to centrifugal/radial fans. Therefore, centrifugal fan design concepts become of great importance when designing an air cooling system for a self-cooled rotor, especially with the integration of embedded fan blades in the rotor body.

The high cooling rate required by the designed machine as a result of its high power density and relatively low permanent magnets thermal threshold, also due to the significant importance of the fan blades to the rotor thermal performance as previously discussed. The rotor design has to be studied while considering the concepts of turbomachinery in order to achieve a thermally sound design without compromising the machine windage losses.

The resemblance of the rotor to radial fans and ventilated brake rotor disks allows the application of the same design concepts to rotor geometry. Nevertheless, blower fan design usually tends to focus on pressure rise, mass flow rate, and fan power as design parameters while the thermal performance of the fan rotor is not usually a concern. Contrarily, rotor brake disc design focuses mainly on the rotor thermal performance with no regard to the fan power/windage loss since it is negligible compared to the power output in a vehicle. Therefore, this work focuses on utilizing both concepts to make the rotor cooling system as efficient as possible.

The heat transfer in the bladed rotor mainly depends on the rotor pumping rate as well as the turbulence over the rotor surfaces which dictates the heat transfer coefficient over it. The flow rate of the radial fan is a function of the blade outlet angle according to Euler equations. While the heat transfer coefficient over the fan rotor is mainly affected by the boundary layer thickness over its surfaces, hence increased turbulence over the rotor surface would result in a thinner boundary layer and higher heat transfer coefficient. Therefore, the rotor blades design should aim to increase the turbulence over the fan blades the surfaces by increasing the relative and meridional speeds of air over the blades and rotor surfaces.

4.3.1 Radial fan design concept

Starting from Euler's incompressible flow equations as the governing equations for the design. The curves shown below for a radial fan with a radial inlet show that the flow rate is a function of the outlet angle. Fig. 4-10 shows that the maximum flow rate of a fan is possible when it has a radial outlet β_2=90°. The high flow rate would result in enhanced heat transfer; however, the radial outlet would compromise the relative velocity *W* of air over the blade surface as shown in Fig. 4-13. Additionally, the radial outlet results in the lowest total to static fan efficiency as shown in Fig. 4-11, so it is expected to have higher losses and power demand compared to its curved counterparts. On the other hand, a curved blade will have a lower flow rate, but it will have higher total to static efficiency and higher relative velocities over the blade surface. Fig. 4-12 shows the radial fan curves at different blade outlet angles. According to the curves, a backward curved blade (β_2<90º) would have a higher efficiency than the radial blade at the same flow rate below flow coefficient, $\varphi \approx 0.55$. However, radial blades are capable of higher flow rates.

Epple et al. [74] presented a case study for the improvement of radial fan performance targeting a higher mass flow rate. According to the study, the following design steps are followed for enhancing their design performance:

1. Reduction of the fan blade outlet angle, $\beta_{2,}$ for a higher total to static fan efficiency.
2. The reduction of mass flow rate due to smaller β_2 can be counteracted by increasing the blade height.
3. Fine-tuning the blade inlet angle β_1 for shockless entry to minimize flow losses.

The author also suggested modifying the inlet radius and inlet blade height to reduce the relative flow velocity on the blades to reduce friction losses. However, the higher relative velocity is beneficial for heat transfer. Accordingly, the opposite effect is targeted for the rotor design.

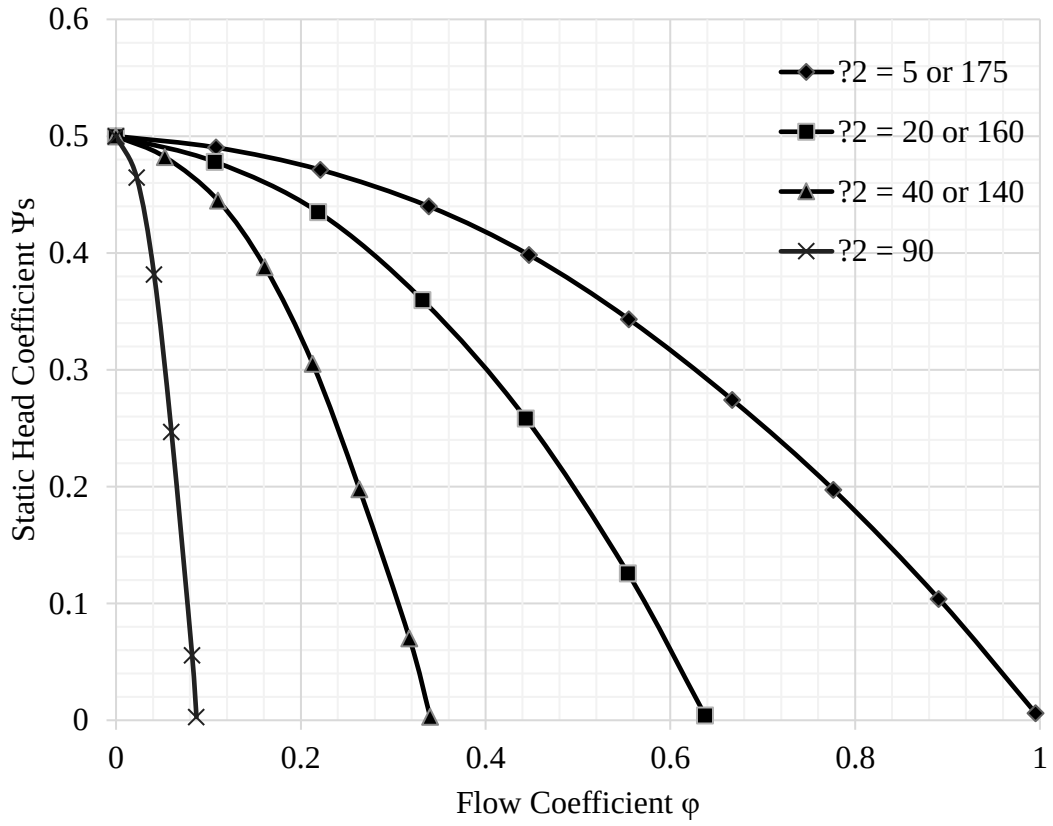

Fig. 4-10 Radial fan performance curves at different blade outlet angles [74].

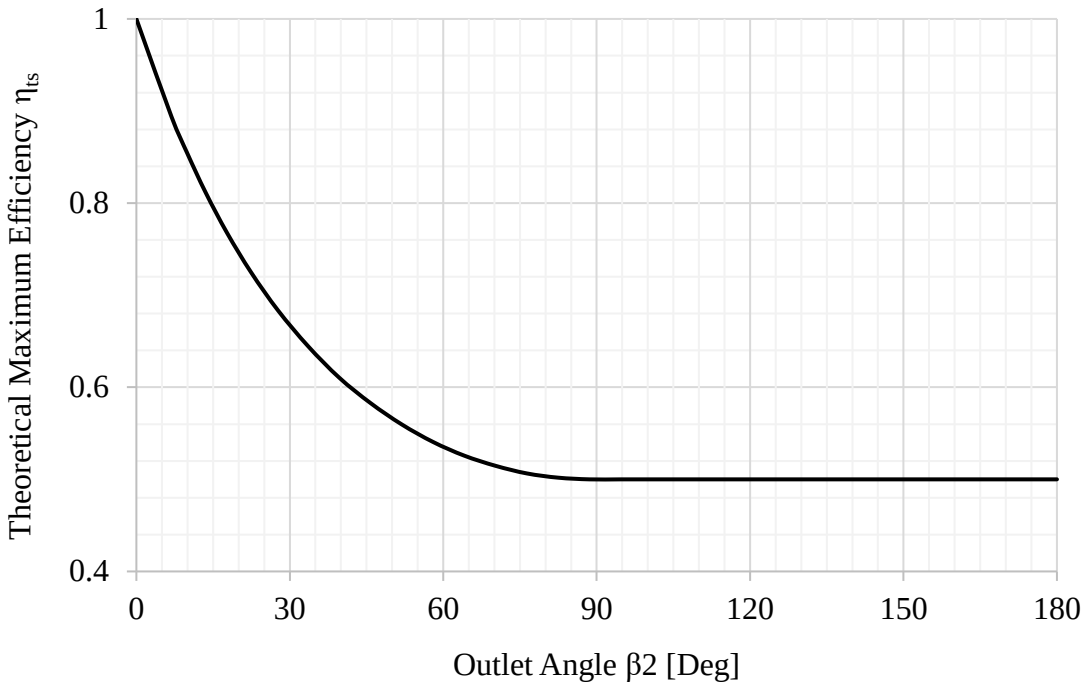

Fig. 4-11 Radial fan theoretical maximum total to static efficiency at different blade outlet angles [74].

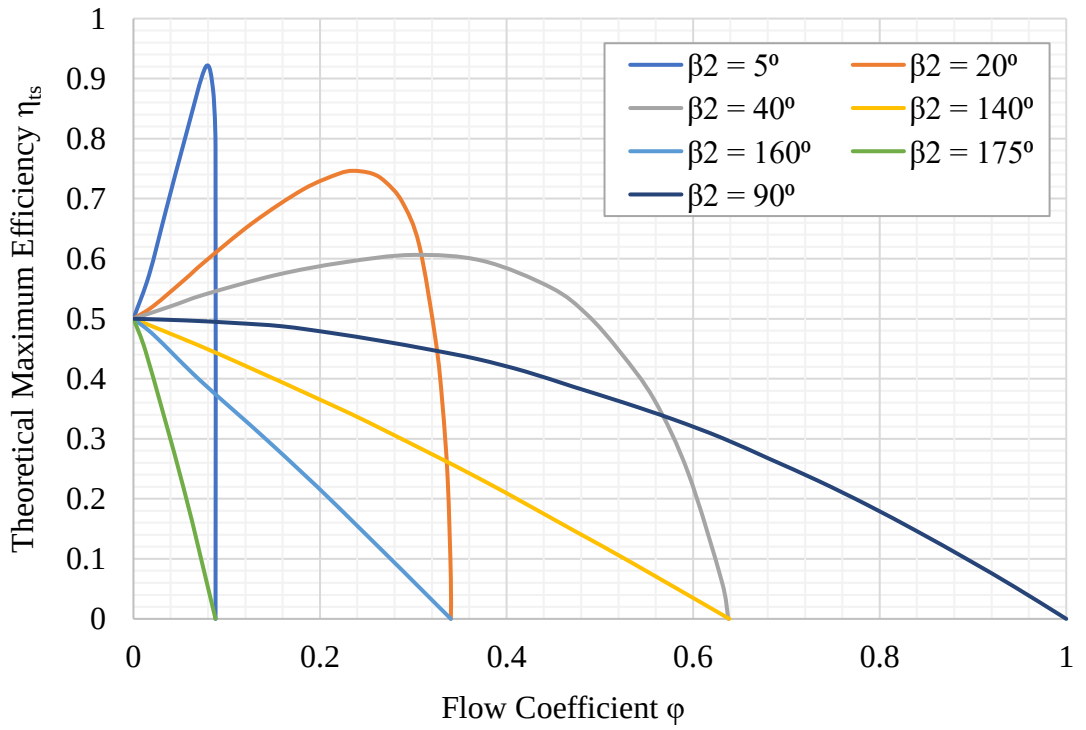

Fig. 4-12 Radial fan efficiency curves at different blade outlet angles [74].

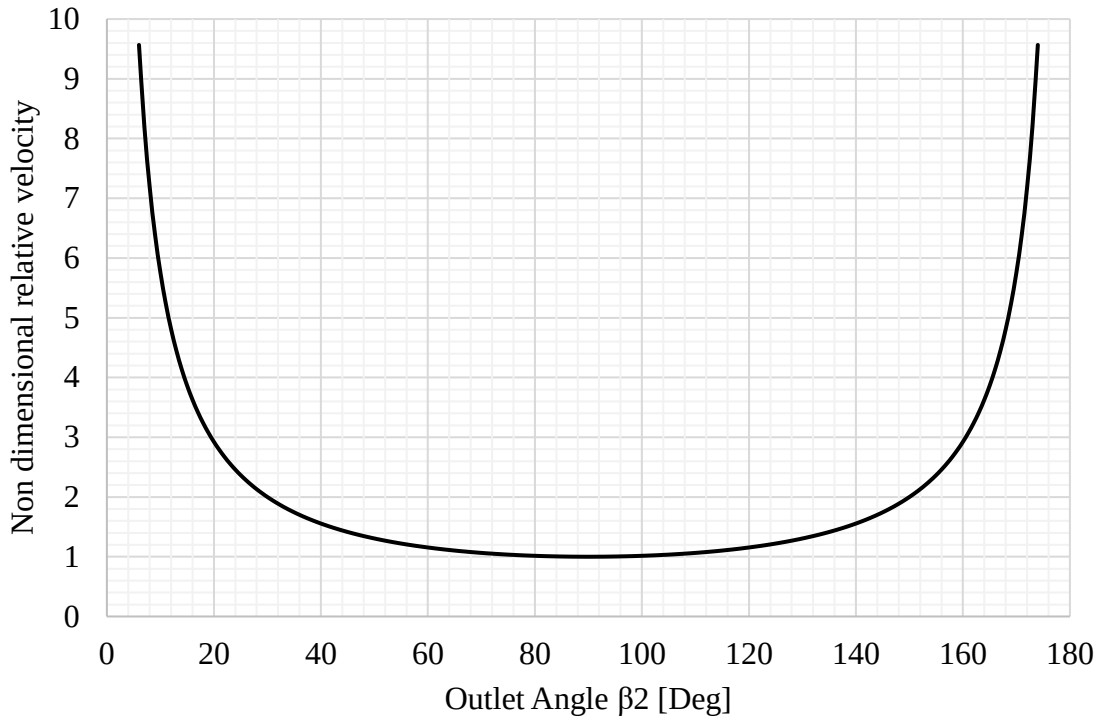

Fig. 4-13 Effect of blade angles on non-dimensional relative velocity over the blade [74].

4.3.2 Radial fan blades

Radial fan blade ($\beta_1 = \beta_2 = 90^o$) is selected for the first design iteration although it has the highest theoretical fan power or windage losses. The selection is made for the following reasons: First, the radial fan blade has the highest theoretical flow rate, therefore studying this geometry allows the assessment of the highest possible mass flow that the rotor is capable of pumping at the given motor operating conditions. Second, to study the effect of mass flow rate on the rotor thermal performance and be able to further compare it to the other curved blade geometries of lower mass flow rate; similarly, knowing the highest fan power associated with the radial blade geometry and further compare it to the curved blades of lower power. Third, the radial fan blade had the highest average heat transfer coefficient, hence better thermal performance compared to the curved and pillar blade type in the study done by Fawzal et al. [72].

Modifications are applied to the simple rotor design presented in section 4.1 along with the revised fan blades design for the following reasons:

1. To allow the rotor to accommodate the other motor components such as the sprag clutch, resolver, and bearing housing in the rotating assembly.
2. To account for the increased mechanical stresses due to the increased nominal speed requirements.
3. Reducing the magnets eddy current losses by using Halbach gapless magnets array instead of conventional surface-mounted magnets poles.

4.3.2.1 Back Plated Rotor, R1

The design concept of the brake rotors studied in [75] and [73] is applied for the rotor design. Unlike the bladed rotor geometry shown in the last section which did not have a back plate covering the blade, this rotor has its blades enclosed by a back plate forming internal channels inside the rotor carrier body. This back plate serves as a mounting surface for the resolver target as well as an additional surface for heat dissipation.

The rotor vents are shifted more towards the inner diameter sharing the same axial inlet with the fan section as shown in Fig. 4-14. This allows the fan section of the rotor to be extended over the entire back of the rotor increasing the effective heat transfer area and without interfering with the other components of the rotor.

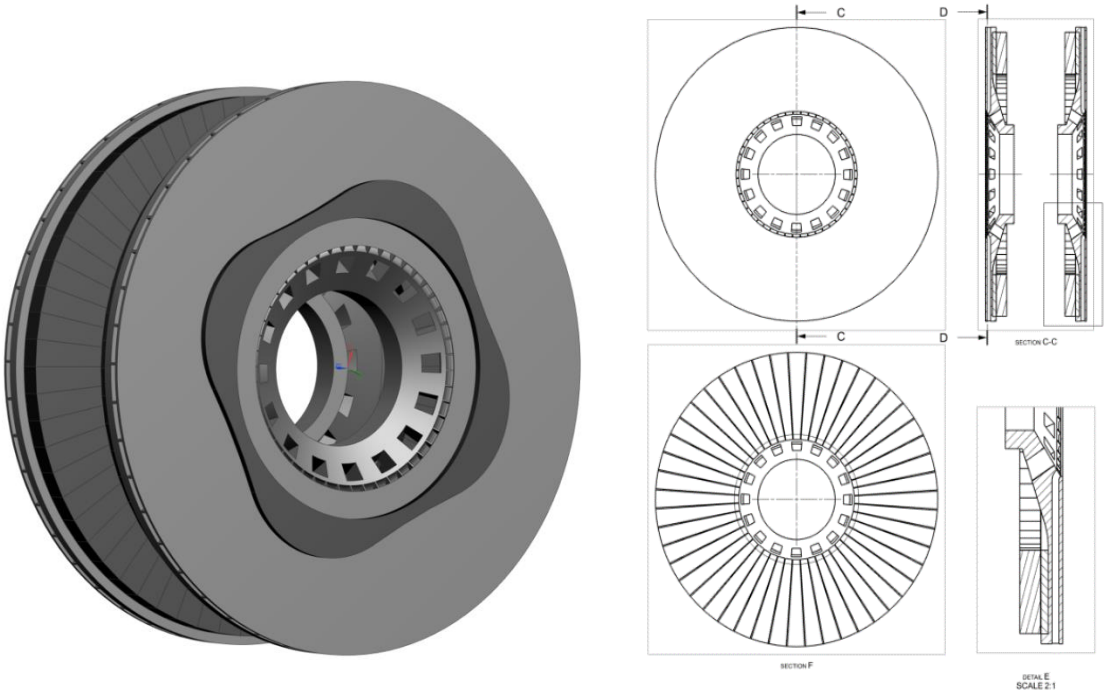

Fig. 4-14 R1 rotor design, Back plated rotor with radial blades.

The rotor design parameters and key results from the simulation at the machine nominal load is as shown below:

Design Parameters		
Blade Outlet Angle, β_2		90°
Blade Inlet Angle, β_1		90°
Number of Blades		48
Inlet Radius, r_1		102 mm
Outlet Radius, r_2		119 mm
Constant Blade Height, b		3 mm
Lean Angle, λ		0°
Key Results		
Mass Flowrate, $\dot{m}$		81.8×10^{-3} [kg/s]
Average Heat Transfer Coefficient, $\bar{h}$	$\bar{h}_{Rotor}$	204.4 [W/m^2.K]
	$\bar{h}_{magnets}$	69.1 [W/m^2.K]
	$\bar{h}_{Rotor\ Carrier}$	158.5 [W/m^2.K]
Power (Windage Loss), P		486.9 [W]
Maximum Magnets Temperature, T_{max}		86.5 [°C}
Cooling Performance Factor, η		7.67 [W/K]

Table 6 Design parameters and key simulation results of R1 rotor.

The design allows the magnets to be at a safe operating temperature, The maximum recorded temperature within the magnets was 86.5 °C with enough safety margin below the threshold at 100 °C. The temperature contours below show that the highest temperature in the rotor is near the bearings, while the lowest temperature is at the backplate near the inlet with a marginal increase in its temperature near the outlet. This indicates the high cooling intensity at the backplate as a result of its large surface area and the fact that it is being cooled on both sides.

The internal blades of the rotor do not only pump the air through it, but they also act as heat-dissipating fins. This can be observed through the variation of the temperature at the rotor carrier circumference near the outlet upper edge where lower temperature regions surrounded the blades. Oppositely, lower temperatures are found in between the blades due to the higher cooling rate on the backplate as it acts as a larger fin.

The static pressure contours below show the pressure development in the rotor channels reaching a maximum at the outlet. This is due to the exchange of angular momentum as well as the diffuser effect of these channels since the increase in the flow area in the radial direction

is not compensated by the reduction of the channel height. Moreover, increased pressure in the internal cavity of the rotor resulted in major blockage of the flow through the vents as shown in the streamlines in Fig. 4-14. Higher pressure is seen near the back iron due to the entrapment of air near the corner by Eckman layer flow inside the cavity.

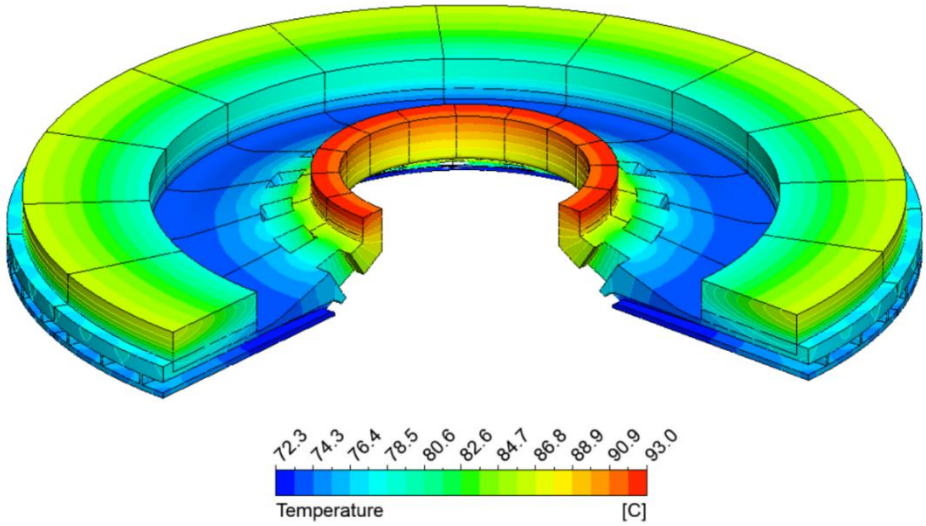

Fig. 4-15 Temperature distribution in R1 rotor.

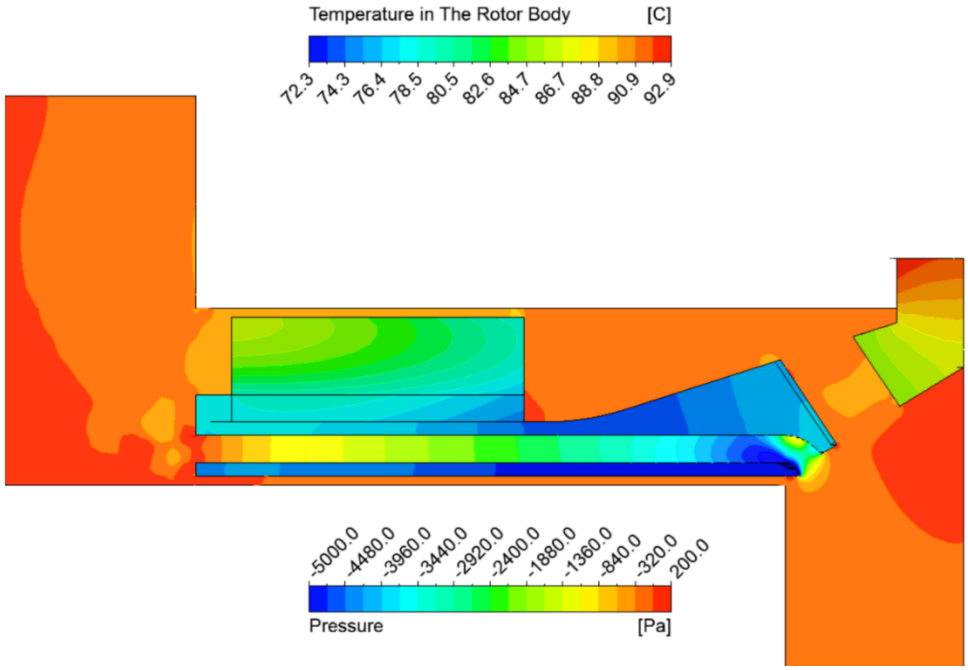

Fig. 4-16 Static pressure distribution in through R1 rotor.

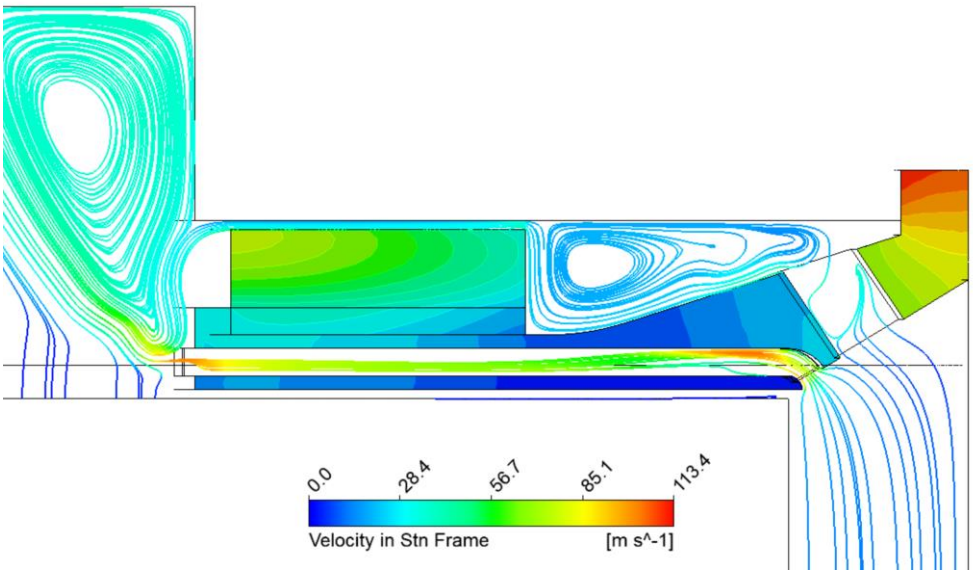

Fig. 4-17 Flow streamlines through R1 rotor.

4.3.2.1.1 Back Plated Rotor with Bleed Vents, R2

The reduced outlet size in the rotor shown in Fig. 4-18 along with the bleed between the rotor inner cavity and the inter-blades channels results in better flow and pressure distribution through the rotor carrier. Accordingly, its average heat transfer coefficient slightly increased. However, the flow through the air gap deteriorated hence the average HTC over the magnets dropped to nearly half of that found in the former rotor. As discussed earlier, the direct heat transfer through the magnet surfaces is more critical to its thermals than the indirect heat transfer through the rotor carrier. This explains the noticeable rise in the magnets temperature compared to the rotor without the bleed vents.

Design Parameters	
Blade Height at Inlet, b_1	3 mm
Blade Height at Outlet, b_2	1.5 mm
Blade Outlet Angle, β_2	90°
Blade Inlet Angle, β_1	90°

Key Results		
Mass Flowrate, $\dot{m}$		78.5 $\times 10^{-3}$ [kg/s]
Average Heat Transfer Coefficient	$\bar{h}_{Rotor}$	267.8 [W/m^2.K]
	$\bar{h}_{magnets}$	33.8 [W/m^2.K]
	$\bar{h}_{Rotor\ Carrier}$	163.1 [W/m^2.K]
Power (Windage Loss), P		439.7 [W]
Maximum Magnets Temperature, T_{max}		90.2 [°C}
Cooling Performance Factor, η		7.3 [W/K]

Table 7 Design parameters and key results of R2 rotor.

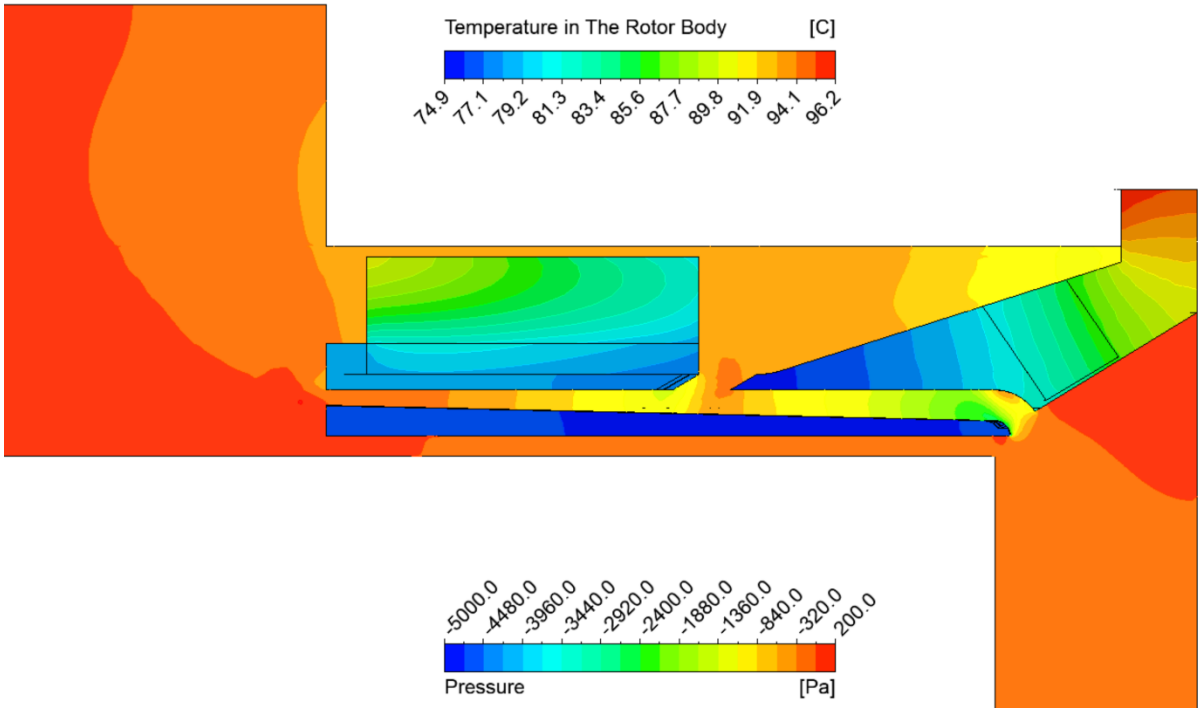

Fig. 4-18 Static pressure distribution through R2 rotor.

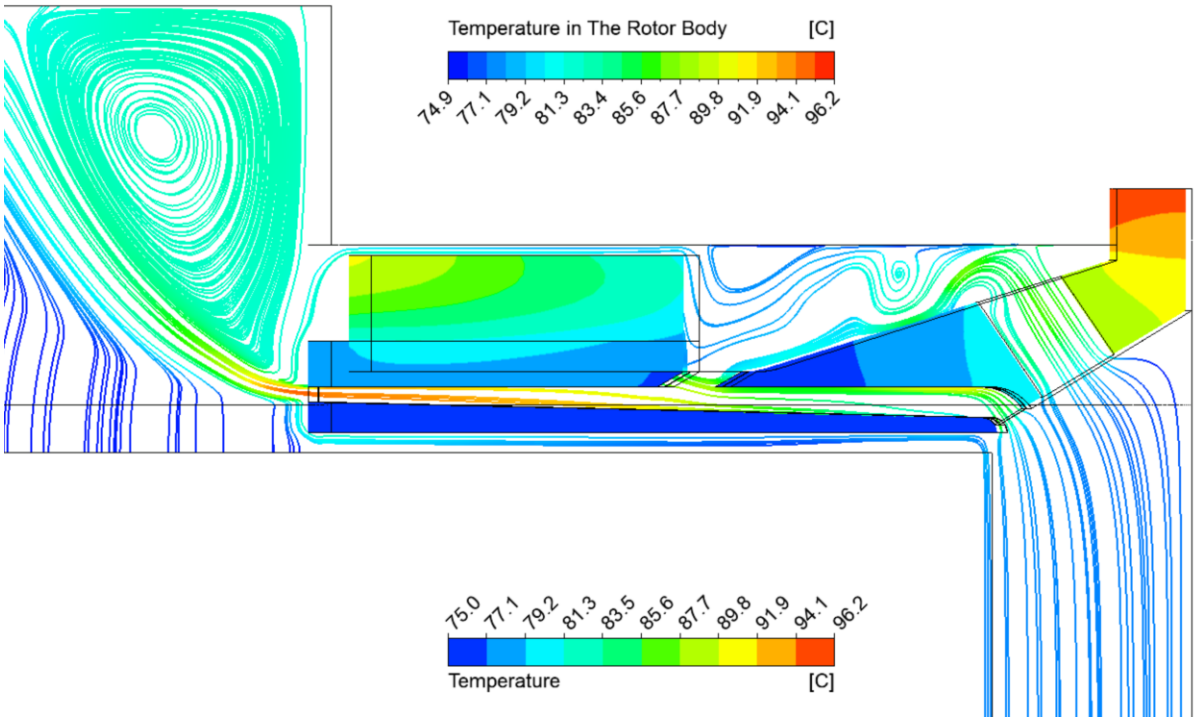

Fig. 4-19 Static pressure distribution through R2 rotor.

4.3.2.2 Open Channeled Rotor, R3

The open channeled rotor without a back plate is studied in effort to make the design easier to manufacture. The resolver target in this design is mounted on the blades to eliminate the need for the back plate as a mounting surface. Also, a sprag clutch is introduced to the motor which occupies a larger space of the motor inner diameter compared to having a motor shaft only. Accordingly, the vent geometry and the number of blades are changed to allow for axially mounting the rotor to the motor drive hub. The rotor carrier thickness is increased near the mounting region where there it is highly possible for the rotor to cone due to stresses. The rotor thick section was later extended to its inner diameter in the finalized mechanical design. The blade height is increased to include height occupied previously by the back plate. The blade lean angle is increased to keep higher velocity gradients near the rotor back surface.

Fig. 4-20 R3 rotor design, open channeled rotor with radial blades.

The rotor temperature contours show that the open channeled rotor is comparable to the back plated rotor despite the smaller effective area of heat transfer of the former. This is due to the higher average heat transfer coefficient over both the rotor carrier and magnets as well as the higher pumping rate of the open channeled rotor.

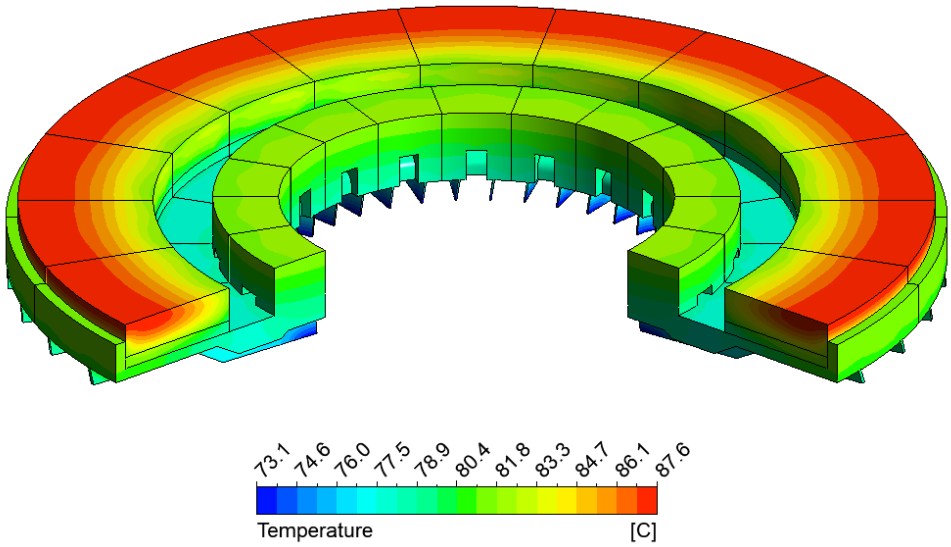

Fig. 4-21 Temperature distribution in R3 rotor.

Design Parameters		
Blade Outlet Angle, β_2		90°
Blade Inlet Angle, β_1		90°
Number of Blades		48
Inlet Radius, r_1		50 mm
Outlet Radius, r_2		119 mm
Constant Blade Height, b		4 mm
Lean Angle, λ		20°
Key Results		
Mass Flowrate, $\dot{m}$		116.7×10^{-3} [kg/s]
Average Heat Transfer Coefficient, $\bar{h}$	$\bar{h}_{Rotor}$	216.6 [W/m^2.K]
	$\bar{h}_{magnets}$	86.7 [W/m^2.K]
	$\bar{h}_{Rotor\ Carrier}$	302.8 [W/m^2.K]
Power (Windage Loss), P		704 [W]
Maximum Magnets Temperature, T_{max}		87.5 [°C}
Cooling Performance Factor, η		11.3 [W/K]

Table 8 Design parameters and key results in R3 rotor.

The increased mass flow rate is due to a larger flow area and reduced flow blockage at the inlet as a result of increased blade height and the smaller number of blades. The increased number of blades results in geometric blockage which when combined with the flow blockage due to separation at the leading edge shown in Fig. 4-22 can significantly deteriorate the pumping capability of the rotor. Although the increased mass flow rate is beneficial for the heat transfer, the reduced number of blades also reduced the effective heat transfer area of the rotor.

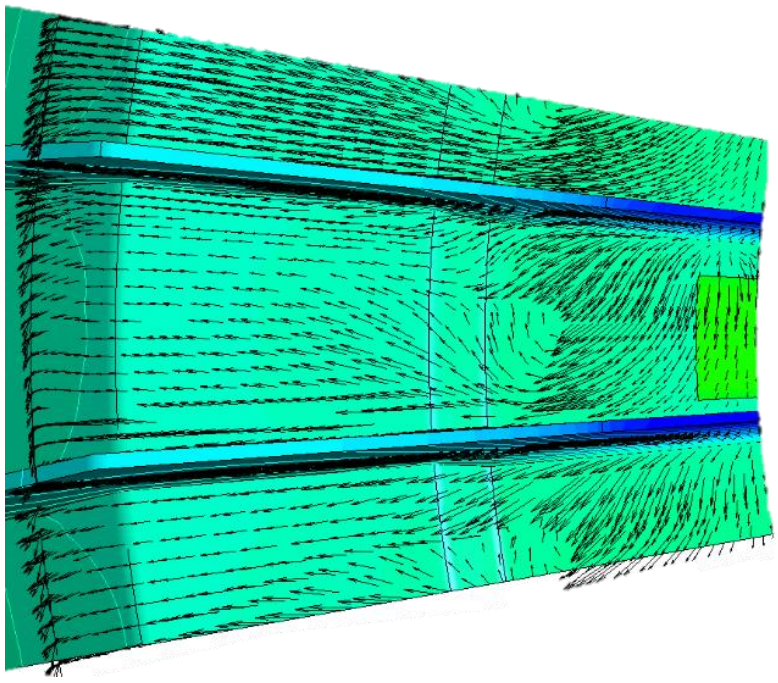

Fig. 4-22 Flow velocity vectors in between the radial rotor blades in R3 rotor.

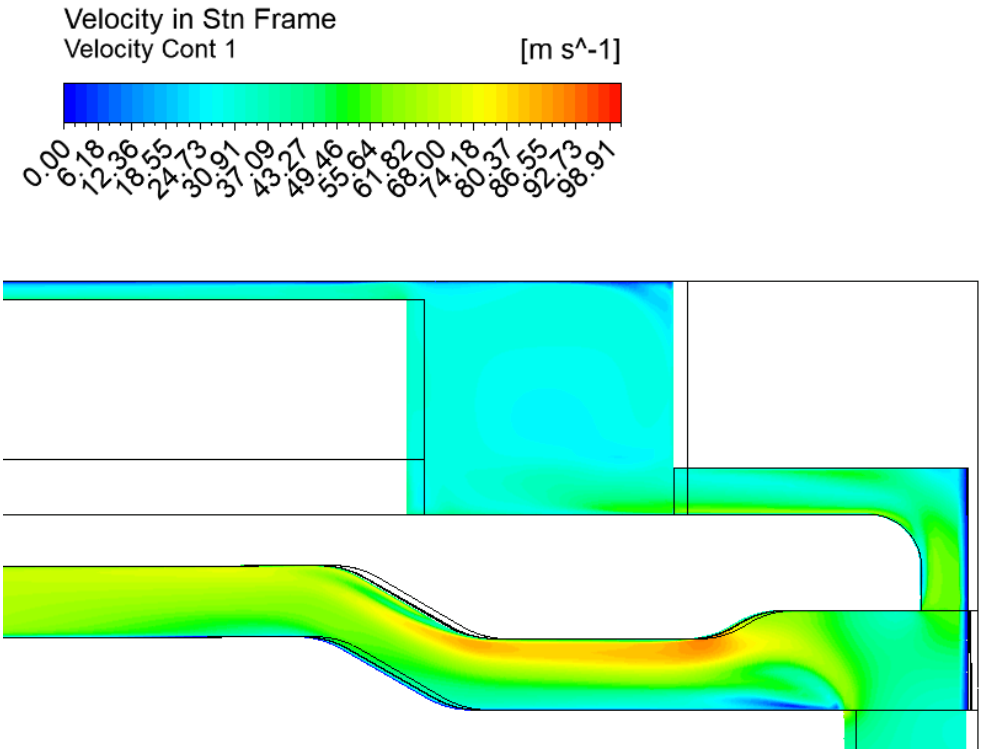

Fig. 4-23 Velocity contours through the R3 rotor.

The relatively smaller vents at the rotor inner diameter allow a throughflow through the rotor cavity. The flow exhibited Eckman layer flow at the rotor cavity similar to the previous geometry. However, the increased average heat transfer coefficient at the magnets surface indicates the better performance of the new vents in cooling the rotor internal surfaces.

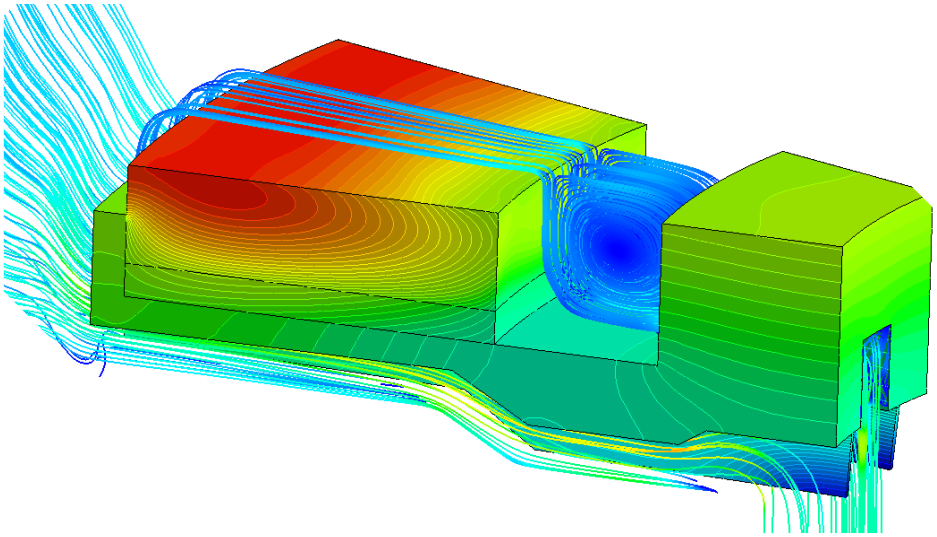

Fig. 4-24 Streamlines of the meridional flow velocity through R3 rotor.

According to Euler equations, the shaft power is directly proportional to the flow rate so as a result of the increased pumping capacity of the open channeled rotor, the inherently high power of the radial fan is increased.

As discussed earlier, the machine considerations require that the windage power loss should not exceed a 500 W limit. Although the radial fan maintained an adequate cooling rate keeping the rotor temperature far below its threshold, the fan blades design has to be further improved to maintain the same thermal performance at lower windage losses.

4.3.3 Backward curved fan blades

By reviewing Euler equations and radial fan curves, it is concluded that the backward curved blades can reduce the fan hydraulic power, while also increasing the fan total to static efficiency theoretically. The combined effect can result in a significant reduction in the shaft power, hence reduced windage loss. The backward curved fan would however reduce the fan pumping capacity in results. Nevertheless, backward curved blades have higher relative velocities over the blades which can increase the heat transfer through increased turbulence countering the effect of reduced mass flow rate.

Fig. 4-25 R4 rotor design, rotor with backward curved fan blades.

The new rotor has the same carrier geometry as the previously studied rotor, but the rotor carrier thickness is kept constant past the inlet to avoid the flow separation due to the thickness step shown in the figure above. The new blade geometry has a circular arc shape; this type of blade is easily computed since there is only one possible arc between the predefined inlet and outlet angles.

The inlet angle is fine-tuned to avoid shock entry loss and flow blockage due to flow separation at the fan inlet. The angle is selected based on a separate simulation where the radial inlet was first tested. The outlet angle is selected based on the radial fan geometry of a different application. This blade geometry is tested as an initial iteration to estimate the potential reduction in windage losses as well as the thermal performance of backward curved blades.

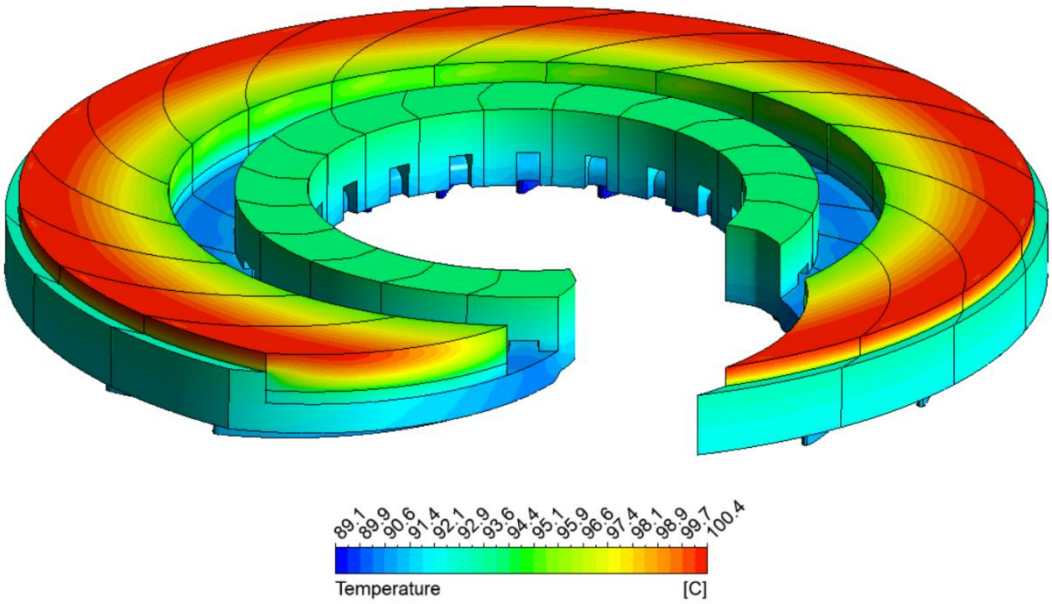

Fig. 4-26 Temperature distribution in R4 rotor.

Design Parameters		
Blade Outlet Angle, β_2		24°
Blade Inlet Angle, β_1		57°
Blade Height at Inlet, b_1		5.5 mm
Blade Height at Outlet, b_2		4 mm
Number of Blades		20
Inlet Radius, r_1		60 mm
Outlet Radius, r_2		114 mm
Lean Angle, λ		0°
Key Results		
Mass Flowrate, $\dot{m}$		80.9×10^{-3} [kg/s]
Average Heat Transfer Coefficient	$\bar{h}_{Rotor}$	155 [W/m^2.K]
	$\bar{h}_{magnets}$	56 [W/m^2.K]
	$\bar{h}_{Rotor\ Carrier}$	224 [W/m^2.K]
Power (Windage Loss), P		193.4 [W]
Maximum Magnets Temperature, T_{max}		100.4 [°C]
Cooling Performance Factor,		3.9

Fig. 4-27 Design parameters and key results of R4 rotor.

The results show a significant reduction in mass flow of the backward curved fan blades compared to the radial ones. Accordingly, the heat transfer deteriorates over the rotor surfaces, and the temperature of the magnets increases as a result. Although the radial fan has better thermal performance, the average relative air velocity over the fan surfaces in the backward curved fan is 54% higher on the backward curved blades. Also, the rotor carrier with the backward curved fan dissipated slightly more heat than the other rotor.

The figure below (Fig. 4-28) shows the velocity vectors of the flow at the blade inlet. The radial inlet shown in the left image resulted in flow separation accompanied by a wake region at the blade suction side, while the revised inlet angle has a uniform flow between the blades. This results in more uniform heat transfer over the rotor carrier surfaces and eliminates the flow blockage due to flow separation between the blades.

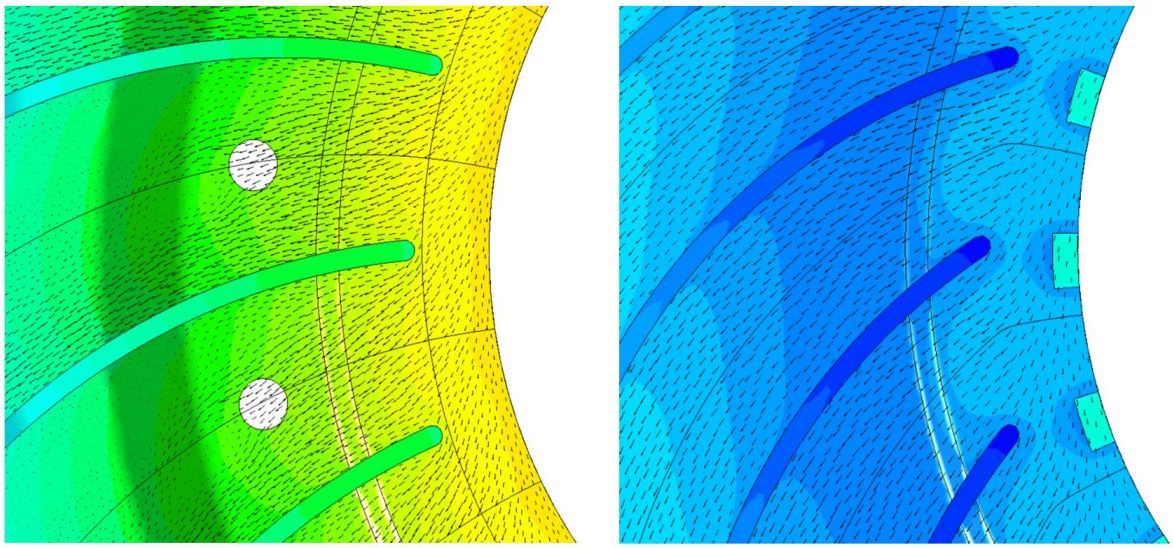

Fig. 4-28 Flow velocity near the backward curved blade leading edges showing the flow separation due to the misaligned inlet angle (left) in comparison with the blade-aligned flow after inlet angle correction (right).

4.3.3.1 Rotor Blades Geometry Improvement

The backward curved blade showed a significantly lower windage power loss. Although the thermal performance is compromised, it is noticed that the reduction in the heat transfer coefficient is not proportional to the reduction in the windage loss. This is due to the effect of the increased relative velocity over the rotor surface as a result of reducing the blade outlet angle which enhances the surface transfer.

In the following rotor R5 design, the blade outlet angle is increased. The increased blade angle has a higher theoretical flow coefficient, hence better mass flow rate and increased heat transfer. The blade inlet diameter is increased to reduce the total pressure development in the fan and the fan power as a result. The blade inlet angle is changed accordingly to ensure the alignment of the flow at the new inlet diameter. The blade height was increased at the inlet to increase the geometrical flow area hence the maximum flow rate. The blade height downstream of the inlet was computed based on the equation shown in Table 9. Epple et al. [74] discussed different approaches for blade height computation. The constant meridional velocity C_m (r) = const. suggested by Pantell [76] and Eckert and Schnell [77] is followed. This is to ensure appropriate distribution of meridional velocity without abrupt deceleration due to expansion as the flow area increase in the radial direction in case of constant blade height.

Fig. 4-29 Rotor R5 design with improved backward curved blades.

The blade outlet angle is fine-tuned to maximize the flow ratio of the backward curved at the highest possible total to static efficiency. The angle is improved with no regards to the maximum pressure drop. The graph below (Fig. 4-30) shows the flow coefficient at the maximum fan efficiency at different outlet angles [74].

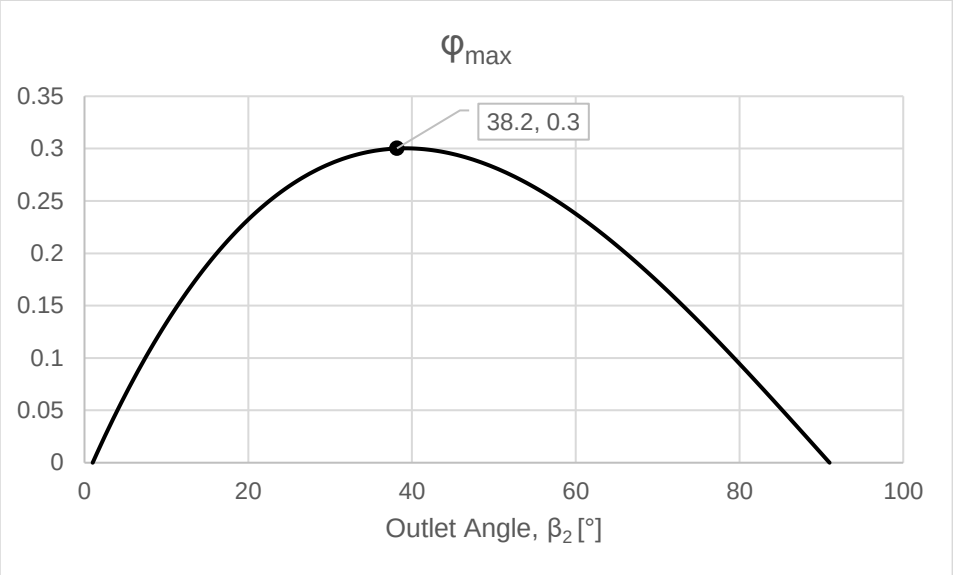

Fig. 4-30 Flow coefficient variation with blade outlet angle.

The design provides a sufficient cooling rate to keep the magnets temperature 6 degrees below its threshold at a relatively low rotor windage loss compared to the maximum allowable value as well as the other designs. The enhanced heat transfer can be related to the high relative flow velocity over the rotor carrier surfaces in addition to the high mass flow rate compared to the other designs.

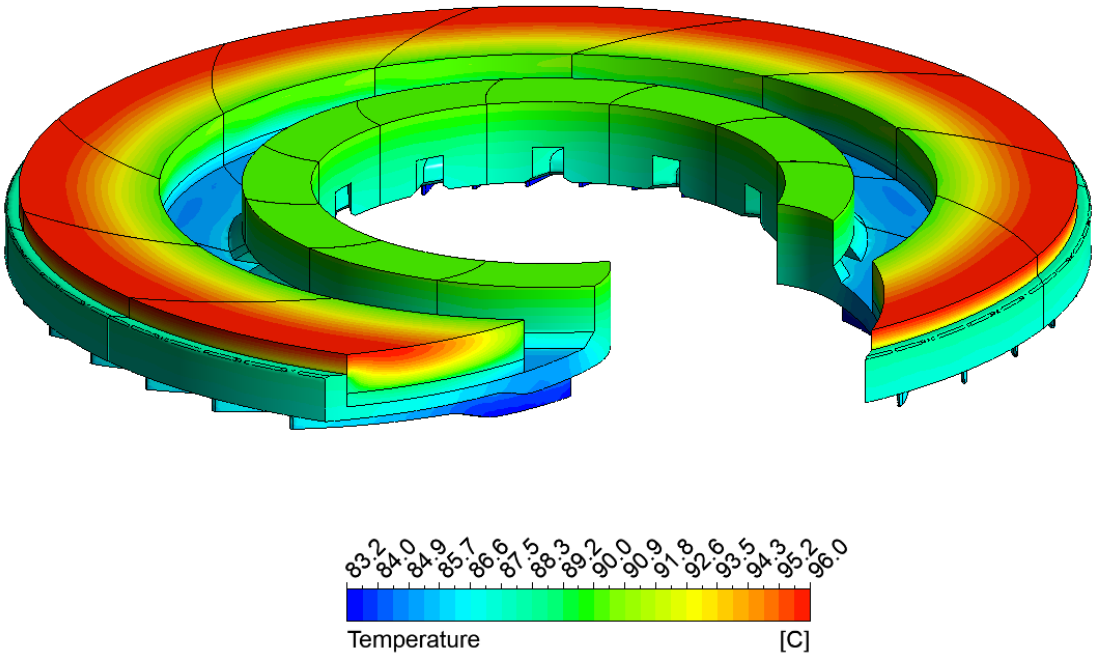

Fig. 4-31 Temperature distribution in rotor R5.

Design Parameters		
Blade Outlet Angle, β_2		38°
Blade Inlet Angle, β_1		50°
Blade Height		$\frac{2.26 \times 10^{-4}}{r}$
Number of Blades		36
Inlet Radius, r_1		66.5 mm
Outlet Radius, r_2		115 mm
Lean Angle, λ		25°
Key Results		
Mass Flowrate, $\dot{m}$		135 $\times 10^{-3}$ [kg/s]
Average Heat Transfer Coefficient	$\bar{h}_{Rotor}$	264.665 [W/m^2.K]
	$\bar{h}_{magnets}$	66 [W/m^2.K]
	$\bar{h}_{Rotor\ Carrier}$	328.7 [W/m^2.K]
Power (Windage Loss), P		300 [W]
Maximum Magnets Temperature, T_{max}		93.6 [°C]
Cooling Performance Factor,		5.32

Table 9 Design parameters and key results of rotor R5.

The results show the sufficiency of the design in terms of thermal performance and acceptable windage losses, and that it can be used for an initial prototype. Further optimization can be done to the rotor geometry. However, it is decided to proceed with this design for the next design task involving the full assembly including the rotor housing.

Blade Configuration	Rotor R3 β_2=90º	Rotor R4 β_2=28º	Rotor R5 β_2=38º
Max. Magnets Temperature [ºC]	87.6	100.4	96.1
Avg. Magnets Temperature [ºC]	84.6	97	92.2
Avg. Rotor Carrier Temperature [ºC]	80.4	92	87.3
Average Magnets Heat Transfer Coefficient, $\bar{h}_{\text{magnets}}$ [W/m^2.K]	86.7	56	66
Average Magnets Heat Transfer Coefficient, $\bar{h}_{\text{carrier}}$ [W/m^2.K]	302.8	224	328.7
Q Magnets Percentage %	11.2	7.1	7.1

Q Rotor Carrier Percentage %	88	92.4	92.5
Ave. Relative Velocity on Carrier W[m/s]	6.7	10.4	25.4
Max. Relative Velocity on Carrier W[m/s]	96.4	62.7	69
Mass Flowrate [kg/s]	0.117	0.092	0.135
Windage Loss [W]	704	193.4	284.5
η [W/K]	11.3	3.9	5.3

Table 10 Summary of thermal performance of the different studied rotors with different outlet blade angles.

By comparing the different designs side to side, the blade angle shows to have a great influence on the thermal performance of the rotor.

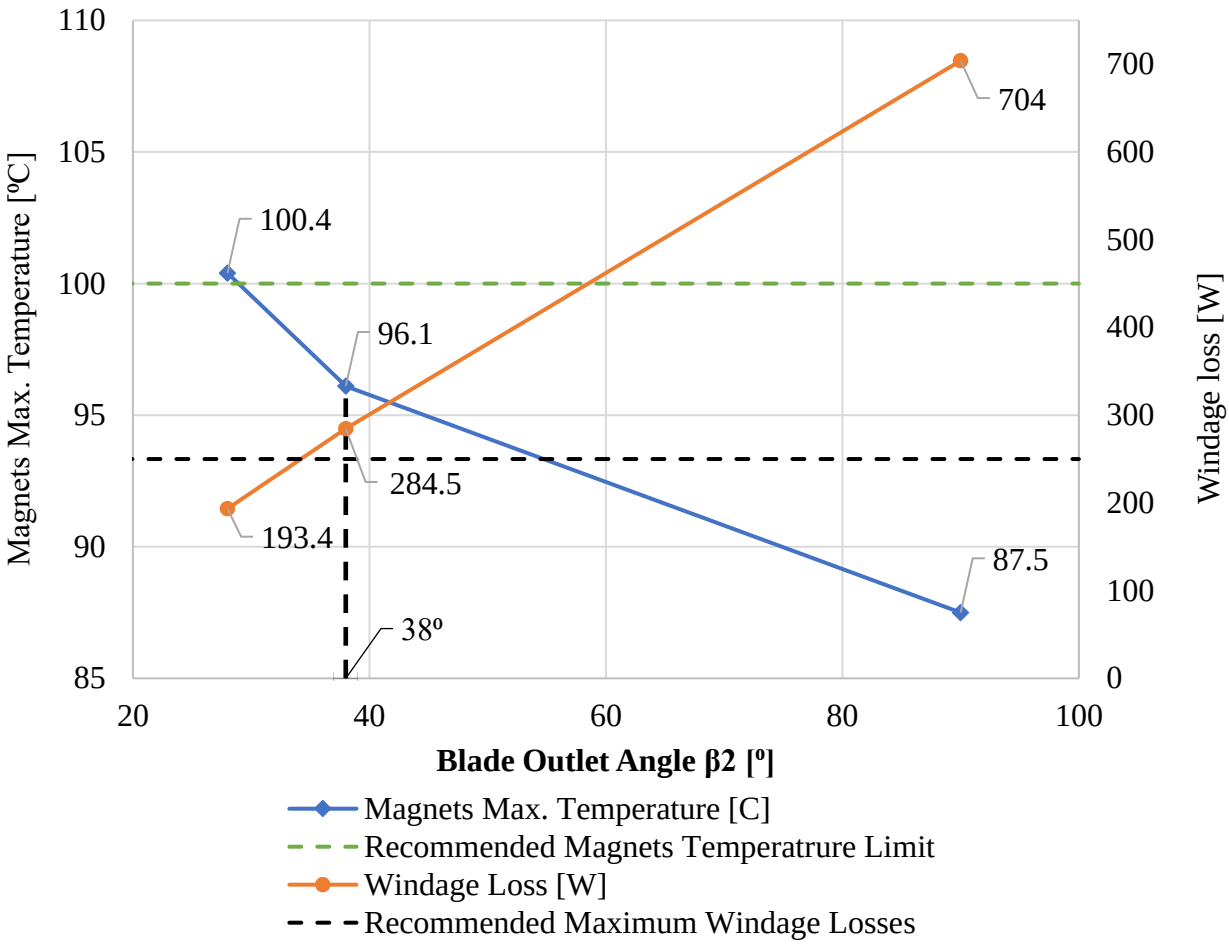

Fig. 4-32 Effect of rotor blades outlet angle on magnets temperature and windage losses.

4.3.4 Surface turbulence effect on rotor heat transfer

The previous study on rotor geometry features emphasized the significant effect of turbulence over rotor surfaces in enhancing the overall heat transfer. The analysis of the final backward curved blade fan showed agreeing results. The figure below (Fig. 4-33) shows the correspondence of zones of high local heat transfer coefficient to the regions of increased surface turbulence kinetic energy. The high turbulence kinetic energy over the backward

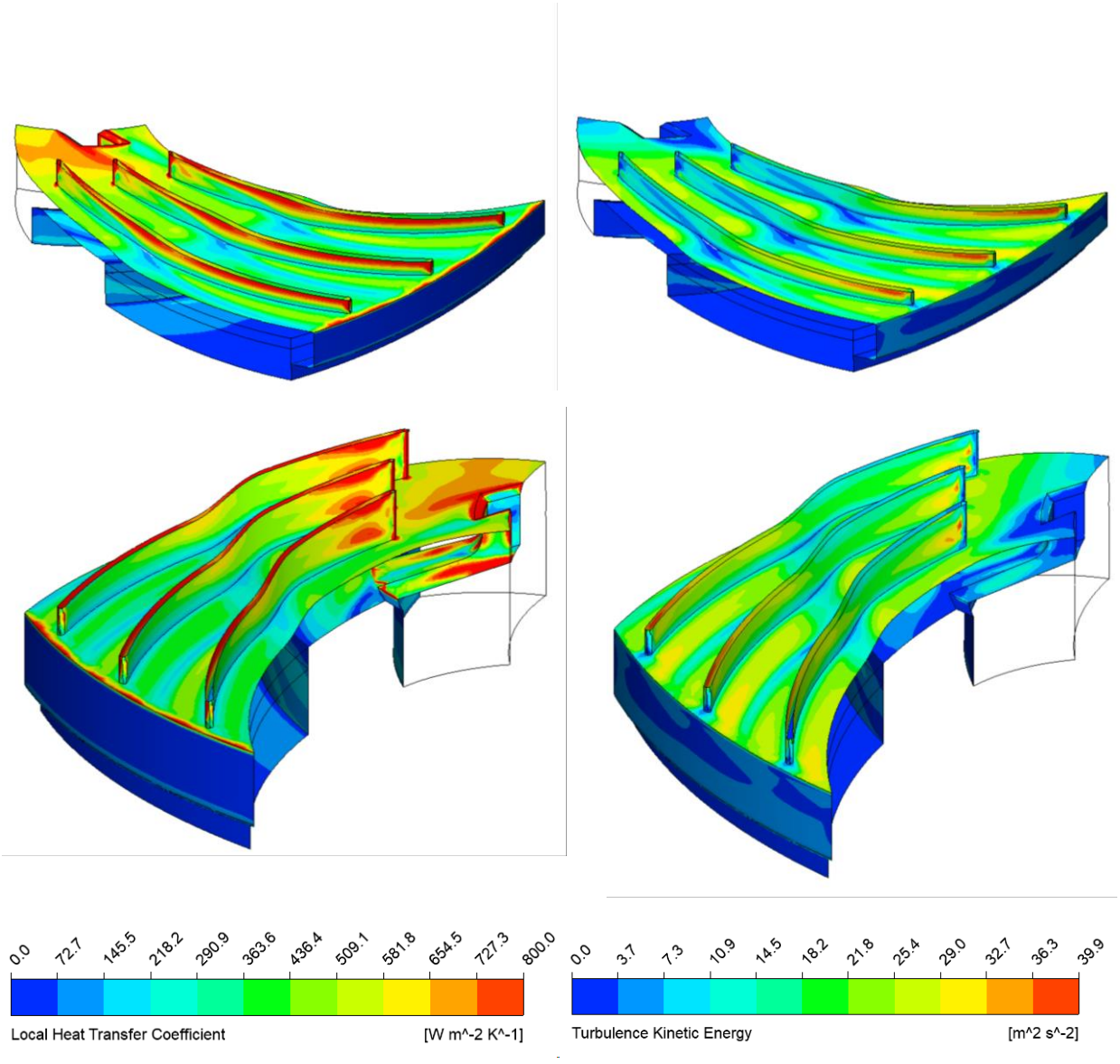

Fig. 4-33 Effect of turbulence kinetic energy (left) on local heat transfer (right) at the rotor/blades surface.

curved fan blades can be associated with the inherently high relative velocities due to the reduced outlet angle.

The contours over the blade surfaces show the effect of different flow patterns over the pressure and suction sides. The suction side appears to have a nearly uniform heat transfer coefficient with a peak where the flow reattachs over the blade past the separation at the leading edge as shown in Fig. 4-34. On the other hand, the local heat transfer coefficient on the blade pressure side has a gradient in the axial direction corresponding to the strong shear forces over its surface. A narrow region of reduced heat transfer at the blade inlet is a result of the interference of two separations zones, the one at the blade leading edge and the other one from the 90° centrifugal inlet as shown in Fig. 4-35.

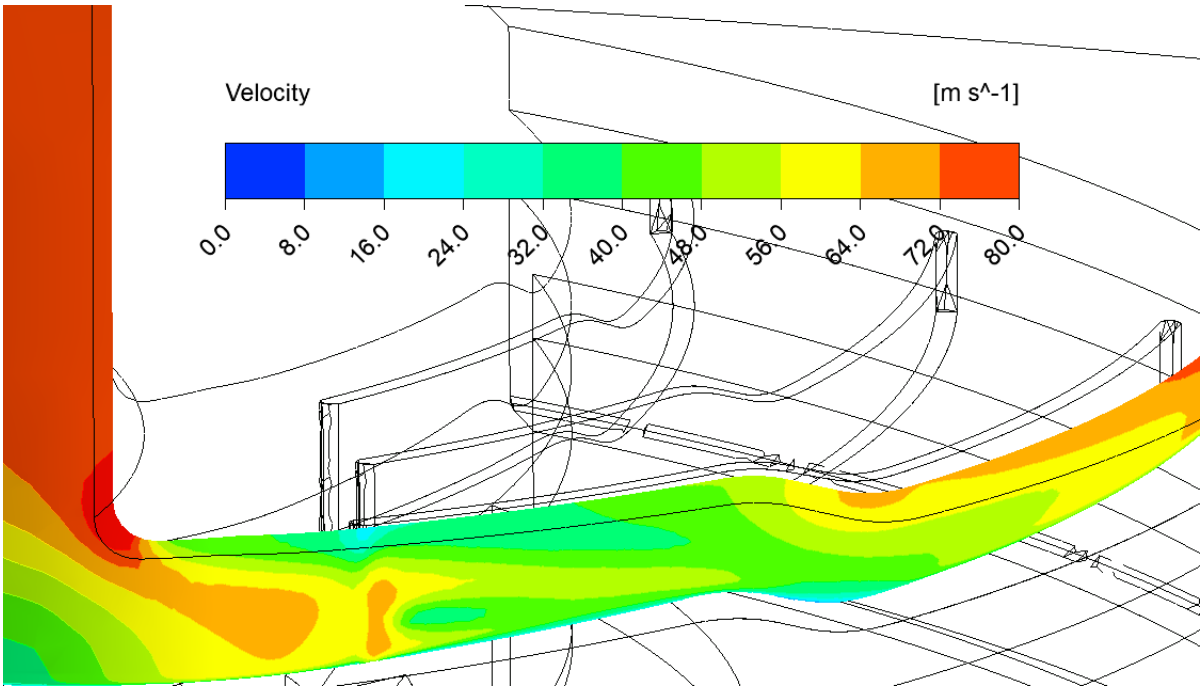

Fig. 4-34 Flow velocity contours midplane in-between the rotor blades suction and pressure sides.

The local heat transfer contours show the effect of the inter-blades flow patterns on heat transfer. The local heat transfer coefficient contours on the rotor carrier back side show a nearly uniform value with a peak near the inlet region due to flow impingement. A narrow region of reduced heat transfer separating two regions of higher local heat transfer coefficient is seen near the outlet. This is a result of the minimal flow separation over the pressure side

of the blade which then reattachs near the blade outlet as shown in the velocity contours below. Another flow separation appears at the step at the rotor carrier back which also results in a slight reduction in the local heat transfer coefficient. The results are found to be agreeing with the analysis made for a similar setup for a ventilated brake rotor in [73].

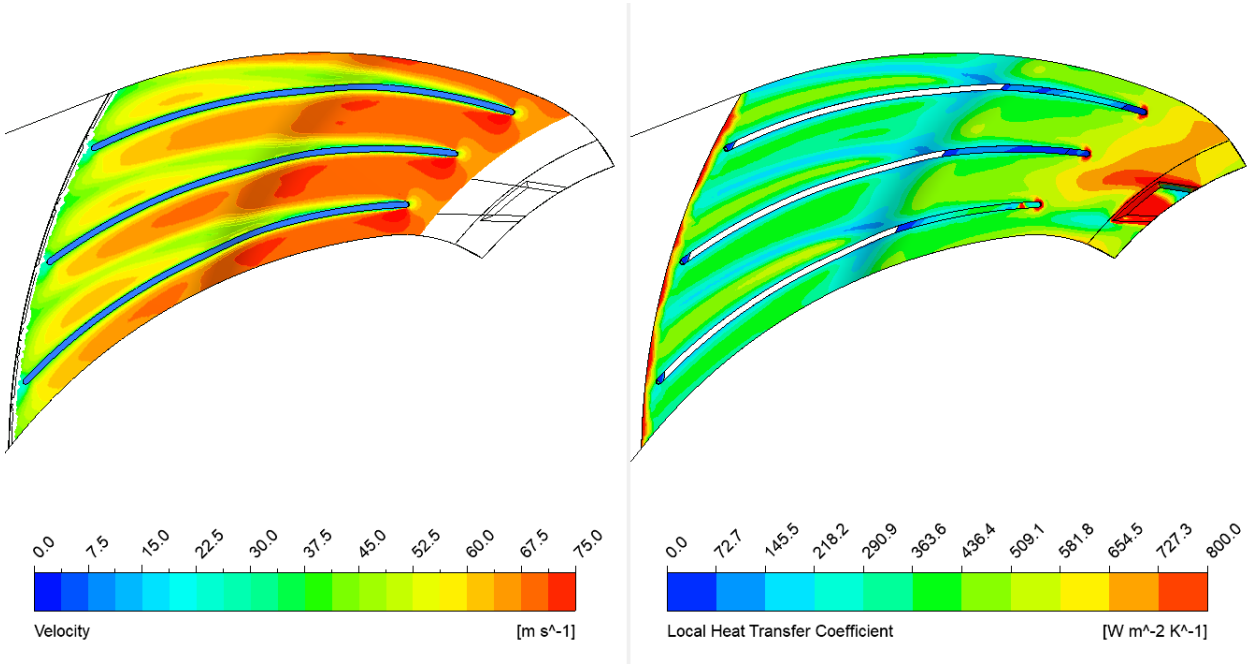

Fig. 4-35 Effect of flow separation shown through the velocity vectors (left) on local heat transfer on the rotor backside (right).

4.4 Rotor Enclosure Design

A final step for machine prototyping is the integration of the selected rotor design in a full motor assembly including the motor housing and the motor cover. The machine final assembly defines the initial shape, location, and dimensions of the rotor air cooling system inlet and outlets. The machine stackability requirement only allows for having all the air cooling system openings on its circumference which poses a challenge due to reduced airflow area and added pressure drop.

An initial enclosure (housing and cover) design considering the machine liquid cooling system hook up, mounting features, and overall mechanical-structural integrity is shown in Fig. 4-36. For each rotor side, a single inlet – single outlet casing design is initially proposed based on the design of a similar machine discussed in [60]. A conventional centrifugal fan design is proposed initially with a radial inlet that feeds the air to the impeller eye at the center, the air is then exhausted through a single outlet located at a nearly 90-degree angle from the inlet location to avoid short-circuiting of the hot air back into the inlet.

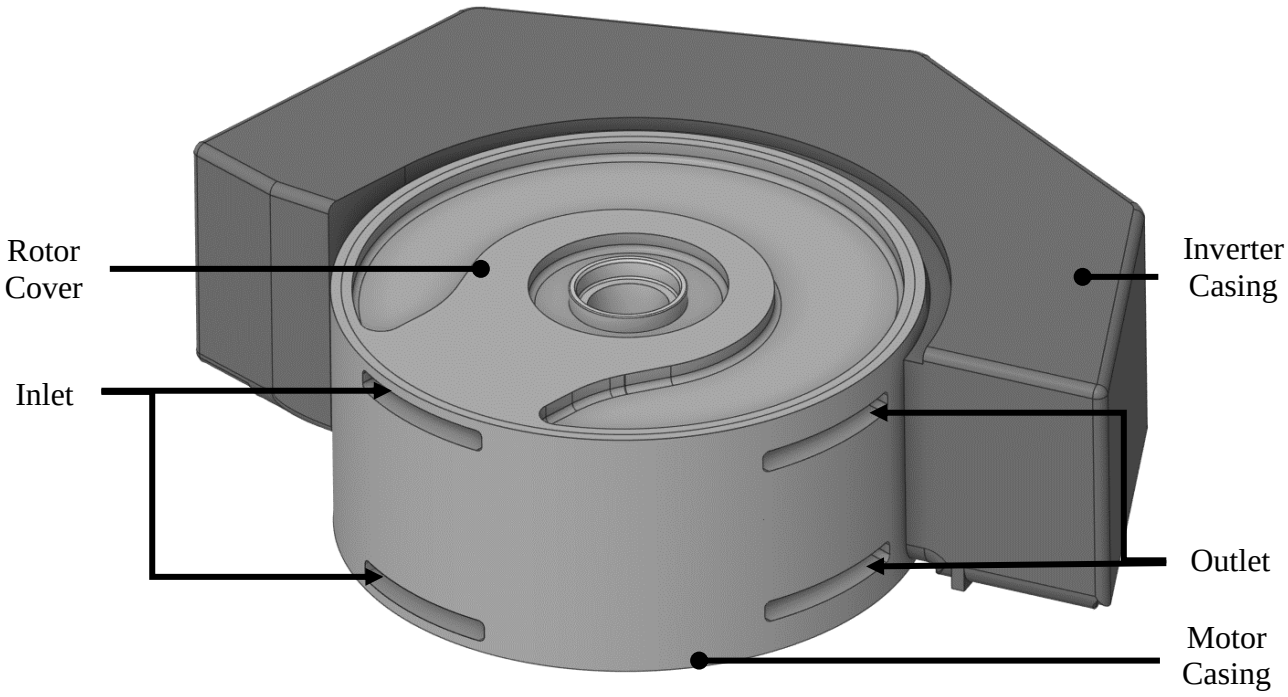

Fig. 4-36 Representation of the external view of the machine assembly with the initial enclosure design.

4.4.1 Casing / Outlet design

4.4.1.1 Spiral volute - single radial outlet

A simulation for the proposed design is run to reassess the thermal performance of the rotor given added flow restrictions to further fine-tune the enclosure design. Initial results (Fig. 4-37) showed a significant reduction in the rotor thermal performance compared to the previous simulations where no motor enclosure is considered. This is due to the reduced mass flow rate due to flow blockage, also the uneven flow distribution at the inlet as will be discussed in the following section.

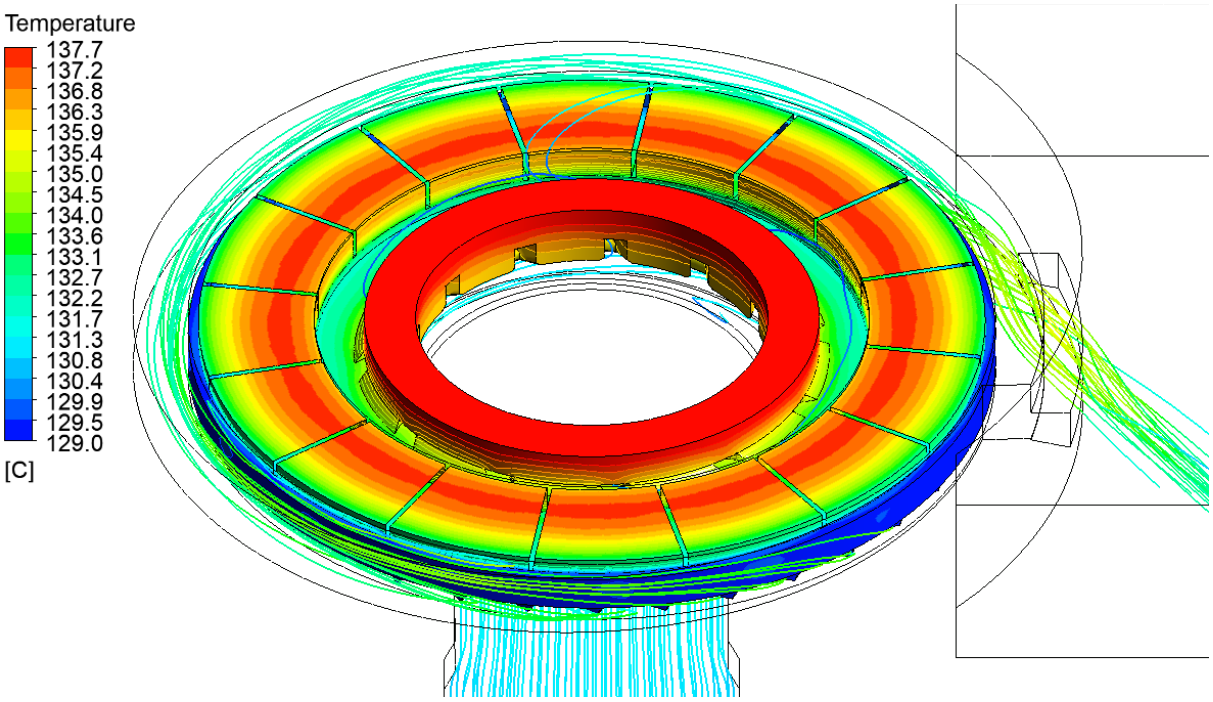

Fig. 4-37 Streamlines inside the rotor enclosure and the rotor temperature distribution with the initial enclosure design.

The sectional simulation for the same rotor presented in the previous section stands as a benchmark of the prototype rotor best thermal performance due to fewer flow restrictions and higher accuracy of the model. The simulation of the rotor considering the initial cover design shows a significant deterioration in the thermal performance. The magnets maximum temperature increased by 41.7 °C exceeding the design temperature limit by 37.7 °C.

Further analysis shows that the enclosure increased the pressure drop across the rotor hence reducing the mass flow rate given that there is no change in the rotational speed. Moreover, the excessive pressure development in the volute due to the dynamic pressure recovery and

having a single outlet resulted in uneven flow through the impeller or even flow blockage at certain. The radial outlet geometry reduced the effective outlet flow area which also contributed to the reduction in the mass flow rate and increased pressure drop.

The velocity contours indicate an unevenness in the instantaneous flow distribution through the rotor passages at a given timestep. The figures below (Fig. 4-38 and Fig. 4-39) show the correspondence of the zones of excessive pressure gradient near the outlet with the blade channels where the flow is weak or nearly blocked. The flow indicates the incompatibility of the volute design with the blades design and operating speed. The assembly geometry results in having the system operating below the optimum mass flow which results in small radial velocities at the outlet, while the tangential velocities are much higher than the through flow velocity in the volute. This results in deceleration of the flow at the outlet which leads to the excessive pressure rise at these locations and increased diffusion losses. An optimal volute design would normally result in pressure rise as it recovers the dynamic pressure. However, the increased pressure due to the suboptimal mass flow affects the uniformity and steadiness of the flow along the impeller circumference.

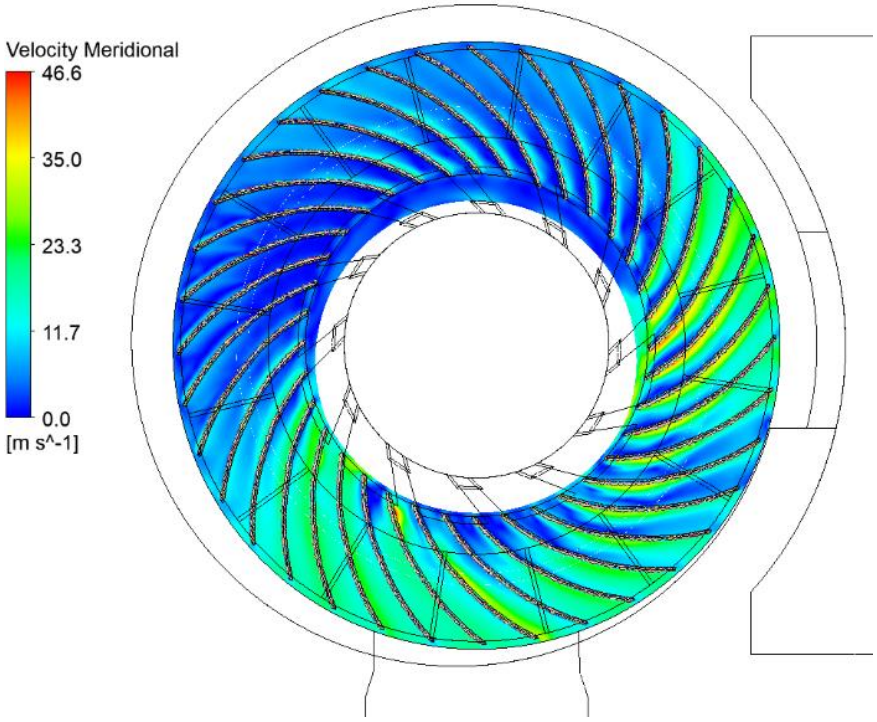

Fig. 4-38 Uneven circumferential flow distribution represented through uneven meridional velocities.

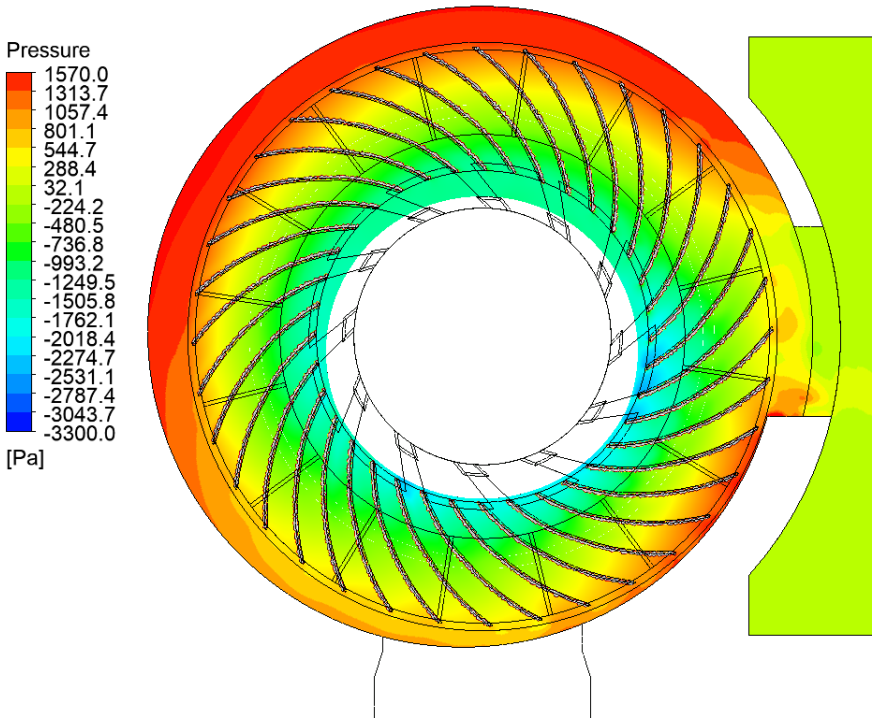

Fig. 4-39 Pressure rise across the rotor and the outlet volute showing excessive and uneven pressure rise.

4.4.1.2 Circular volute - two tangential outlets.

Changes are made to the volute design in order to avoid the unnecessary increase in temperature requires increasing its cross-sectional flow area. Such changes cannot be made to the casing design given the machine outer measurements limitations. Accordingly, spiral volute design with a single outlet is disregarded.

The new design shown in Fig. 4-40 has two oppositely located tangential outlets to allow for more even circumferential pressure distribution and to reduce the maximum flow pressure rise in the casing before it can be exhausted to the outside. The inlet design is kept the same to isolate its effect.

An alternative design that targets reducing the local excessive pressure increase hence improving the flow steadiness and uniformity. The design might not be precisely applicable since one of the proposed outlet locations would be interfering with the location designated for the inverter mounting as shown in Fig. 4-41. However, the design is still studied to check for potential improvement due to improving the pressure field around the impeller as well as increasing the outlet flow area.

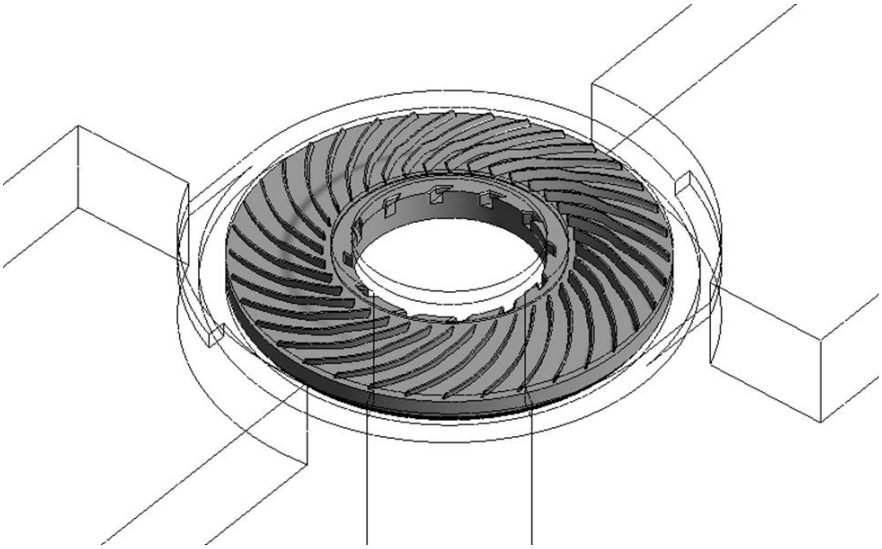

Fig. 4-40 Double outlet volute design (wireframe) with respect to the rotor.

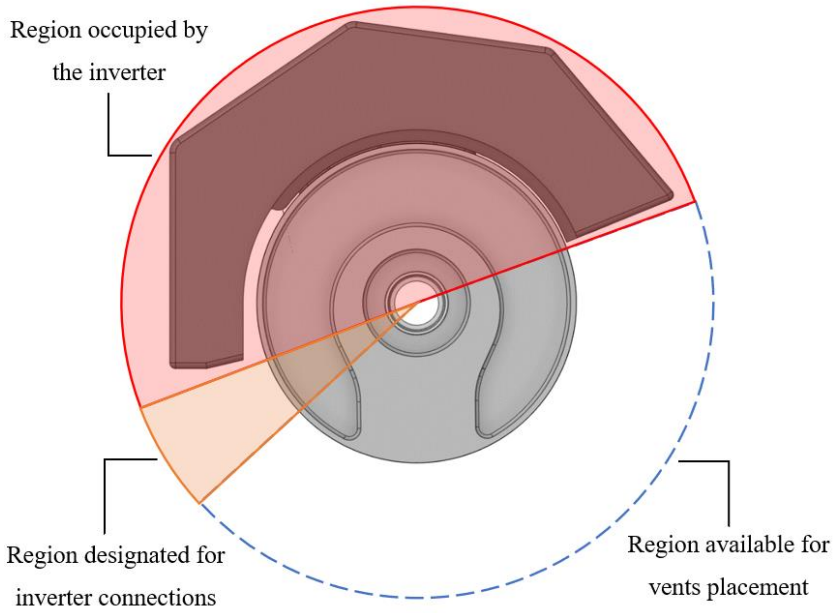

Fig. 4-41 Machine-inverter modular assembly and limitations on rotor enclosure geometry.

`The initial results showed that the maximum pressure in the volute dropped by 18% when compared to the previous design, while the mass flow with the new design increased by 36.5%. Heat transfer is improved thanks to the enhanced uniformity of the flow, the magnets maximum temperature dropped 14 degrees as a result. Flow blockage due to the fully radial outlet is mitigated through having tangential outlets as shown in Fig. 4-42.

The pressure contours shown in Fig. 4-43 show reduced average pressure around the fan impeller yielding a significant improvement in the overall flow through the impeller and increased pumping rate. The pressure increase due to flow deceleration in the first design is mitigated. However, the few regions exhibited a slight reduction at the blade outlet which that the flow is being accelerated to match the throughflow speed in the volute. The pressure reduction due to increased blade outlet velocity can also induce added losses similar to the first design. The high radial component and smaller tangential component at the impeller outlet result in a pressure gradient in the radial direction which also negatively affects the flow uniformity.

This study concludes that the reduced pressure development in the fan casing is beneficial for the fan pumping rate as well as flow uniformity, hence improving the heat transfer and rotor thermal performance. Further improvements can be yielded however through tweaking the blade angles as well as the inlet geometry. Reducing the blade outlet angle would improve the pressure distribution in the volute, especially in the radial direction which would further improve the flow uniformity by neutralizing the radial pressure gradient seen with the current design.

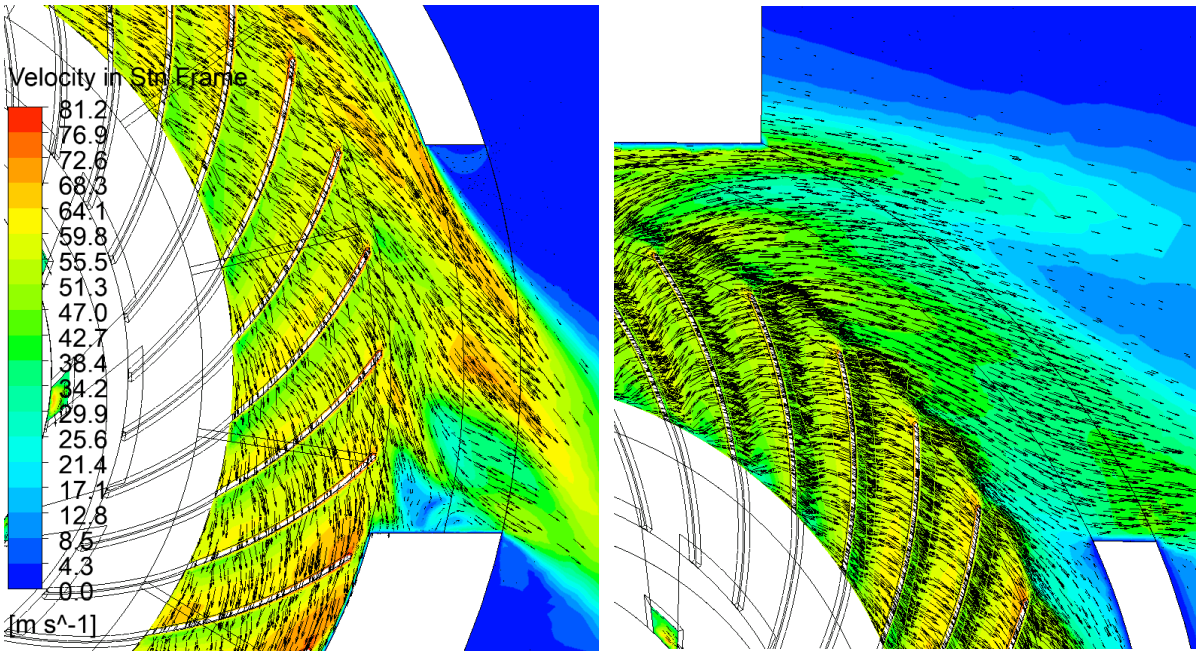

Fig. 4-42 Outlet volute flow velocity vectors showing the effect of tangential outlet in comparison to the fully radial outlet.

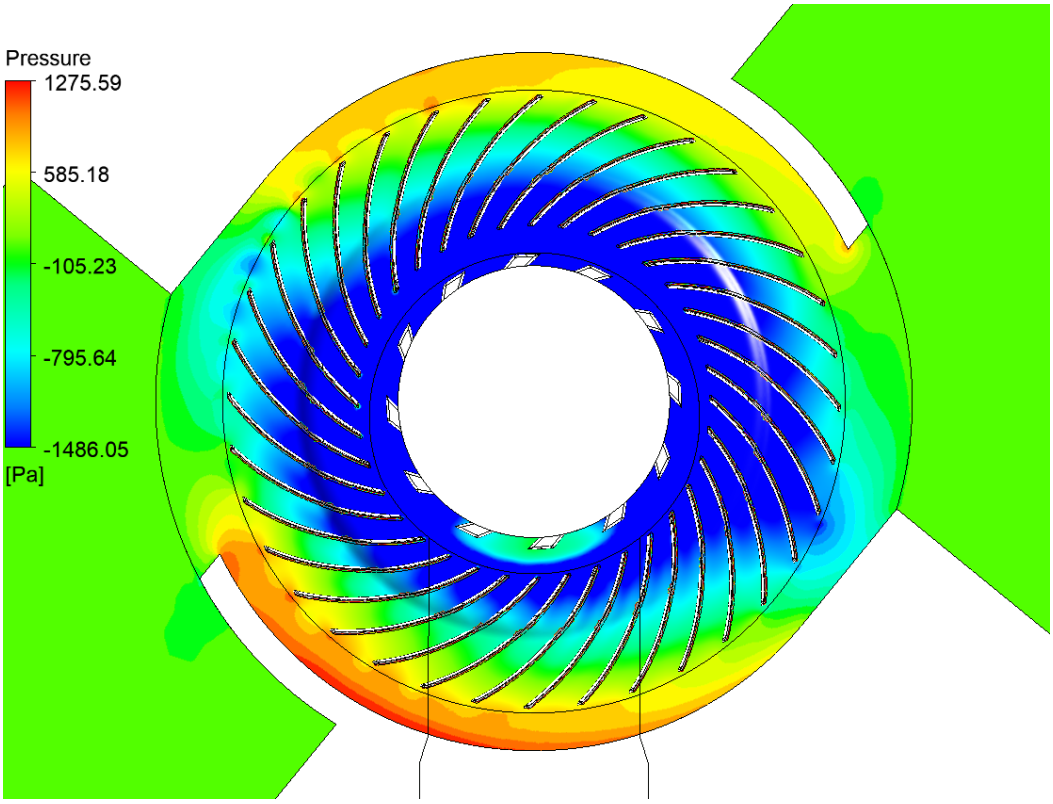

Fig. 4-43 Pressure development through the double outlet circular volute.

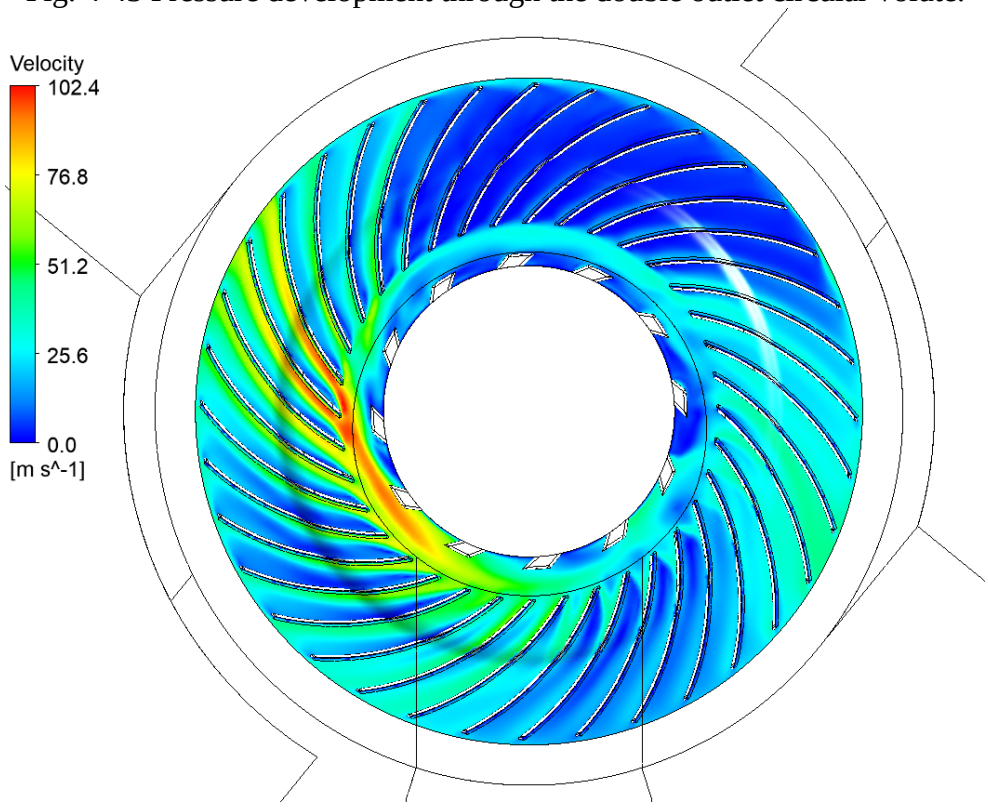

Fig. 4-44 Flow velocity distribution through the rotor with the circular volute.

4.4.1.2.1 Effect of outlet angle on double outlet volute throughflow

The previously discussed steps are taken to improve the volute design in order to reach the maximum pumping capability of the rotor as well as uniform flow distribution across the rotor channels. However, changes to the volute or casing geometry are limited by the motor assembly limitations. Accordingly, rotor-casing has to be designed as a single system. The radial pressure variation, as well as the pressure drop at the blade outlet shown in the pressure contours in Fig. 4-43, can be mitigated by modifying the blade angle. Reducing the blade angle at the outlet would flatten the outlet velocity triangle as shown in Fig. 4-45, which in turn would reduce the radial velocity component and increase the circumferential component to match the through flow velocity to mitigate the abrupt acceleration and the associated pressure drop. Reducing the radial velocity will also help avoid the radial pressure gradient in the volute. In addition to changing the rotor blades outlet angles, the inlet vent size opening is increased to counter the effect of reduced blade outlet angle on mass flow.

The result shows that the local pressure drop at the blades outlet is mitigated; however, the pressure gradient in the radial direction is still persistent. The pressure increases near the volute wall as the flow decelerates due to the wall friction. This explains the higher maximum pressure in the volute with the modified blade angle which is a result of deceleration of higher circumferential and through flow velocities.

.

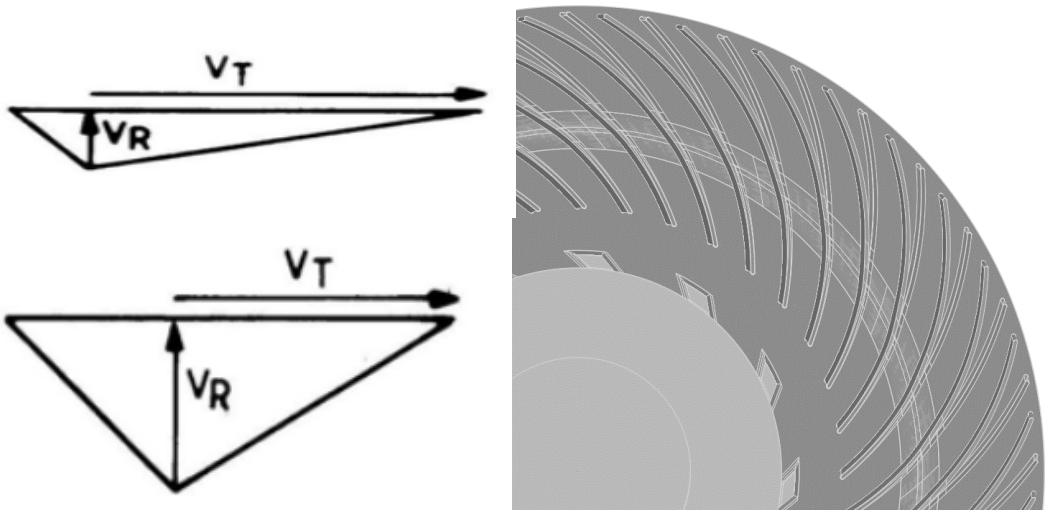

Fig. 4-45 Effect of blade outlet angle variation (right) on the flow velocity triangles, smaller blade outlet angle (top left), and larger blade outlet angle (bottom left).

Despite the higher outlet pressure, the mass flow rate increased by 21%, and the circumferential uniformity of the flow is improved. Moreover, overall heat transfer is improved resulting in 5 degrees lower magnets temperature. Another conclusion to be drawn from these results is that an excessive outlet angle would result in a higher radial component and smaller tangential component.

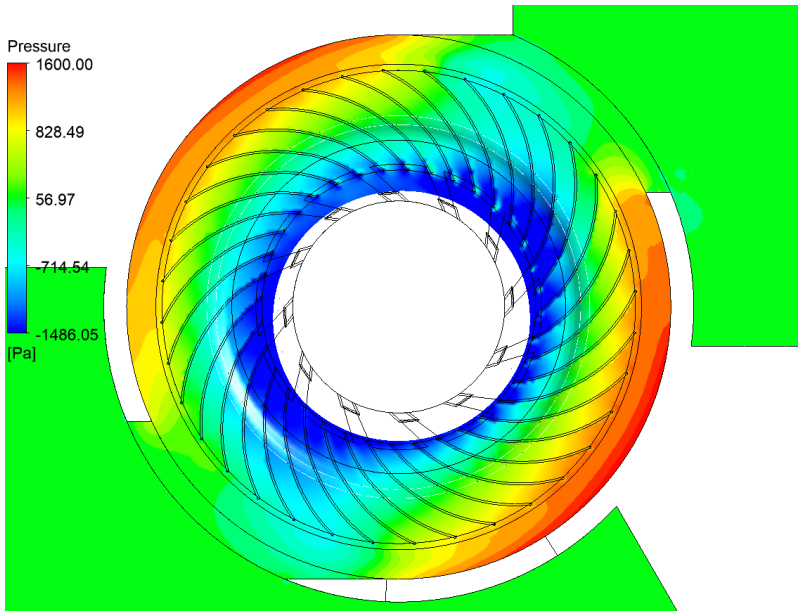

Fig. 4-46 Pressure development through the double outlet circular volute with reduced blade outlet angle.

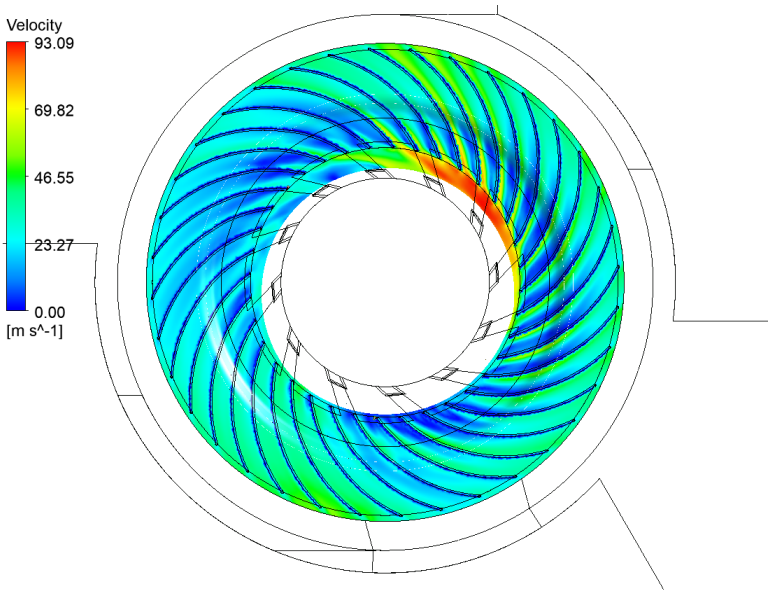

Fig. 4-47 Flow velocity distribution through the rotor with the circular volute with reduced blade outlet angle.

4.4.1.3 Circular volute – Multiple tangential outlets

The previous design showed that increasing the number and size of outlets improves the rotor thermal performance, however, it cannot be applied to targeted prototype design due to the motor assembly limitations discussed earlier. In the efforts to maximize the air mass flow rate and heat transfer and minimize the pressure drop across the rotor the following design shown in Fig. 4-48 are proposed where tangential outlet openings are placed wherever possible in the motor housing around the rotor.

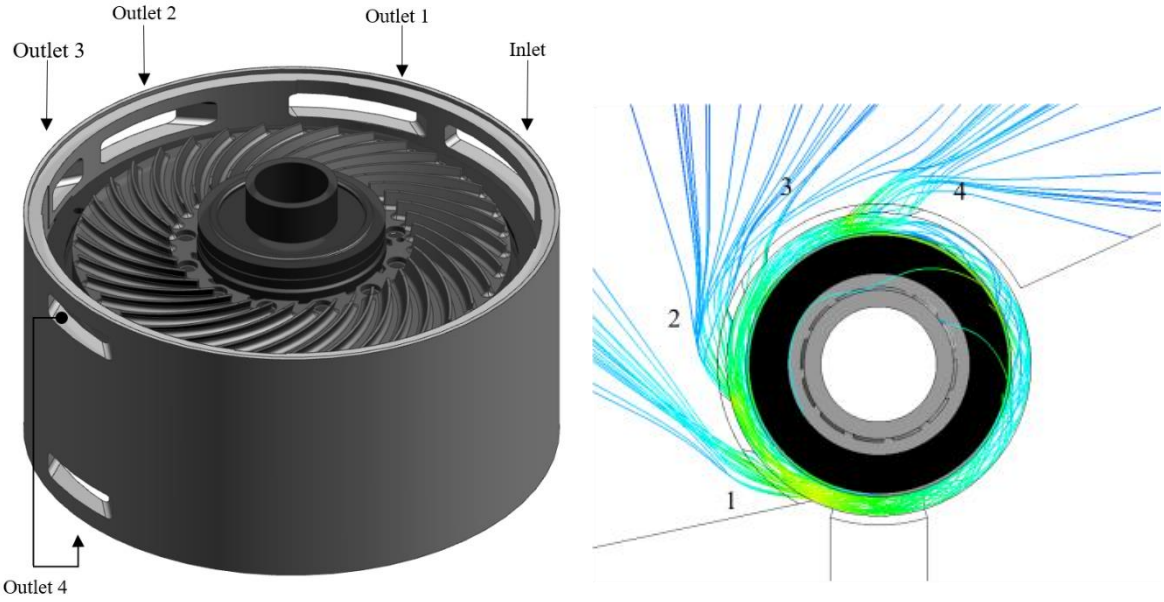

Fig. 4-48 Machine housing geometry with circular volute and multiple tangential outlets (left), and corresponding volute flow volumetric streamlines (right).

The blade outlet angle also appears to have an effect on the volute throughflow and the overall rotor thermal performance as shown in the previous section. Accordingly, the outlet blade angles have to be fine-tuned with respect to the newer volute design. The following design changes are targeting maximizing the mass flow rate and heat transfer while ensuring the best flow uniformity across the volute and the rotor.

The first tested rotor has an 18° outlet angle to account for potential reduction in the mass flow that might result from the uneven outlets distribution. The results showed a minimal reduction in the mass flow rate of 3% compared to the previous design with 28° outlet angles, this indicates higher fan efficiency given the higher pumping capacity with the smaller outlet angle. Despite the slightly lower mass flow rate, the heat transfer is improved over the magnets side of the rotor which reduced the temperature further by 8 degrees.

4.4.1.4 Rotor blades geometry fine-tuning

The casing outlets sizes and locations are fixed since they are maximized within the allowable space in the motor housing in the latest design. Moreover, the multiple outlet design is found to be better performing thermally than designs with smaller or fewer outlet openings.

On the other hand, the rotor geometry blade geometry is varied in order to further improve its thermal performance. On the first iteration of this process, the blade height is increased within the allowable dimensions of the machine. Increasing the blade height by 30 % (2mm) resulted in a 16% increase in mass flow rate and 5.6 degrees reduction in the magnets maximum temperature. The reduction in temperature is a result of the combined effect of increased mass flow rate and increased rotor surface area.

Three different blade outlet angles (18°, 28°, and 38°) are tested at the new blade height configuration as shown in Table 11. The three blade configurations showed comparable performance in terms of rotor pumping capacity and thermal performance. The intermediate blade angle, however, results in nearly the same magnets maximum and average temperature, however, the mass flow rate is slightly higher compared to the rotor with the smaller rotor outlet angle indicating better performance. The higher mass flow rate means that the windage losses are also higher as shown in the table.

The design decision is made to proceed with an intermediate blade angle. Although it is thermally comparable to the smaller blade angle, the smaller pressure rise and higher mass flow rate indicate a potential higher yield in performance through the enhancement of the inlet manifold design in the next step.

Outlet Blade Angle	**18°**	**28°**	**38°**
Max. Magnets Temperature [ºC]	109.5	109.7	111.2
Avg. Magnets Temperature [ºC]	106.6	106.8	108.4
Avg. Rotor Carrier Temperature [ºC]	102.6	102.6	105.5
Average Magnets Heat Transfer Coefficient, $\bar{h}_{\text{magnets}}$ [W/m^2.K]	38.5	37.3	41
Average Magnets Heat Transfer Coefficient, $\bar{h}_{\text{ carrier}}$ [W/m^2.K]	107.8	113.45	112.7
Q Magnets Percentage %	6.3	6	8.2
Q Rotor Carrier Percentage %	93.6	93.9	91.7

Ave. Relative Velocity on Carrier W[m/s]	30.5	29.6	29
Max. Relative Velocity on Carrier W[m/s]	91.9	102.3	110.7
Mass Flowrate [kg/s]	0.0516	0.0537	0.058
Windage Loss [W]	198.9	259.7	276.1
Pressure rise [Pa]	988	1108	1210

Table 11 Comparison of the results with different rotor blade outlet angles.

4.4.2 Inlet Cover / Manifold design

The machine stackable assembly dictates having the air be fed radially into the rotor fan section through a single opening in the machine outer casing. This is achieved through having a semi-circular manifold at the rotor fan impeller eye connected to a duct that passes under the rotor shroud leading to the designated inlet on the machine side as shown in Fig. 4-36

The initial inlet manifold design is based on the inlet configuration and design discussed by Fawzal et al. [60]. Although their study showed that the central inlet–tangential outlet design usually utilized with centrifugal fans performed the best among other discussed configurations, the negative effect of adapting this configuration in order to have a radial inlet instead of an axial inlet was not discussed.

Results from different simulations show that the radial side inlet results in significant losses and poor circumferential flow distribution at the impeller eye compared to the conventual axial inlet. The uneven distribution results in inconsistent flow velocities and angles at the blades inlet at a given instant during the motor operation at a steady state. The figure below (Fig. 4-49) shows the local heat transfer over the rotor surface in conjunction with the flow velocity vectors. The flow appears to be of a greater intensity on one side of the rotor where the blade leading edge has a velocity component in the direction opposite to the inlet manifold flow direction. The flow then impinges on the rotor surface and few blades resulting in a local high heat transfer coefficient near one side of the impeller eye compared to the other regions of the rotor. Moreover, the uneven flow results in an inconsistent angle of attack over the fan blades. The angle of attack over the blades is much larger on the side of higher flow intensities compared to the rest of the rotor. This results in having intense separation over these blades causing partial flow blockage in the passages between these blades hence deteriorated local heat transfer. The flow angle is found to be aligned with the blade inlet angle in some other regions maintaining a small angle of attack and minimal to no flow detachment which is directly reflected on the heat transfer downstream the blade passage inlet.

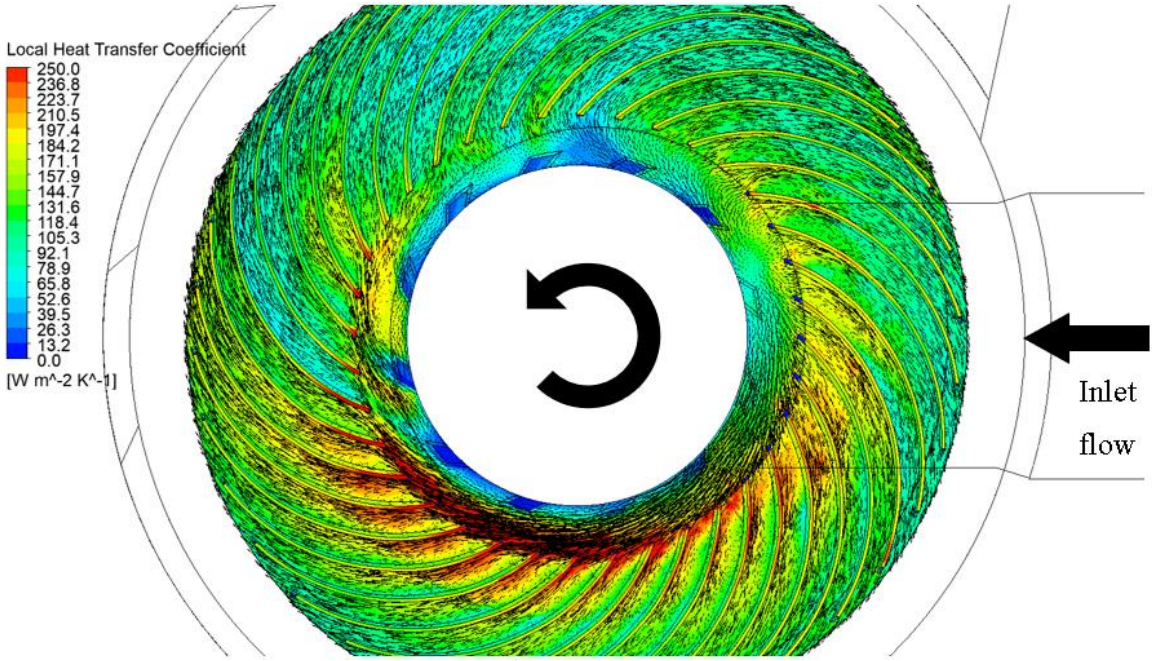

Fig. 4-49 Effect of the radial inlet on flow distribution and local heat transfer.

4.4.2.1 Assessment of axial inlet effect on rotor thermal performance

As discussed earlier, the one-sided radial inlet affected the flow distribution at the impeller eye which leads to a local reduction in the heat transfer in certain regions on the rotor surface. A separate study is carried out to assess the extent of deterioration that the radial inlet has on rotor thermal performance compared to the axial inlet. The axisymmetric flow from the axial inlet ensures having consistent flow angles at the inlet, hence a nearly even flow distribution and heat transfer throughout the rotor. Moreover, the inlet flow angle is maintained at its design angle for minimum shock loss and flow separation as shown in Fig. 4-50. The flow velocity vectors and heat transfer contours show the significantly improved flow and heat transfer distribution in the rotor with the axial inlet design. The shock-free entry achieved by the inlet design results in a larger effective flow area in between the blades which led to a significant increase in the mass flowrate, additionally, the reduced flow separation enhances the heat transfer over the blades and rotor surfaces. These two effects combined result in better thermal performance of the rotor hence, the magnets temperature is reduced by 6.9 degrees.

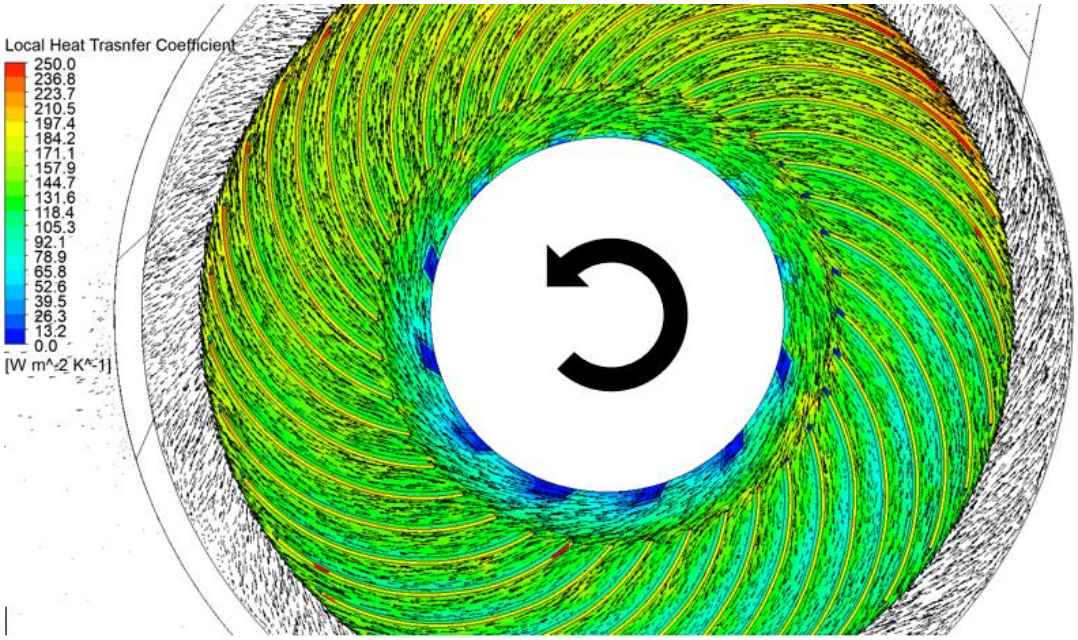

Fig. 4-50 Effect of axial inlet on flow distribution and local heat transfer.

Inlet Configuration	**Axial**	**Radial**
Max. Magnets Temperature [ºC]	102.6	109.5
Avg. Magnets Temperature [ºC]	99.6	106.6
Avg. Rotor Carrier Temperature [ºC]	95.8	102.6
Average Magnets Heat Transfer Coefficient, $\bar{h}_{\text{magnets}}$ [W/m^2.K]	42	38.5
Average Magnets Heat Transfer Coefficient, $\bar{h}_{\text{ carrier}}$ [W/m^2.K]	116	107.8
Ave. Relative Velocity on Carrier [m/s]	37	30.5
Max. Relative Velocity on Carrier [m/s]	92.3	91.9
Mass Flowrate [kg/s]	0.0817	0.0516
Windage Loss [W]	199	198.9
Max. Magnets Temperature [ºC]	872	988

Table 12 Comparison of cooling performance with radial and axial inlet manifolds.

4.4.2.2 Modified inlet manifold

The study showed the achievable enhancement through enhancement of the inlet flow field. The axial reduces the losses generated at the impeller eye due to:

1) flow sharp direction change
2) shock losses due to circumferential variations of the flow field at the inlet eye resulting in incorrect flow incident angle over the blades.
3) local decelerations in the inlet manifold cause separated flow at the impeller eye and the blades leading edges.

The effect of inlet manifold geometry on radial fan performance was discussed by Braembussche [78]. The author reviewed different geometries from previous studies that proposed solutions for the reduction of inlet-related losses. The radial inlet volute geometry proposed by Ludtke [79] was found to be the most suitable for our application due to its relative compactness and simplicity compared to tangential volutes for example. The center rib in the manifold is purposed for minimizing the flow angular momentum before the inlet eye for a near swirl-free inlet. The study, however, showed that the radial inlet manifold ducts can be greatly improved using the arrangement shown below. Although tangential inlet ducts offer better results in terms of flow uniformity, they tend to be less compact. The design is implemented with modifications to be accommodated within the limited space available for the cover. These modifications are expected to limit the intended design full capabilities of flow enhancement; However, the motor size limitations can not be compromised. The figures below (Fig. 4-51) show simplified sketches of the tested inlet geometry based on Ludtke design.

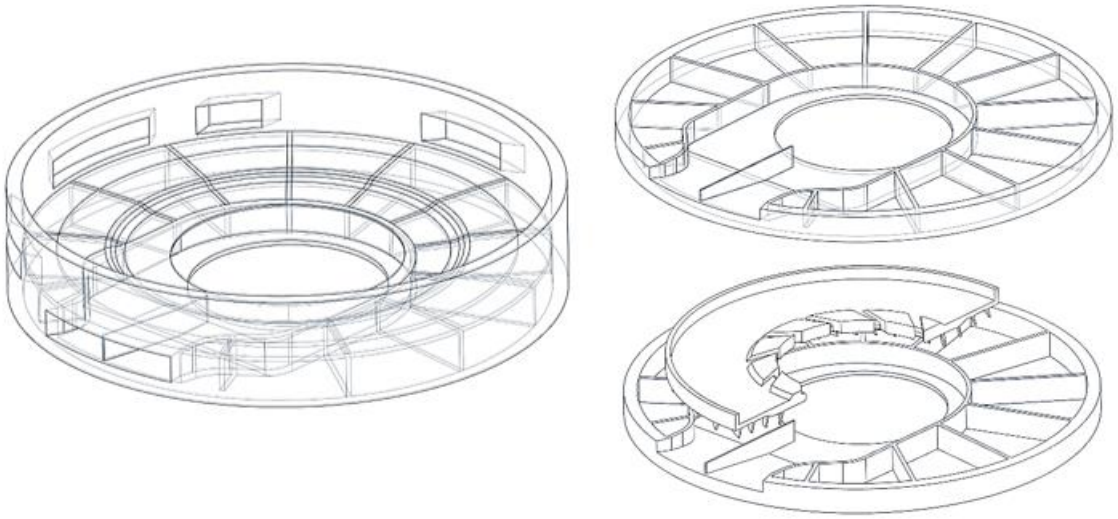

Fig. 4-51 Modified radial inlet design.

The results showed improvement in the flow uniformity at the impeller eye. The figures below (Fig. 4-52, Fig. 4-53, and Fig. 4-54) show the eye velocity distribution in each of the tested inlet ducts. Circumferential velocity variations are present in all the geometries; however, the axial inlet had the most distribution. Although the velocity magnitude is slightly varied, the flow angle shown by the velocity vectors is nearly consistent along the circumference. The observed variations are due to the downstream uneven flow caused by the outlet geometry, hence inevitable at this design stage.

The initial radial inlet design shows the highest flow unevenness with the increased number and size of separation regions. The modified radial inlet design, on the other hand, shows significant improvement in the flow evenness, a smaller difference between the maximum and minimum velocity magnitudes, and smaller separation regions. This improvement is reflected on the overall enhancement in the rotor thermal performance resulting in very comparable performance to that of the hypothetical optimum performance provided by the axial inlet. The table below compares different parameters of the thermal performance between the different designs. By comparing the different designs based on magnets temperature, the most important design parameter, the new inlet design is found to achieve the best performance and is chosen to proceed for prototyping stage.

Inlet Configuration	**Axial**	**Radial**	**Modified Radial**
Max. Magnets Temperature [ºC]	102.6	109.5	103.7
Avg. Magnets Temperature [ºC]	99.6	106.6	100.9
Avg. Rotor Carrier Temperature [ºC]	95.8	102.6	97.2
Average Magnets Heat Transfer Coefficient, $\bar{h}_{\text{magnets}}$ [W/m^2.K]	42	38.5	39.2
Average Magnets Heat Transfer Coefficient, $\bar{h}_{\text{ carrier}}$ [W/m^2.K]	116	107.8	131.6
Ave. Relative Velocity on Carrier [m/s]	37	30.5	34.8
Max. Relative Velocity on Carrier [m/s]	92.3	91.9	98
Mass Flowrate [kg/s]	0.0817	0.0516	0.0626
Windage Loss [W]	199	198.9	211.8

Table 13 Summary of cooling performance with radial and axial inlet manifolds.

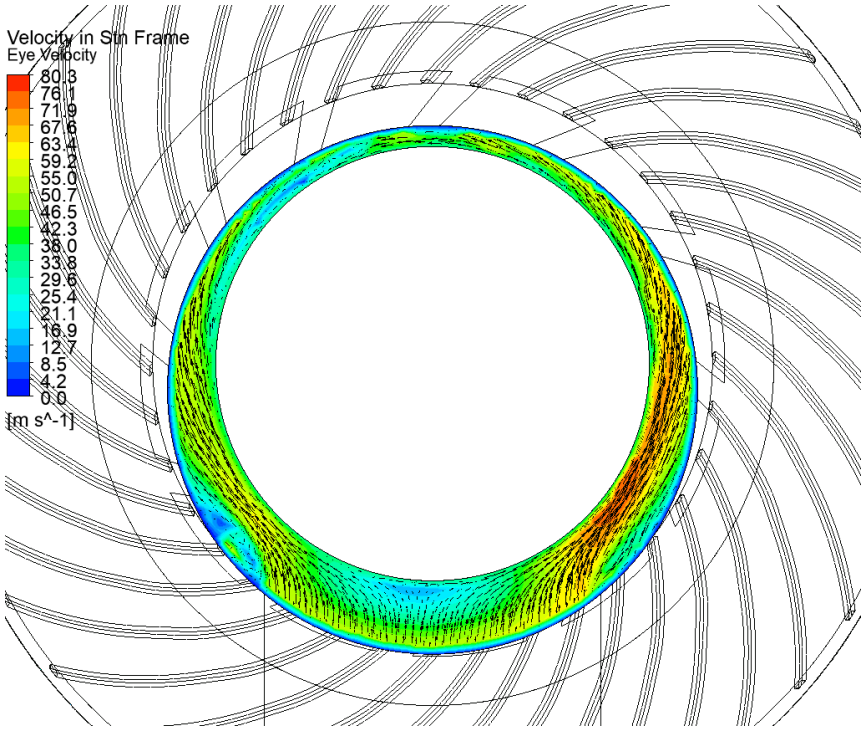

Fig. 4-52Flow velocity distribution at the inlet eye with the initial radial inlet manifold design.

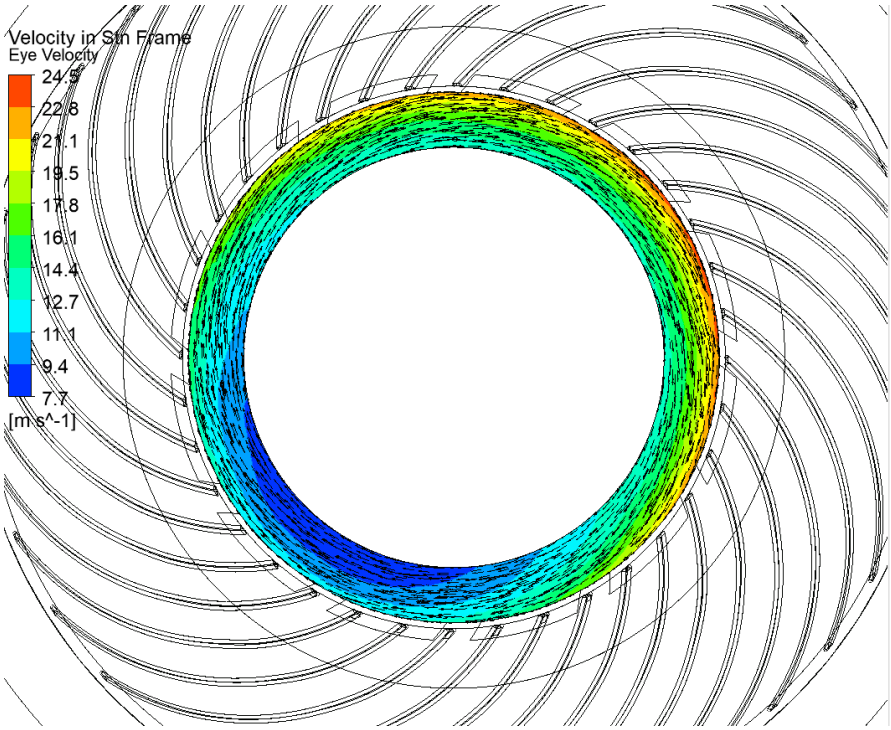

Fig. 4-53 Flow velocity distribution at the inlet eye with considering fully axial inlet design.

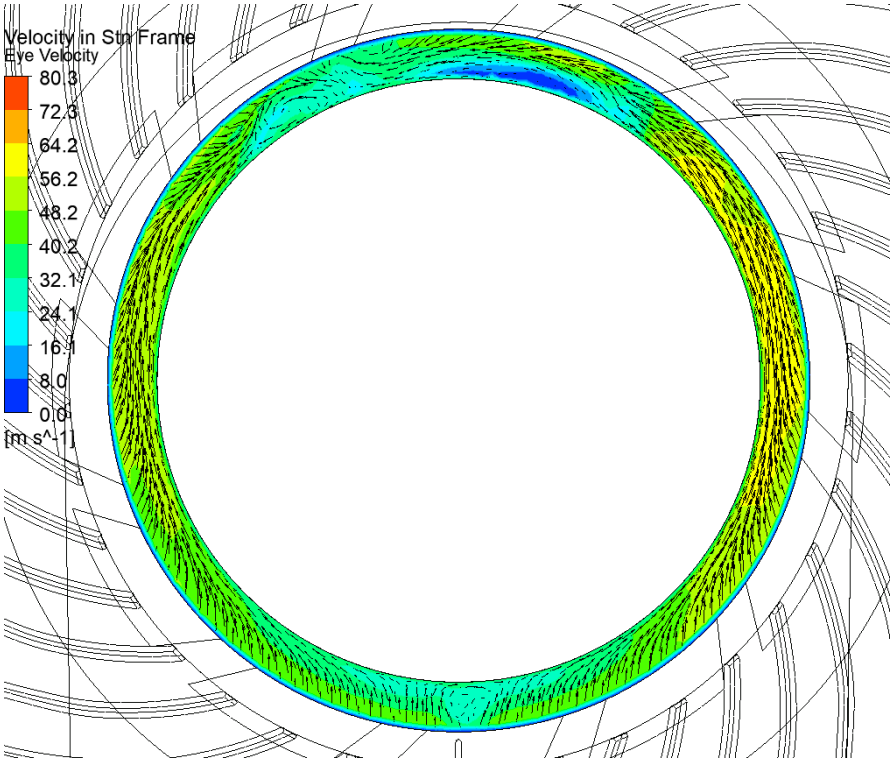

Fig. 4-54 Flow velocity distribution at the inlet eye with the modified radial inlet manifold design.

Chapter 5

Conclusion and Future Work

5 Conclusion and Future Work

5.1 Conclusion

The process of designing an integrated rotor air cooling system for a newly developed AFPM machine is discussed in this thesis. The requirement of the machine to be part of an aircraft propulsion system adds challenges to thermal design. Hence, particular attention has to be paid to the design of the rotor, where a failure due to permanent magnets demagnetizations or debonding as a result of excessive temperature rise would be critical to the aircraft safety.

Previous work by other researchers regarding different applications that involves cooling of rotating bodies is reviewed. Guidelines and possible geometrical features that can be utilized to increase the rotor heat transfer are concluded from the literature.

The concluded guidelines from literature can be summarized through the following points:

1. The air gap ratio should be kept lower than 0.02 to increase the heat transfer rate over the air gap surfaces by reducing the possibility of recirculation of hot air at the air gap.
2. Rotor air vents (holes) can greatly improve the heat transfer of the rotor inner surfaces.
3. Surface-mounted permanent magnets enhance the heat transfer by acting as a centrifugal fan, inducing a higher mass flow rate through flow ventilated machines.
4. The addition of surface features such as fan blades to the rotor surface improves the heat transfer on the rotor carrier by increasing its surface area and cooling air mass flow rate. However, the resulting cooling efficiency of the fan can greatly vary based on the blades geometry, hence, they have to be carefully designed to avoid an excessive increase in windage losses.
5. The air vents shape and location with respect to the rotor can significantly affect the cooling performance.

A study is performed based on these conclusions to determine the best combination of the rotor features that achieve the best cooling performance with special regards to the magnets temperature and windage losses as the two main design parameters. The rotor vents are found to be crucial for lowering the magnets temperature without significantly increasing the windage losses when compared to a non-vented rotor. The introduction of centrifugal fan effect through having a protruding surface on the rotor body is found to be essential for further

enhancement of the cooling rate and reducing the magnets temperature eventually. Conventional surface-mounted protruding magnets offer a great cooling performance by increasing the throughflow rotor ventilation and directly cooling the magnets. However, the electromagnetic design of the machine required having gapless Halbach magnets, hence, the using magnets protrusions as a cooling feature is disregarded. Rotor fan blades are found to result in higher windage power loss when compared to other features. Nevertheless, they significantly improve the rotor heat transfer and pumping capacity.

The study concluded that a vented rotor with embedded fan blades would be the most suitable configuration for the designed machine and further studies are done to improve the cooling performance of the blades are done.

Radial fan design concepts are utilized to improve the geometry of the blades. Design iterations are done using different rotor and blade geometries configurations. Sectional rotational CHT CFD simulations are used to assess the thermal performance of the tested geometries. Periodic sections of the full rotor assembly are modeled and simplified cover geometries with a fully axial inlet and open periphery are used for the simulations for blade shape studies for simplification.

Straight fan blades are tested for two different rotor carrier base geometries (back plated and open channeled rotors). The back plated rotor is modeled based on rotor geometries discussed in literature designed for a similar machine. The results showed that the rotor backplate is not effective for improving the heat transfer despite its larger surface area. On the other, the heat transfer and the pumping capacity in the open channeled rotor design are found to be significantly higher as a result of the increased flow area through the impeller. Despite both designs offering a sufficient cooling rate, they are found to generate excessive windage losses.

Backward curved blades are then tested, targeting lower windage losses. First, the blade inlet is fine-tuned for minimum separation through initial iterations. Second, the blade shape and outlet angle are improved through further simulations. This is done with the aid of analytical calculations to help determine the blade angle for the highest flow rate within the allowable windage losses range. The blade outlet angle of 38º is chosen accordingly and found to offer a sufficient cooling rate, resulting in safe operation magnets temperature at 60% less windage power loss compared to the rotor with the straight fan blades.

The last step for rotor design prior to prototyping is to design the cover(enclosure). An initial cover design with a radial inlet and a spiral volute was modeled. The initial enclosure geometry is based on literature and adapted to the designed machine dimensions and topology. Full rotor-enclosure assembly is modeled and simulated. The results showed significant deterioration in the overall heat transfer compared to the partially shrouded models initially studied due to uncontrolled pressure rise in the volute casing causing circumferential unevenness and major flow blockage near the impeller trailing edges. This resulted in a 41.7 ºC rise in the magnets maximum temperature pushing it far beyond the safe operating temperature limit.

Improvements are done to the outlet side first to isolate the effect of inlet flow. Multiple design iterations are done where the outlet volute shape, outlet locations and sizes, and blade outlet angles are varied to improve the pressure development across the impeller and flow evenness. Using a circular volute geometry, increasing the number and size of outlets, and fine-tuning the blade outlet angles eventually resulted in 28 degrees drop in the magnets temperature.

Further improvements are done through modification of the inlet manifold geometry. The fully axial inlet is studied first to insolate the effect of flow unevenness due to the radial inlet geometry and measure the highest possible enhancement through having wake-free flow at the impeller eye. The inlet manifold design is then modified to reduce the inlet flow angular momentum and abrupt flow direction change which contributes to the formation of wake regions at the impeller eye, unalignment of flow angles at the blades leading edges, and flow blockage eventually. This modified inlet results in further enhancement of the overall heat transfer and a comparable overall thermal performance to the axial inlet.

The final configuration of the inlet, rotor, and outlet is found sufficient to proceed to the prototyping stage. Although the maximum magnets temperature did not drop below the originally set temperature limit of 100 ºC, the design is found to be satisfactory for initial testing in a controlled lab environment where worst-case conditions is not expected. New rotor cooling methods and further improvements to the design are being researched for future prototypes.

5.2 Future work

Future research ideas for improvement of the AFPM rotor cooling and better usage of rotor cooling techniques are recognized through this research. These ideas are presented as follows:

1. Transient drive cycle thermal modeling

The rotor thermal performance is tested in the worst-case scenario at the highest power output of the motor. Despite the rotor being designed for safe operation at such operating conditions, the thermal performance through the full drive cycle of the aircraft might be useful for the assessment of thermal dependent electromagnetic and mechanical specifications of the motor. This will require a more thorough CFD thermal transient modeling of the rotor which might be very computationally expensive to perform. Minimizing the computational domain size and careful balancing of the model complexity and its errors is hence required to be studied.

2. Liquid cooling / Heat pipes in AFPM rotor cooling

An aluminum rotor carrier is used for the design in this research. Although the air cooling system design is able to maintain safe operating temperatures of the rotor, using a less conductive rotor carrier material than aluminum can pose a challenge to the thermal design. Other materials for the rotor carrier (such as steel and titanium) were tested the results showed a significant increase in the rotor temperatures by a margin of 10 to 15 ºC. While usage of heat pipes in AFPM stators was already researched in earlier studies such as the one presented by Scooby et al. [80], the utilization of miniature heat pipes or liquid cooling passages in the rotor cooling system can increase its efficiency by reducing the overall thermal resistivity of the rotor. Liquid cooling and heat pipes have been widely researched for radial machines rotors due to the easier implementation of the pipes in the central shaft near to the heat source at the center; However, the implementation in an AFPM rotor will be more challenging due to the flat rotor geometry. Accordingly, the thermal and mechanical rotor design must be carefully studied, and more research needs to be done.

3. Dual-purpose AFPM rotor impeller geometry

The feasibility of embedding fan blades directly to the rotor of an AFPM for cooling purposes inspires for direct application of AFPM machines rotor in turbomachines. The flat geometry of the AFPM machines rotors allows for having blades of different geometries embedded in

the rotor carrier as presented in this research. Turbomachines (fans, compressors, and pumps) often rely on external power drives which increases the size of their package assembly. Doubling the purpose of an AFPM machine rotor to directly act as an impeller for a turbomachinery application can result in significantly reducing their package size and improve their efficiency through the elimination of coupling mechanical losses. This concept can also be applied to the machine AFPM individually to eliminate the need for an external pump for its liquid cooling systems. Rotor impeller/casing design will need to be exclusively optimized for each of the mentioned applications and more complex mechanical considerations are expected for pump applications where liquids are involved.

References

[1] "Building a green economy: Government of Canada to require 100% of car and passenger truck sales be zero-emission by 2035 in Canada - Canada.ca." [Online]. Available: https://www.canada.ca/en/transport-canada/news/2021/06/building-a-green-economy-government-of-canada-to-require-100-of-car-and-passenger-truck-sales-be-zero-emission-by-2035-in-canada.html.

[2] "Government takes historic step towards net-zero with end of sale of new petrol and diesel cars by 2030 - GOV.UK." [Online]. Available: https://www.gov.uk/government/news/government-takes-historic-step-towards-net-zero-with-end-of-sale-of-new-petrol-and-diesel-cars-by-2030.

[3] B. Graver, K. Zhang, and D. Rutherford, "CO 2 emissions from commercial aviation, 2018," 2018.

[4] M. Klöwer, M. R. Allen, D. S. Lee, S. R. Proud, L. Gallagher, and A. Skowron, "Quantifying aviation's contribution to global warming," *Environ. Res. Lett*, vol. 16, p. 104027, 2021.

[5] "Climate change: Should you fly, drive or take the train? - BBC News." [Online]. Available: https://www.bbc.com/news/science-environment-49349566.

[6] L. Dorn-Gomba, J. Ramoul, J. Reimers, and A. Emadi, "Power Electronic Converters in Electric Aircraft: Current Status, Challenges, and Emerging Technologies," *IEEE Trans. Transp. Electrif.*, vol. 6, no. 4, pp. 1648–1664, Dec. 2020.

[7] D. P. Thipphavong *et al.*, "Urban air mobility airspace integration concepts and considerations," *2018 Aviat. Technol. Integr. Oper. Conf.*, 2018.

[8] "Vahana | Airbus." [Online]. Available: https://www.airbus.com/en/innovation/zero-emission/urban-air-mobility/vahana.

[9] "Joby Begins Journey to Becoming First eVTOL Airline | Joby." [Online]. Available: https://www.jobyaviation.com/news/joby-begins-journey-become-first-evtol-airline/.

[10] S. C. Oh and A. Emadi, "Test and simulation of axial flux-motor characteristics for hybrid electric vehicles," *IEEE Trans. Veh. Technol.*, vol. 53, no. 3, pp. 912–919, May 2004.

[11] R. Camilleri, T. Woolmer, A. Court, and M. D. McCulloch, “Investigation into the temperature profile of a liquid cooled YASA© AFPM machine,” *IET Conf. Publ.*, vol. 2012, no. 592 CP, 2012.

[12] B. Bilgin *et al.*, “Modeling and Analysis of Electric Motors: State-of-the-Art Review,” *IEEE Trans. Transp. Electrif.*, vol. 5, no. 3, pp. 602–617, 2019.

[13] W. Sixel, M. Liu, and B. Sarlioglu, “Rotor Thermal Design for Electric Machines: Challenges and Opportunities,” in *2018 IEEE Transportation Electrification Conference and Expo (ITEC)*, 2018, pp. 821–826.

[14] T. Sebastian, “Temperature Effects on Torque Production and Efficiency of PM Motors Using NdFeB Magnets,” *IEEE Trans. Ind. Appl.*, vol. 31, no. 2, pp. 353–357, 1995.

[15] T. V. Kármán, “Über laminare und turbulente Reibung,” *ZAMM - J. Appl. Math. Mech. / Zeitschrift für Angew. Math. und Mech.*, vol. 1, no. 4, pp. 233–252, Jan. 1921.

[16] U. T. Bödewadt, “Die Drehströmung über festem Grunde,” *ZAMM - J. Appl. Math. Mech. / Zeitschrift für Angew. Math. und Mech.*, vol. 20, no. 5, pp. 241–253, Jan. 1940.

[17] G. K. Batchelor, “ Note on A Class of Solutions of The Navier-Stokes Equations Representing Steady Rotationally-Symmetric Flow,” *Q. J. Mech. Appl. Math.*, vol. 4, no. 1, pp. 29–41, Jan. 1951.

[18] K. Stewartson, “On the flow between two rotating coaxial disks,” *Math. Proc. Cambridge Philos. Soc.*, vol. 49, no. 2, pp. 333–341, 1953.

[19] G. N. Lance; and M. H. Rogers, “The axially symmetric flow of a viscous fluid between two infinite rotating disks,” *Proc. R. Soc. London. Ser. A. Math. Phys. Sci.*, vol. 266, no. 1324, pp. 109–121, Feb. 1962.

[20] C. E. Pearson, “Numerical solutions for the time-dependent viscous flow between two rotating coaxial disks,” *J. Fluid Mech.*, vol. 21, no. 4, pp. 623–633, 1965.

[21] L. Durlofsky, “Topics in fluid mechanics: I. flow between finite rotating disks II. simulation of hydrodynamically interacting particles in stokes flow.,” 1986.

[22] H. P. Greenspan, D. R. Rodenhuis, and W. M. Elsasser, “The Theory of Rotating Fluids: Cambridge Monograph on Mechanics and Applied Mathematics,” *Phys. Today*, vol. 22, no. 7, pp. 81–82, Jan. 1969.

[23] S. V. Parter, “On the swirling flow between rotating coaxial disks: a survey,” pp. 258–280, 1982.

[24] P. J. Zandbergen and D. Dijkstra, “Von Karman Swirling Flows.,” *Annu. Rev. Fluid Mech.*, vol. 19, no. 1, pp. 465–491, Nov. 1987.

[25] G. L. Mellor, P. J. Chapple, and V. K. Stokes, “On the flow between a rotating and a stationary disk,” *J. Fluid Mech.*, vol. 31, no. 1, pp. 95–112, Jan. 1968.

[26] J. F. Brady and L. ; Durlofsky, “On rotating disk flow,” Cambridge University Press, 1987.

[27] J. W. Daily and R. E. Nece, “Chamber dimension effects on induced flow and frictional resistance of enclosed rotating disks,” *J. Fluids Eng. Trans. ASME*, vol. 82, no. 1, pp. 217–230, Mar. 1960.

[28] J. M. Owen and R. H. Rogers, “Flow and heat transfer in rotating-disc systems.” New York, NY (USA); John Wiley and Sons Inc., 01-Jan-1989.

[29] S. Poncet, R. Schiestel, and M. P. Chauve, “Centrifugal flow in a rotor-stator cavity,” in *Journal of Fluids Engineering, Transactions of the ASME*, 2005, vol. 127, no. 4, pp. 787–794.

[30] S. Poncet, M. P. Chauve, and R. Schiestel, “Batchelor versus Stewartson flow structures in a rotor-stator cavity with throughflow,” *Phys. Fluids*, vol. 17, no. 7, pp. 1–15, 2005.

[31] E. C. Cobb and O. Saunders, “Heat transfer from a rotating disc,” *Am. Soc. Mech. Eng.*, Aug. 1990.

[32] L. Dorfman, *Hydrodynamic resistance and the heat loss of rotating solids*, [1st English ed.]. Edinburgh: Oliver & Boyd, 1963.

[33] SOO and SL, “Laminar flow over an enclosed rotating disk,” *Trans ASME*, vol. 80, pp. 287–296, 1958.

[34] V. M. Kapinos, “Heat transfer from a disc rotating in a housing with a radial flow of coolant,” *J. Eng. Phys. 1965 81*, vol. 8, no. 1, pp. 35–38, Jan. 1965.

[35] J. M. Owen, “The effect of forced flow on heat transfer from a disc rotating near a stator,” *Int. J. Heat Mass Transf.*, vol. 14, no. 8, pp. 1135–1147, Aug. 1971.

[36] F. Kreith, E. Doughman, and H. Kozlowski, “Mass and Heat Transfer From an Enclosed Rotating Disk With and Without Source Flow,” *J. Heat Transfer*, vol. 85, no. 2, pp. 153–162, May 1963.

[37] J. M. Owen, “The Reynolds analogy applied to flow between a rotating and a stationary disc,” *Int. J. Heat Mass Transf.*, vol. 14, no. 3, pp. 451–460, Mar. 1971.

[38] R. Boutarfa and S. Harmand, “Local convective heat transfer for laminar and turbulent flow in a rotor-stator system,” *Exp. Fluids*, vol. 38, no. 2, pp. 209–221, Feb. 2005.

[39] S. Baina, “Écoulement entre deux disques : instabilités et transition laminaire turbulent,” Nov. 1994.

[40] J. Lin, T. Lambert, Y. Yang, B. Bilgin, R. Lankin, and A. Emadi, “A novel axial flux switched reluctance motor with multi-level air gap geometry,” *2016 IEEE Electr. Power Energy Conf. EPEC 2016*, Dec. 2016.

[41] A. Rasekh, P. Sergeant, and J. Vierendeels, “Fully predictive heat transfer coefficient modeling of an axial flux permanent magnet synchronous machine with geometrical parameters of the magnets,” *Appl. Therm. Eng.*, vol. 110, pp. 1343–1357, Jan. 2017.

[42] D. A. Howey, A. S. Holmes, and K. R. Pullen, “Measurement and CFD Prediction of Heat Transfer in Air-Cooled Disc-Type Electrical Machines,” *IEEE Trans. Ind. Appl.*, vol. 47, no. 4, pp. 1716–1723, Jul. 2011.

[43] G. Airoldi *et al.*, “Air flow and heat transfer modeling of an axial flux permanent magnet generator,” *World Acad. Sci. Eng. Technol.*, vol. 58, pp. 809–813, 2009.

[44] A. S. Fawzal, “Numerical Modelling and Analysis of a New Rotor Cooling Technique for Axial Flux Permanent Magnet Machines.”

[45] C. H. Lim *et al.*, “2-D lumped-parameter thermal modelling of axial flux permanent magnet generators,” in *Proceedings of the 2008 International Conference on Electrical Machines, ICEM’08*, 2008.

[46] R. Camilleri, D. A. Howey, and M. D. McCulloch, “Thermal limitations in air-cooled axial flux in-wheel motors for urban mobility vehicles: A preliminary analysis,” in *Electrical Systems for Aircraft, Railway and Ship Propulsion, ESARS*, 2012.

[47] N. Rostami, M. R. Feyzi, J. Pyrhonen, A. Parviainen, and M. Niemela, “Lumped-parameter thermal model for axial flux permanent magnet machines,” *IEEE Trans. Magn.*, vol. 49, no. 3, pp. 1178–1184, 2013.

[48] C. Corey and W. Wink, “3D Thermal Network Modeling for Axial-Flux Permanent Magnet Machines with Experimental Validation,” pp. 4059–4066, Nov. 2021.

[49] D. A. Howey, “Thermal design of air-cooled axial flux permanent magnet machines,” 2010.

[50] C. Wang, R. Qu, J. Li, X. Fan, D. Li, and Y. Lu, “Rotor loss calculation and thermal analysis of a dual-stator axial-flux permanent magnet machine with combined rectangle-shaped magnets,” in *2017 20th International Conference on Electrical Machines and Systems, ICEMS 2017*, 2017.

[51] J. Parviainen, A., Niemelä, M., & Pyrhönen, “Modeling axial-flux PM machines: Thermal analysis,” in *In Proceedings of International Conference on Electrical Machines ICEM’04*, 2004.

[52] K. M. Becker and J. Kaye, “Measurements of Diabatic Flow in an Annulus With an Inner Rotating Cylinder,” *J. Heat Transfer*, vol. 84, no. 2, pp. 97–104, May 1962.

[53] G. Airoldi *et al.*, “Computations on heat transfer in axial flux permanent magnet machines,” in *Proceedings of the 2008 International Conference on Electrical Machines, ICEM’08*, 2008, pp. 1–6.

[54] D. A. Howey, A. S. Holmes, and K. R. Pullen, “Measurement of stator heat transfer in air-cooled axial flux permanent magnet machines,” in *2009 35th Annual Conference of IEEE Industrial Electronics*, 2009, pp. 1197–1202.

[55] D. A. Howey, A. S. Holmes, and K. R. Pullen, “Radially resolved measurement of stator heat transfer in a rotor-stator disc system,” *Int. J. Heat Mass Transf.*, vol. 53, no. 1–3, pp. 491–501, Jan. 2010.

[56] A. Rasekh, P. Sergeant, and J. Vierendeels, “A parametric-CFD study for heat transfer and fluid flow in a rotor-stator system,” 2014.

[57] A. Rasekh, P. Sergeant, and J. Vierendeels, “Convective heat transfer prediction in disk-type electrical machines,” *Appl. Therm. Eng.*, vol. 91, pp. 778–790, Dec. 2015.

[58] A. S. Fawzal, R. M. Cirstea, K. N. Gyftakis, T. J. Woolmer, M. Dickison, and M. Blundell, “Fan Performance Analysis for Rotor Cooling of Axial Flux Permanent Magnet Machines,” *IEEE Trans. Ind. Appl.*, vol. 53, no. 4, pp. 3295–3304, Jul. 2017.

[59] A. S. Fawzal, R. M. Cirstea, K. N. Gyftakis, T. J. Woolmer, M. Dickison, and M. Blundell, “The fan design impact on the rotor cooling of axial flux permanent magnet machines,” in *2016 XXII International Conference on Electrical Machines (ICEM)*, 2016, pp. 2725–2731.

[60] A. S. Fawzal, R. M. Cirstea, T. J. Woolmer, M. Dickison, M. Blundell, and K. N. Gyftakis, “Air inlet/outlet arrangement for rotor cooling application of axial flux PM machines,” 2017.

[61] J. Hey, D. Howey, R. Martinez-Botas, and M. Lamperth, “Transient Thermal Modeling of an Axial Flux Permanent Magnet (AFPM) Machine Using a Hybrid Thermal Model,” World Academy of Science, Engineering and Technology (WASET), Dec. 2010.

[62] J. Hey, D. A. Howey, R. Martinez-Botas, and M. Lamperth, “Transient thermal modelling of an Axial Flux Permanent Magnet (AFPM) machine with model parameter optimisation using a Monte Carlo method.”

[63] Y. C. Chong, E. J. P. Echenique Subiabre, M. A. Mueller, J. Chick, D. A. Staton, and A. S. McDonald, “The ventilation effect on stator convective heat transfer of an axial-flux permanent-magnet machine,” *IEEE Trans. Ind. Electron.*, vol. 61, no. 8, pp. 4392–4403, Aug. 2014.

[64] H. Vansompel, “Design of an energy efficient axial flux permanent magnet machine,” *undefined*, 2013.

[65] D. Parish and D. G. Macmanus, “Aerodynamic investigations of ventilated brake disks,” 2005.

[66] “ANSYS FLUENT 12.0 User’s Guide.” [Online]. Available:https://www.afs.enea.it/project/neptunius/docs/fluent/html/ug/main_pre.htm. [Accessed: 28-Dec-2021].

[67] “ANSYS CFX-Solver Theory Guide,” vol. 15317, no. April, pp. 724–746, 2009.

[68] F. R. Menter, “Zonal two equation κ-ω turbulence models for aerodynamic flows,” *AIAA 23rd Fluid Dyn. Plasmadynamics, Lasers Conf. 1993*, 1993.

[69] P. R. Spalart and M. Shur, “On the sensitization of turbulence models to rotation and curvature,” *Aerosp. Sci. Technol.*, vol. 1, no. 5, pp. 297–302, Jul. 1997.

[70] A. Malloy, “Thermal Management of the Permanent Magnets in a Totally Enclosed Axial Flux Permanent Magnet Synchronous Machine,” 2014.

[71] G. Airoldi, “Durham E-Theses Numerical Investigations of Air Flow and Heat Transfer in Axial Flux Permanent Magnet Electrical Machines.”

[72] A. S. Fawzal, R. M. Cirstea, K. N. Gyftakis, T. J. Woolmer, M. Dickison, and M. Blundell, “Fan Performance Analysis for Rotor Cooling of Axial Flux Permanent Magnet Machines,” *IEEE Trans. Ind. Appl.*, vol. 53, no. 4, pp. 3295–3304, 2017.

[73] H. Yan, W.-T. Wu, S. Feng, and G. Xie, “Role of vane configuration on the heat dissipation performance of ventilated brake discs,” *Appl. Therm. Eng.*, vol. 136, pp. 118–130, May 2018.

[74] P. Epple, B. Karic, Č. Ilić, S. Becker, F. Durst, and A. Delgado, “Design of radial impellers: A combined extended analytical and numerical method,” *Proc. Inst. Mech. Eng. Part C J. Mech. Eng. Sci.*, vol. 223, no. 4, pp. 901–917, Apr. 2009.

[75] Y. Madhu, M. Reddy, and U. Sri, “HEAT TRANSFER ANALYSIS OF AUTOMOTIVE DISC BRAKES,” 2014.

[76] K. Pantell, “Über die Schaufelausbildung von Turbo,” *Arbeitsmaschinen. Konstr.*, vol. 3, pp. 77–82, 1949.

[77] B. Eckert and E. Schnell, *Axial- und Radialkompressoren*. Springer-Verlag Berlin Heidelberg, 1961.

[78] R. A. Van den Braembussche, “Flow and loss mechanisms in volutes of centrifugal pumps,” *Rto-En-Avt*, vol. 143, no. July, pp. 1–26, 2006.

[79] K. Ludtke, “Centrifugal process compressors - radial vs. tangential suction nozzles.,” Mar. 1985.

[80] S. T. Scowby, R. T. Dobson, and M. J. Kamper, “Thermal modelling of an axial flux permanent magnet machine,” *Appl. Therm. Eng.*, vol. 24, no. 2–3, pp. 193–207, Feb. 2004.